



**TECHNISCHE  
UNIVERSITÄT  
DRESDEN**



# **Spin-transfer torques in MgO-based magnetic tunnel junctions**

## **DISSERTATION**

**zur Erlangung des akademischen Grades**

**Doktoringenieur**

**(Dr.-Ing.)**

**vorgelegt**

**der Fakultät Maschinenwesen**

**der Technischen Universität Dresden**

**von**

**Dipl.-Ing. Kerstin Bernert**

**geboren am 24.01.1985 in Karl-Marx-Stadt jetzt Chemnitz**

**eingereicht im November 2013**

Die Dissertation wurde in der Zeit von November 2008 bis November 2013 am Institut für Ionenstrahlphysik und Materialforschung des Helmholtz-Zentrums Dresden-Rossendorf e.V. angefertigt.



# Eigenständigkeitserklärung

Hiermit versichere ich, dass ich die vorliegende Arbeit ohne unzulässige Hilfe Dritter und ohne Benutzung anderer als der angegebenen Hilfsmittel angefertigt habe; die aus fremden Quellen direkt oder indirekt übernommenen Gedanken sind als solche kenntlich gemacht.

Bei der Auswahl und Auswertung des Materials sowie bei der Herstellung des Manuskripts habe ich Unterstützungsleistungen von folgenden Personen erhalten: Prof. Dr. Jürgen Faßbender, Prof. Dr. Gianarelio Cuniberti, Dr. Alina Deac, Dr. Ciarán Fowley, Dr. Volker Sluka, Dr. Christopher Bunce. Weitere Personen waren an der geistigen Herstellung der vorliegenden Arbeit nicht beteiligt. Insbesondere habe ich nicht die Hilfe eines kommerziellen Promotionsberaters in Anspruch genommen. Dritte haben von mir keine geldwerten Leistungen für Arbeiten erhalten, die in Zusammenhang mit dem Inhalt der vorgelegten Dissertation stehen.

Die Arbeit wurde bisher weder im Inland noch im Ausland in gleicher oder ähnlicher Form einer anderen Prüfungsbehörde vorgelegt und ist auch noch nicht veröffentlicht worden.

Die Promotionsordnung der Fakultät Maschinenwesen vom 1. Juli 2001 wird anerkannt.

Dresden, November 2013

---

Kerstin Bernert



## Abstract

This thesis discusses spin-transfer torques in MgO-based magnetic tunnel junctions. The voltage-field switching phase diagrams have been experimentally determined for in-plane CoFeB/MgO/CoFeB magnetic tunnel junctions. In order to limit the effect of thermal activation, experiments have been carried out using nanosecond voltage pulses, as well as at low-temperature (4.2 K).

The bias-dependence of the two spin-torque terms (Slonczewski-like and field-like) has been determined from thermally-excited ferromagnetic resonance measurements, yielding values which are in good agreement with previous reports. Additionally, material parameters such as the effective magnetisation and the damping factor have also been extracted.

Using these values as input, the switching voltages as function of the applied magnetic field have been calculated numerically and analytically by solving the modified Landau-Lifshitz-Gilbert equation. Unlike previous studies, the field-like spin-torque has also been included. Moreover, different configurations have been considered for the magnetic anisotropy directions of the reference and free layer, respectively.

## Kurzzusammenfassung

Diese Arbeit befasst sich mit Spin-Transfer-Torque-Effekten in MgO-basierten magnetischen Tunnelstrukturen. Die Phasendiagramme als Funktion von Spannung und Magnetfeld von CoFeB/MgO/CoFeB-Tunnelstrukturen mit Magnetisierung in der Ebene wurden experimentell bestimmt. Um thermische Anregungseffekte zu limitieren, wurden die Experimente einerseits mit nanosekundenlangen Spannungspulsen und andererseits bei niedrigen Temperaturen (4.2 K) durchgeführt.

Die Spannungsabhängigkeit der beiden Spin-Torque-Parameter (in-plane und senkrechter Spin-Transfer-Torque) wurde aus Messungen der thermisch angeregten ferromagnetischen Resonanz bestimmt, wobei sich Werte ergaben, die gut mit vorangegangenen Untersuchungen übereinstimmen. Zusätzlich wurden Werte für Materialparameter wie die effektive Magnetisierung und den Dämpfungsparameter gewonnen.

Unter Verwendung der erhaltenen Werte wurden die Schaltspannungen als Funktion des angelegten Magnetfeldes analytisch und numerisch berechnet, indem die erweiterte Landau-Lifshitz-Gilbert-Gleichung gelöst wurde. Im Gegensatz zu vorangegangenen Untersuchungen wurde der senkrechte Spin-Transfer-Torque dabei mit einbezogen. Darüber hinaus wurden verschiedene Konfigurationen für die Richtung der magnetischen Anisotropie der freien und fixierten Schicht berücksichtigt.

# Contents

---

<b>1</b>	<b>Introduction</b>	<b>1</b>
<b>2</b>	<b>Fundamentals</b>	<b>5</b>
2.1	Magnetoresistance . . . . .	6
2.1.1	Giant magnetoresistance . . . . .	6
2.1.2	Tunnel magnetoresistance . . . . .	8
2.2	Spin-transfer torque effect . . . . .	13
2.2.1	Physical picture of the STT . . . . .	13
2.2.2	In-plane and perpendicular STT . . . . .	16
2.3	Equation of motion for the magnetisation . . . . .	17
2.3.1	The Landau-Lifshitz-Gilbert equation . . . . .	17
2.3.2	Extension including spin-transfer-torque (LLGS) . . . . .	18
2.4	Applications of MR and spin-transfer torque . . . . .	19
2.4.1	Read heads in hard disk drives . . . . .	20
2.4.2	Spin-transfer torque magnetic random access memory . . . . .	21
2.5	STT effects in magnetic tunnel junctions . . . . .	23
2.5.1	Current-induced switching . . . . .	23
2.5.2	Magnetisation precession . . . . .	35
2.5.3	Bias-dependence of STT . . . . .	36
2.5.4	Back-hopping . . . . .	41
<b>3</b>	<b>Experimental</b>	<b>43</b>
3.1	Samples . . . . .	43
3.1.1	Stack composition . . . . .	43
3.1.2	Properties of samples used in this work . . . . .	46

---

3.2	Experimental setup . . . . .	47
3.2.1	Overview of equipment for the different measurement techniques	47
3.2.2	Electromagnet and Kepco power supply . . . . .	48
3.2.3	Contacting of the sample . . . . .	49
3.2.4	Principle specifications of equipment . . . . .	50
3.3	Experimental techniques . . . . .	53
3.3.1	Measurement of DC R-H and R-I loops . . . . .	53
3.3.2	Measurement of phase diagrams: off and on-pulse . . . . .	55
3.3.3	Thermally-excited ferromagnetic resonance . . . . .	61
<b>4</b>	<b>Results and discussion</b>	<b>65</b>
4.1	Switching phase diagrams of MTJs . . . . .	65
4.1.1	Theory: Calculating the phase diagram . . . . .	66
4.1.2	Experimental phase diagrams . . . . .	81
4.2	Thermally excited ferromagnetic resonance . . . . .	95
4.2.1	Smoothing and fitting of raw data . . . . .	96
4.2.2	Determination of $M_s$ . . . . .	98
4.2.3	Signal evolution with bias voltage . . . . .	100
4.2.4	Analysis of peak position: perpendicular STT . . . . .	102
4.2.5	Analysis of peak linewidth . . . . .	104
<b>5</b>	<b>Summary and outlook</b>	<b>107</b>
<b>A</b>	<b>Appendix</b>	<b>113</b>
	<b>List of figures</b>	<b>123</b>
	<b>List of tables</b>	<b>125</b>
	<b>Bibliography</b>	<b>136</b>



## Acknowledgement

First, I want to thank both Prof. Gianarelio Cuniberti and Prof. Jürgen Faßbender for supervising this PhD thesis and introducing me into their field of science. I am very thankful to Prof. Jürgen Faßbender and Prof. Manfred Helm for giving me the opportunity to work at the Helmholtz-Zentrum Dresden-Rossendorf, to use all the equipment and for allowing me to travel to several international conferences during my PhD time. I thank Dr. Jürgen Lindner for all his support and many fruitful discussions and suggestions.

I also want to deeply thank Dr. Alina Deac for having the honour to be her first PhD student, for sharing her broad knowledge and repeatedly explaining all the details until I finally got it. Last but not least for her sudden flash of inspiration to link the perpendicular STT to the back-hopping, which led to this thesis.

The next most important people for my PhD were the three post-docs Dr. Christopher Bunce, Dr. Ciarán Fowley and Dr. Volker Sluka whom I could always ask when I was stuck - Chris not only showed me the whole world of LabView and was helping me so much with the setup when I started my PhD, he also explained me how to prepare a proper English tea and improved my language skills (including puns and humour). The complementary pair of Ciarán and Volker was an ideal source of expert knowledge both on experimental and theoretical questions. I want to thank Volker especially for his patience and committed explanations of all physical processes involved in this thesis - the private physics lessons were extremely helpful and not in vain! Ciarán was always there to help and give clear and brief advice in case of experimental problems. I will miss the happy and cheerful atmosphere in the I' office!

I also want to thank all my countless other office mates for the nice atmosphere, but especially my 'fellow PhD student' Dr. Marcel Höwler for his tireless effort of manufacturing the perfect sample, his constant support and his good mood even in spite of the famous never-ending flashing LED of the current source.

I want to thank Yuriy Aleksandrov, Ewa Kowalska, my summer student Sylvain Mathonnière and the whole spintronics group for all the discussions and the friendly and open atmosphere in the group.

I am very thankful to Dr. Jonathan Sun, Prof. Stéphane Mangin and Prof. Jeffrey McCord who were supplying me with 'THE' sample to finally start measuring.

Furthermore, I want to thank Dr. Kay Potzger for his administrative help and for his blunt refreshing statements. I want to thank Dr. Artur Erbe both for the discussions and

the easy access to his low-temperature setup as well as for countless musical rehearsals which formed a good balance to work. Dr. Jochen Grebing needs to be thanked for his immediate help with programming and setting up the low-temperature phase diagram measurement at the end of the PhD, fighting all obstacles until it finally worked. I also want to thank Dr. Huadong Gan, who programmed the first LabView programme of the off-pulse measurement. I thank Dr. Kilian Lenz for his quick answers and help to all my questions concerning lab equipment or LabView programming and Andreas Henschke for all his proper and reliable technical and administrative support.

A big thank you goes to Anja Banholzer, Julia Osten, Manuel Langer and all the others for the countless relaxing tea/coffee breaks and loads of biscuits that lifted my mood.

I want to thank everybody else of the institute (also from the FWIO department) for their support, the friendly atmosphere and help whenever needed.

A lot of people have checked this thesis thoroughly, I think it is the best checked thesis I have written so far! I want to thank everybody who took the time and gave me the possibility to improve it.

Finally, a big thank you for my parents for making me curious on the world of science and supporting me in all possible ways. I want to thank them and Sebastian's family for their support and spontaneous child-care whenever needed and possible. Last but not least I want to thank Sebastian for all his support and for teaching me optimistic thinking and Fabian for being a large motivation and opening my eyes on how nature is still a miracle.

# Introduction

---

A spin-polarised current flowing through a ferromagnetic layer transfers angular momentum to the local magnetisation. This can be expressed in terms of a pseudo-torque (known as spin-transfer torque, STT) [1, 2], which allows for the manipulation of magnetic moments even in the absence of external magnetic fields. Specifically, two types of effects can be induced: magnetisation reversal and steady state precession.

A number of possible applications have been suggested, exploiting STT effects. Examples are frequency-tunable current-driven microwave oscillators for mobile telecommunications (based on STT-driven precession) or magnetic random access memory (MRAM) cells (using STT-induced switching as writing scheme). The STT-MRAM has the potential to serve as a 'universal' memory combining advantages such as non-volatility, unlimited endurance, high speed, high density and error-free addressing. The main challenge for STT-MRAM cells nowadays is to achieve sufficiently low write currents to be transistor-compatible, while maintaining good thermal stability. The first commercial STT-MRAM based on Fe/MgO/Fe-type magnetic tunnel junctions (MTJs) was produced in November 2012 by Everspin Technologies and is currently being tested by selected costumers. However, the estimated cost for a 1 GB unit remains about 50 times higher than that for a conventional NAND-Flash memory [3].

A spin-polarised current applied through an MgO-based MTJ induces an STT which consists of two components: the in-plane 'damping-like' and the perpendicular 'field-like'. Unlike in metallic structures, where the perpendicular STT is usually negligible, it has been demonstrated that in MgO-MTJs it can reach up to 30 % of the in-plane torque [4, 5] and therefore needs to be considered. The magnitude of the two spin-transfer torque components and their voltage dependence are predicted to depend on the symmetry of the structure, as well as the layer thicknesses, the magnitude of the exchange splitting and the interfacial microstructure [6, 7]. Given its direct impact on

the switching current for STT-MRAM, this topic is currently widely discussed in the literature, with various groups reporting partially conflicting results.

For the design of industrially-competitive MRAM devices, the switching mechanism needs to be understood and reliably controlled. Although this has previously been achieved in metallic devices, it has been reported that MgO-based MTJs exhibit a behaviour referred to as 'back-hopping', whereby reliable reversal is achieved at the critical voltage, but higher voltages induce telegraph-noise-like behaviour. As MRAM devices are typically operated in 'overdrive' (voltages above the threshold for switching) in order to compensate for sample-to-sample variation, back-hopping has a direct impact on writing reliability. Back-hopping is typically attributed to thermally activated magnetisation reversal [8, 9, 10, 11]. Here, we address this issue from a different perspective. Specifically, we analyse the impact of the perpendicular STT on the switching and the switching reliability.

Chapter 2 starts with the theoretical background of magnetoresistance (MR) and STT. The equation of motion for the magnetisation (known as the Landau-Lifshitz-Gilbert (LLG) equation) is introduced and a brief overview about the literature concerning STT effects in MgO-MTJs is presented. Two applications of the MR and STT are presented: the read heads for hard disk drives and the STT-MRAM, respectively.

Chapter 3 describes the samples used and the experimental setup which was specifically developed in order to investigate STT-induced effects. The techniques employed during this PhD are presented: field- and voltage-driven magnetisation reversal and thermally-excited ferromagnetic resonance (TE-FMR). Both DC and high frequency (nanosecond pulse and real-time switching) experiments are described.

In chapter 4, the experimental results, as well as the calculations for determining the switching voltages are discussed. Specifically, we solve (analytically and numerically) the extended LLG equation, in order to obtain the voltage-field switching phase diagrams for MgO-based MTJs with different geometries. We demonstrate that for in-plane MTJs, the perpendicular STT can lead to back-hopping and its bias-dependence can in principle be directly extracted from the curvature of a specific critical line of the phase diagram. While the calculations were carried out at 0 K, in practice, both switching by field and by current are (at least partially) thermally activated. For better comparison with theory, switching experiments have been conducted with nanosecond voltage pulses as well as at low temperature (4.2 K). Moreover, the real-time switching behaviour was analysed with single-shot oscilloscope traces on the reflected pulses. The bias-dependence of the two STT terms was determined from bias-dependent thermally-

excited ferromagnetic resonance (TE-FMR) experiments and is presented as the last part of chapter 4.

Finally, chapter 5 summarises the results and proposes a series of further measurements as an outlook.



# 2

## Fundamentals

---

This chapter will give an introduction into the background of magnetotransport phenomena and their applications in so far that they are relevant for this work.

The relative orientation of the magnetisation of two magnetic layers with a non-magnetic spacer layer can influence the electric current flow through the layers, which is referred to as magnetoresistance. Both the giant magnetoresistance (GMR) in metallic structures and the tunnel magnetoresistance (TMR) in magnetic tunnel junctions (MTJs) effects will be introduced.

Then the inverse phenomenon, the so-called spin-transfer torque (STT), in which a current flow influences the magnetisation direction by a transfer of angular momentum, is explained in a simple physical picture. It is emphasised that the STT consists of two components, namely the in-plane and the perpendicular STT, which both have to be taken into account for the case of magnetic tunnel junctions investigated in this work.

The equation that describes the motion of the magnetisation in a magnetic field, the Landau-Lifshitz-Gilbert equation (LLG) is introduced in section 2.3. Its modification including the STT is discussed.

Two important applications of the magnetoresistance and STT effect are the read head in magnetic storage devices and magnetic access random memory (MRAM). They will be presented before STT-induced phenomena in magnetic tunnel junctions are discussed in more detail. These include the current-induced magnetisation switching (CIMS) and current-induced precession of the magnetisation.

The background of the research on two phenomena that have been widely debated on is summarised in the last two subsections of this chapter: the bias-dependence of the STT and the perturbing 'back-hopping' effect, which is highly relevant for an industrial application of MTJs as MRAM elements. Both effects are the core of the studies presented in the next chapters.

## 2.1 Magnetoresistance

Magnetoresistance (MR) is the change of resistance of a conductor by an applied magnetic field [12]. In magnetic materials, the spin polarisation of the electrons results in large (up to several 100 %) MR effects. In this section, the giant magnetoresistance and the tunnel magnetoresistance effect will be briefly explained.

### 2.1.1 Giant magnetoresistance

The giant magnetoresistance (GMR) effect is an interface effect due to spin-dependent scattering observed in ferromagnetic multilayers [13]. The conductivity of the stack depends on the relative magnetisation direction of the layer. In the following a system with two ferromagnetic layers and a non-magnetic layer in between is discussed. Here, a change in the relative angle between the magnetisations of the two ferromagnetic layers changes the total resistance of the structure. In general, the effect has been investigated in two different geometries, the current-in-plane (CIP) and current-perpendicular-to-plane (CPP) geometry. Since all measurements in this thesis are performed in the latter geometry, this chapter will focus on the CPP-GMR.

The so-called 'two current-model' of Mott [14] explains the GMR effect in a phenomenological picture. This phenomenon is caused by a difference in the conductivity for the two currents from majority and minority electrons. Majority (minority) relates to the direction of the projection of their spin being antiparallel (parallel) to the local magnetisation, whereas their magnetic moment is parallel (antiparallel). The terms 'spin-up' and 'spin-down' are defined in relation to a fixed quantisation axis (typically the magnetisation direction of the ferromagnet).

The main contribution to the current in a ferromagnetic transition metal are the electrons from the s subband, whereas the specific resistivity is mainly caused by scattering of these electrons into free states in the d subbands at an energy close to the Fermi level [15]. When neglecting spin-flip events, which is justified if the barrier is thin enough, the two currents from majority and minority electrons can be treated independently and the conductivities for the two channels can be summed up in a parallel circuit.

In a ferromagnetic material, electrons with opposite spin form different electronic bandstructures due to the exchange splitting. For the example shown in figure 2.1, the d-subband of the majority electrons is reduced in energy with respect to the Fermi



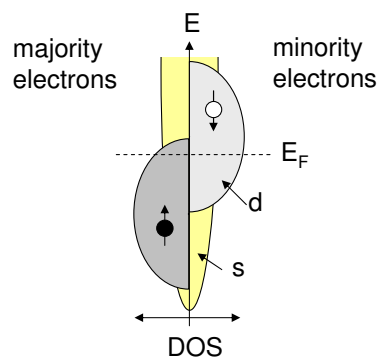


Figure 2.1: Schematic of the spin-dependent density of states in a ferromagnet. The exchange splitting of the localised d-electrons leads to a different density of states at the Fermi level. Therefore the s-d scattering is much smaller for majority than minority electrons and the conductivities of the two currents are different.

energy, so that it is almost completely filled and its density of states (DOS) at the Fermi level is much smaller than that of the minority electrons. Therefore, for this example, less scattering can take place in the case of majority electrons resulting in a higher conductivity for this spin channel. (In general, it can also be opposite, so that the minority carriers are conducting better than the majority carriers.)

We can now investigate the GMR effect for a symmetric spin-valve (where both ferromagnetic layers are similar) for the two cases of the magnetisations of the two ferromagnetic layers being parallel (P) and antiparallel (AP) (figure 2.2). For a symmetric structure, if  $R_1$  and  $R_2$  are the resistances for the majority and minority spins in each magnet, the total resistance in the P and AP state is given by

$$R_P = \frac{2R_1R_2}{R_1 + R_2} \quad (2.1)$$

$$R_{AP} = \frac{1}{2}(R_1 + R_2). \quad (2.2)$$

From this it can be found that

$$R_{AP} = R_P + \frac{(R_1 - R_2)^2}{2(R_1 + R_2)}. \quad (2.3)$$

Now it is easily visible that the resistance in the AP state is larger than in the P state.

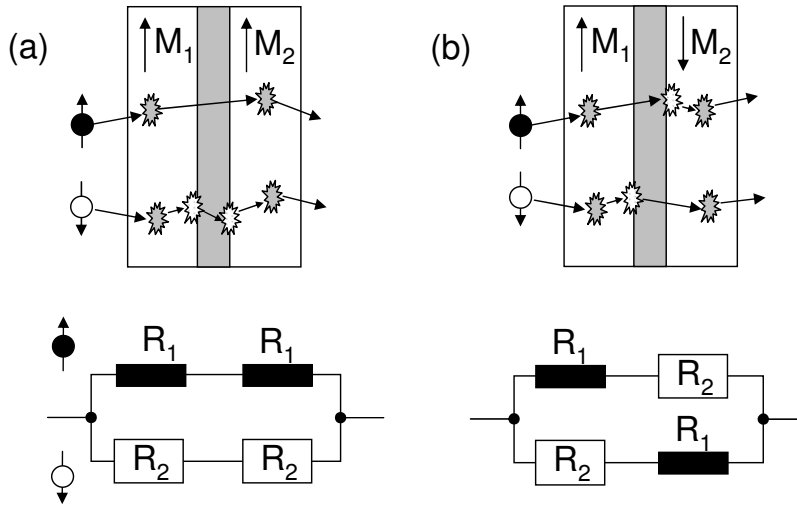


Figure 2.2: Phenomenological picture for the two-current model of the CPP GMR effect. The two magnetic layers are in (a) parallel and (b) antiparallel alignment. The scattering at the interfaces is spin-dependent: It is low if the magnetic moment is parallel to the magnetisation direction (resulting in resistance  $R_1$ ) and large for the opposite case ( $R_2$ ). The total resistance for crossing all three layers can be calculated from the circuit below.

This is a direct result from the fact that the investigated structure is symmetric; additionally it is independent from  $R_1$  or  $R_2$  being lower. The GMR ratio is defined as

$$GMR = \frac{(R_{AP} - R_P)}{R_P}. \quad (2.4)$$

It should be noted that for asymmetric spin-valves and certain material combinations the GMR can be negative ( $R_{AP} < R_P$ ). This happens if the conductivity for minority spins is larger than for majority spins in one of the two ferromagnets.

### 2.1.2 Tunnel magnetoresistance

The tunnel magnetoresistance (TMR) effect can be observed in magnetic tunnel junctions (MTJs) consisting of two ferromagnetic layers separated by an insulating spacer layer. The conduction is due to quantum mechanical tunneling and the origin of the TMR effect is the spin-dependence of the tunneling. As in the GMR, the resistance measured via applying a current perpendicular to the layer stack depends on the relative angle between the magnetisation directions of the two ferromagnetic layers. The TMR ratio is defined in the same way as the GMR (eq. (2.4)).

The first TMR measurement was realised by Jullière in 1975, who determined the conductance change in Fe-Ge-Co samples for parallel and antiparallel configurations at low temperatures (4.2 K) [16]. Measuring the TMR at room temperatures was achieved in the 1990s by Yaoi et al. [17] and Moodera et al. [18] using amorphous  $\text{Al}_2\text{O}_3$  barriers and reaching TMR values around 1-10 %.

In 2004, a change in the barrier material finally led to a drastic increase in the TMR values: Two groups, Yuasa et al. (180 % [19]) and Parkin et al. (220 % [20]) managed the fabrication process of epitaxially grown Fe/MgO/Fe MTJs. The highest TMR value for such a kind of structure up to date is 604 % at room temperature (Ikeda et al. in 2008 [21]).

### 2.1.2.1 The Jullière model of TMR

To explain the TMR effect, Jullière proposed a model [16] which relates the conductance to the density of states. Since the DOS is spin-dependent in a ferromagnetic material, the number of states that are actively involved in the transport process, i.e. states at or close to the Fermi level, differ. This is exemplarily shown in figure 2.3. Assuming that during the tunneling process the spin of the electrons does not flip, the

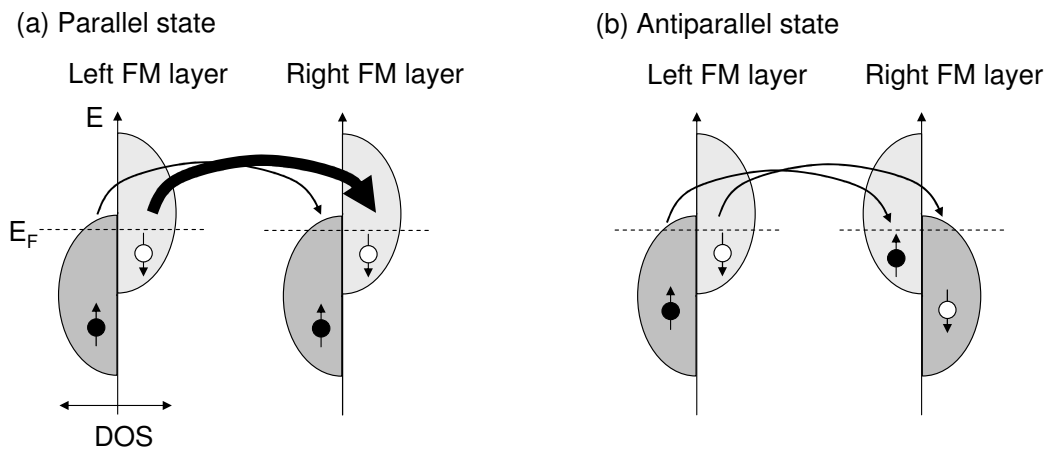


Figure 2.3: DOS depending on the energy for the Jullière model of the TMR effect for (a) parallel and (b) antiparallel alignment of the magnetisation of the two ferromagnetic layers. The current flowing in the two subchannels is indicated by arrows. Due to the large DOS in both layers the total current is largest for the case of parallel alignment.

tunneling probability for the majority and minority electrons is not equal [15]. For the case of parallel configuration, the majority electrons tunnel to majority electron states and the minority electrons into minority states. For antiparallel configuration, the tun-

neling occurs from majority to minority states and vice versa. Since the tunneling rate is proportional to the DOS of the start and end states, the resistances are different for the P and AP case. In the AP case, the two channel currents can be described by two equal resistances while in the P case a very small and a very large resistance are in parallel. Therefore, the total resistance is smallest in the parallel case.

In order to derive a formula for the TMR, the current can be related to the product of the DOS  $n$  of the two sides:

$$I_{total} = I_{\uparrow} + I_{\downarrow}, \quad (2.5)$$

$$I_P \propto n_{L\uparrow}n_{R\uparrow} + n_{L\downarrow}n_{R\downarrow}, \quad (2.6)$$

$$I_{AP} \propto n_{L\uparrow}n_{R\downarrow} + n_{L\downarrow}n_{R\uparrow}, \quad (2.7)$$

where L and R stand for the two ferromagnetic layers,  $\uparrow$  and  $\downarrow$  for the majority and minority spin channels, respectively. The TMR is therefore given by

$$TMR = \frac{R_{AP} - R_P}{R_P} = \frac{G_P - G_{AP}}{G_{AP}} = \frac{n_{L\uparrow}n_{R\uparrow} + n_{L\downarrow}n_{R\downarrow} - (n_{L\uparrow}n_{R\downarrow} + n_{L\downarrow}n_{R\uparrow})}{n_{L\uparrow}n_{R\downarrow} + n_{L\downarrow}n_{R\uparrow}} \quad (2.8)$$

$$TMR = \frac{(n_{L\uparrow} - n_{L\downarrow})(n_{R\uparrow} - n_{R\downarrow})}{n_{L\uparrow}n_{R\downarrow} + n_{L\downarrow}n_{R\uparrow}} = \frac{2P_L P_R}{1 - P_L P_R} \quad (2.9)$$

and the two polarisations are defined as  $P_L = \frac{n_{L\uparrow} - n_{L\downarrow}}{n_{L\uparrow} + n_{L\downarrow}}$  and  $P_R = \frac{n_{R\uparrow} - n_{R\downarrow}}{n_{R\uparrow} + n_{R\downarrow}}$ . As can be seen from eq. (2.9), the maximum TMR will be expected if the polarisation is 100 %, which is the case for example for Heusler alloys [12].

In a symmetric junction ( $P_L = P_R$ ), the polarisation can therefore be calculated from the two resistance levels in the P and AP state in the limit of zero voltage by using the following formula [7]:

$$P = \sqrt{\left(\frac{R_{AP} - R_P}{R_{AP} + R_P}\right)}. \quad (2.10)$$

### 2.1.2.2 Fe/MgO(100)/Fe magnetic tunnel junctions

In contrast to tunnel barriers consisting of amorphous  $\text{Al}_2\text{O}_3$ , an MgO barrier can be grown epitaxially on Fe since the lattice mismatch is small. The fabrication of these barriers is very demanding. They are typically realised by a deposition of MgO on amorphous CoFeB with an additional annealing of the structure above 300 °C leading to a crystallisation of CoFeB in the (001) orientation [20]. In 2001, already before

the first experimental fabrication, two groups, Butler et al. [22] and Mathon et al. [23] independently predicted a very high TMR from calculations of the electronic structure for Fe/MgO/Fe tunnel junctions due to coherent tunneling.

At interfaces and in thin tunnel barriers, the so-called 'complex bandstructure' has to be taken into account [12]. That means that there exist states in the thin MgO barrier with a complex wave vector, i.e. an evanescent or exponentially decaying state in the bandgap of a material. The state with the slowest decay rate is the so-called  $\Delta_1$  state [22]. Its wave function is symmetric with respect to the barrier-normal axis. In coherent tunneling, only conduction electrons with symmetric wave functions are connected to the electronic states in the barrier region [19]. Due to these symmetry restrictions, only the  $\Delta_1$  state in Fe can couple to the decaying state in the MgO. This is possible around the Fermi energy  $E_F$  in the case of majority electrons, but not until  $E = E_F + 2$  eV for minority electrons due to the exchange splitting in the Fe [12], resulting in the huge difference in transmission for the P and AP alignment of the two ferromagnetic electrodes.

The tunneling densities of states (the DOS of corresponding Bloch states on both sides of the interface) for the P and AP alignment were calculated by Butler et al. [22] and the results are shown in figure 2.4. In the P state the main difference is the absence of the  $\Delta_1$  band for the minority carriers in the Fe. Therefore, the tunneling is dominated by the  $\Delta_1$  majority spin channel, which couples efficiently with a slowly decaying state in the MgO barrier resulting in a good conductivity.

In the AP state, the majority  $\Delta_1$  states on the one side do not find corresponding states at the other side of the barrier since there, the electrons suddenly are minority carriers (lower left panel of figure 2.4). This is visible in the decay of the  $\Delta_1$  channel in the Fe, resulting in a total reflection of the electrons. Therefore the tunneling is dominated by the  $\Delta_5$  channel, which has a constant, large enough number of minority states in the Fe to couple to but decays rather quickly in the MgO barrier. The  $\Delta_{2'}$  state decays extremely fast and does not contribute to the conduction. A similar total reflection due to decaying Fe states occurs for the  $\Delta_2$  band minority carriers entering from the left after passing the MgO barrier (lower right panel of figure 2.4). Overall, this results in a much higher resistance for the AP compared to the P state.

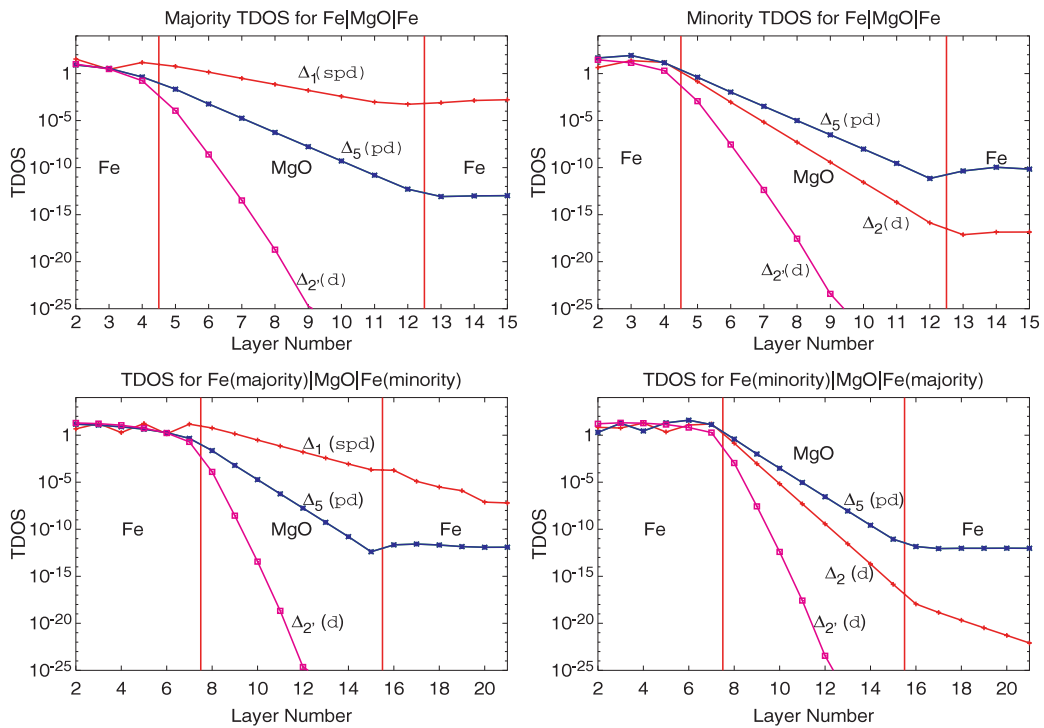


Figure 2.4: Tunneling density of states at normal incidence ( $\vec{k}_{\parallel} = 0$ ) for Fe(100)/MgO/Fe(100), taken from [24]. The two upper panels show the DOS for P alignment (left for majority electrons, right for minority electrons), while the lower panels show the AP alignment DOS. The curve labelling refers to the symmetry of the incident Bloch state at the left Fe electrode.

## 2.2 Spin-transfer torque effect

A spin polarised current flowing through a ferromagnetic layer will exert a torque on its magnetisation. The so-called spin-transfer torque effect (STT) was theoretically predicted independently by Slonczewski [1] and Berger [2] in 1996.

To achieve the high current density needed for a sufficiently high spin-transfer torque ( $>10^7$  A/cm<sup>2</sup> [12]), the lateral size of the devices needs to be constricted. Therefore the samples either use a point-contact on an extended multilayer substrate or they are shaped into nanopillars with lateral cross sections smaller than about 250 nm, so that the STT is larger than the Oersted field induced by the current [25]. The first experimental observation of spin-transfer torque-induced magnetisation switching of the magnetisation was achieved by Myers et al. in 1999 for a Co/Cu/Co point contact geometry [26] and by Katine et al. in 2000 for Co/Cu/Co nanopillars [27]. Following shortly after in 2003, Kiselev et al. reported the first STT-induced magnetisation dynamics in Co/Cu/Co nanopillars [28].

### 2.2.1 Physical picture of the STT

For a physical picture of the STT, we consider two ferromagnetic layers (FM 1 and FM 2, see figure 2.5) with a thin non-magnetic spacer layer in between. The spacer layer thickness is below its spin-diffusion length so that the spin polarisation is preserved. The coercivity of one of the two layers (referred to as the 'fixed' or 'reference' layer) is significantly larger than that of the other (referred to as the 'free' layer), where a switching of the magnetisation can be achieved at comparatively low external magnetic fields. This can be realised by, e.g.

- using different materials for each of the two layers,
- using the same material but different thicknesses of the layers,
- coupling the fixed layer to another ferromagnetic layer (building a so-called synthetic antiferromagnet (SAF)) and by
- exchange coupling the fixed layer to an antiferromagnet.

In state-of-the-art devices, typically the last two methods are combined leading to reduced stray fields near the free layer and a magnetically stable fixed layer in the required field, temperature and current ranges. Additionally, for an application as a memory element, the two magnetic configurations should be stable at zero external magnetic field.

The nanopillar shape is often preferred since it requires less current density for STT excitations compared to a point-contact geometry. The reason is that in the latter, STT excitations must reorient a small area in the extended magnetic film, and thus have to overcome a strong exchange interaction [25].

Let us first consider the case of the two magnetisation directions of FM 1 and FM 2, which are tilted by an angle of  $\theta$ , and the electron flow from the fixed to the free layer (figure 2.5 (a)). The wave function of the incident electrons corresponds to a super-

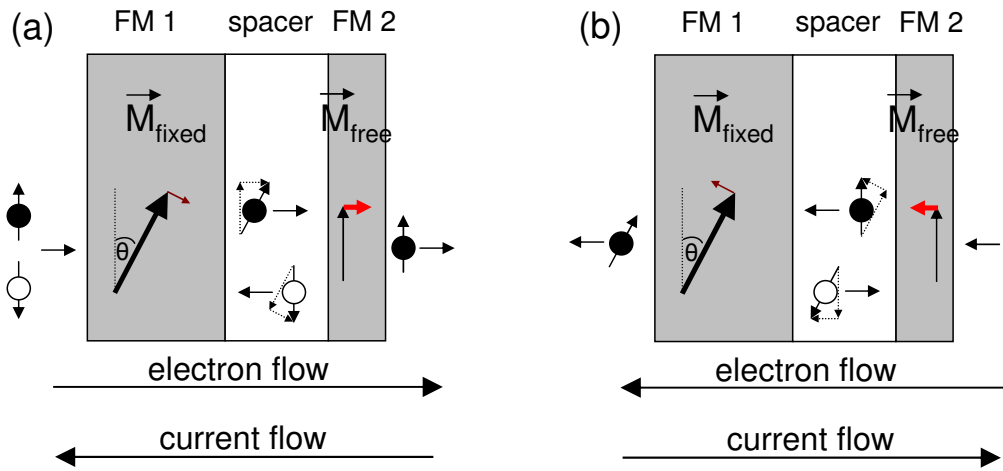


Figure 2.5: Physical picture of spin-transfer torque in a ferromagnet/spacer/ferromagnet structure for electron flow directions favouring (a) parallel and (b) antiparallel alignment. Due to a larger coercivity, the magnetisation of FM 1 does not rotate due to the STT (thin brown arrows), whereas the magnetisation of FM 2 follows the STT (red arrows).

position of spin-up and spin-down components with respect to the quantisation axis of the magnetisation. After the electrons have passed the first ferromagnet (FM 1), their magnetic moments will be polarised in the direction of the magnetisation of FM 1 due to the spin-dependent conductivity in the ferromagnet.

When the electrons enter the second ferromagnet (FM 2) they lose transverse angular momentum due to three different processes: Spin filtering, differential spin reflection and spatial spin precession [25, 29]. Since the angular momentum has to be conserved, it is absorbed by the FM 2 and acts as a torque on the magnetisation.

The effect of spin filtering is caused by the spin-dependency of the reflection and transmission processes. The reflected and transmitted wave functions for an electron are modified linear combinations of majority and minority components compared to the incident wave function. It was shown that the spin-dependent reflection and trans-



mission causes a discontinuity in the transverse spin current, leading to a spin-transfer torque [29]. The spin filtering is an effect that is experienced by each electron individually. In the extreme case of perfect spin filtering, only electrons with the magnetic moment aligned with the magnetisation of the ferromagnet will pass the layer, whereas those with opposite magnetic moment are reflected (see figure 2.5 (a)).

Spatial spin precession occurs because the electrons experience exchange splitting in the ferromagnet, which leads to a spin-dependent kinetic energy and therefore spin-dependent wave vectors. When the electrons propagate away from the interface, due to the different wave vectors, there is a spatial precession of the transverse spin-component around the axis of the magnetisation of FM 2. When summed up over all conduction electrons, a rapid dephasing occurs after a short distance from the interface. This leads to a rapid decay of the total transverse spin component of the conduction electrons with increasing distance to the interface, which is absorbed by the magnetisation.

The effect of differential spin reflection is a quantum mechanical effect due to the rotation of the spin upon reflection and transmission. This rotation can also contribute to the spin-transfer torque. The angle of rotation depends on the wave vector of the incoming electron. Since the wave vectors are distributed, when summing over all resulting spin vectors, the net outgoing transverse angular momentum is reduced, i.e. it has been transferred to the magnetisation.

For ferromagnets like the 3d transition metals, about 50 % of the transversal component are absorbed, and so the transmitted and reflected components still have a transversal spin-component [12].

The reflected electrons are polarised with the magnetic moment being antiparallel to the magnetisation of FM 2 and travel back to FM 1, where they experience an absorption of the transversal component which acts as a torque on the magnetisation of FM 1. However, since the fixed layer has a large total magnetic moment, the magnetisation will not rotate due to the STT. In contrast, the free layer magnetisation will switch if the STT is large enough to reach a parallel alignment to the magnetisation of FM 1.

For the opposite direction of electron flow from the free to the fixed layer (figure 2.5 (b)), the torques point in the opposite direction. It is then the reflected electrons which exert a torque on the free layer magnetisation, leading to a rotation of the magnetisation towards antiparallel alignment.

Typically, magnetic nanopillars have an elliptical shape, so that due to shape anisotropy there are two stable magnetisation states for the free layer. By changing the polarity of the current, i.e. the direction of the electron flow, the STT can switch the

magnetisation in either of the two states. The STT might also generate precessional motion of the magnetisation, as will be discussed further in chapter 2.5.2.

In general, the STT is only non-zero if the two magnetisation directions are not collinear. However, this condition is satisfied at finite temperature due to thermal fluctuations of the magnetisation.

## 2.2.2 In-plane and perpendicular STT

### 2.2.2.1 In-plane STT

The in-plane STT is the STT as introduced by Slonczewski in 1996 [1]. The term 'in-plane' refers to it lying in the plane defined by the free layer magnetisation and the magnetic moment of the incoming electron. It is defined as [25]:

$$\left(\frac{d\vec{m}}{dt}\right)_{STT_{\parallel}} = -\eta_{\parallel}(\theta) \frac{\mu_B \vec{j}}{e \cdot d} \vec{m} \times (\vec{m} \times \vec{p}), \quad (2.11)$$

where  $\vec{m}$  and  $\vec{p}$  are the unit vectors in the direction of the free layer magnetisation and the magnetic moment of the incoming electrons (or the fixed layer magnetisation),  $\mu_B$  is the Bohr magneton,  $e$  is the elementary charge ( $e > 0$ ) and  $d$  is the thickness of the layer.  $\vec{j}$  is the current density, defined so that for positive currents the electrons flow from the fixed to the free layer and the in-plane STT favours the parallel alignment.  $\theta$  is the angle between the incoming electron polarisation and the free layer magnetisation:  $\cos(\theta) = \vec{p} \cdot \vec{m}$ .

The **angular dependence**  $\eta_{\parallel}(\theta)$  describes that the spin torque in general is not independent of the relative orientations of the two magnetisations.

If  $\eta_{\parallel}$  is constant, then the STT would be symmetric to the maximum at the angle of  $90^\circ$  between  $\vec{m}$  and  $\vec{p}$  and the angular dependence would be solely described by the cross product. However, for metallic multilayers, transport calculations predict  $\eta_{\parallel}$  not to be constant, so that an additional angular dependence is induced and the torques are not symmetric around  $90^\circ$  anymore. This arises from the different amounts of spin accumulation for alignments close to P or AP [25]. The angular dependence is described with the asymmetry parameter  $\Lambda$  and the polarisation  $P$  [30]:

$$\eta_{\parallel}(\theta) \propto \frac{P\Lambda}{\Lambda \cos^2(\frac{\theta}{2}) + \frac{1}{\Lambda} \sin^2(\frac{\theta}{2})}. \quad (2.12)$$

### 2.2.2.2 Perpendicular STT

There is another contribution to the STT which is perpendicular to the plane defined by the free layer magnetisation  $\vec{m}$  and the moment of the incoming electrons  $\vec{p}$  in the form [25]

$$\left(\frac{d\vec{m}}{dt}\right)_{STT_{\perp}} = \eta_{\perp}(\theta) \frac{\mu_B \vec{j}}{e \cdot d} \vec{m} \times \vec{p}. \quad (2.13)$$

It is also called 'field-like' STT since it has the same form as a torque that would result from a field aligned parallel or antiparallel to the fixed layer magnetisation. In metallic multilayer devices, the perpendicular torque was calculated to be in the range of typically 1-3 % of the in-plane torque [25, 31]. This was confirmed by STT-ferromagnetic resonance (ST-FMR) experiments on metallic IrMn/Py/Cu/Py spin-valves, where the perpendicular STT was determined to be less than 1 % of the in-plane torque for biases up to 2 mA [4].

For tunnel junctions, the bias-dependent part of the perpendicular STT is predicted to be larger than for metallic devices [31, 32]. Theodonis et al. predicted a quadratic bias-dependence for symmetric tunnel junctions (similar to what should be expected in metallic structures), but additional complicating facts might play a role (e.g. angular momentum loss from hot electrons to the excitation of short-wavelength spin waves). For non-symmetric tunnel junctions, where the free and fixed layer are not identical, an additional linear dependence on the voltage is expected [25]. A detailed discussion of the current research on the bias-dependence of the STT in MTJs can be found in section 2.5.3.

## 2.3 Equation of motion for the magnetisation

### 2.3.1 The Landau-Lifshitz-Gilbert equation

The Landau-Lifshitz-Gilbert equation (LLG) describes the magnetisation dynamics of a magnetic moment in a macrospin approximation. It was found that the Landau-Lifshitz equation established beforehand could not account for large damping problems. In his PhD thesis in 1956, Gilbert suggested a different phenomenological damping term in order to take large damping into account. The theory was reformulated concisely in

2004 [33]. The LLG equation can be written as:

$$\frac{d\vec{m}}{dt} = -\gamma(\vec{m} \times \vec{H}_{\text{eff}}) + \alpha \left( \vec{m} \times \frac{d\vec{m}}{dt} \right). \quad (2.14)$$

For the special case of describing the free layer magnetisation of a spin-valve or MTJ,  $\vec{m}$  is the unit vector parallel to the magnetisation of the free layer ( $\vec{m} = \frac{\vec{M}}{M_s}$ ,  $M_s$  is the saturation magnetisation).  $\alpha$  is the Gilbert damping,  $H_{\text{eff}}$  the effective magnetic field and  $\gamma$  is the Gilbert gyromagnetic constant. It can be expressed as  $\gamma = \mu_0 \frac{g\mu_b}{\hbar} = -g \frac{e\mu_0}{2m_e}$ , where  $g$  is the Landé factor,  $\mu_0$  the vacuum permeability,  $m_e$  the electron mass and  $e$  the elementary charge.

The structure of the first term leads to precessional motion around the direction of the effective magnetic field  $\vec{H}_{\text{eff}}$ . The effective field is the negative derivative of the total energy density  $E$  with respect to the  $\vec{m}$  magnetisation:

$$\vec{H}_{\text{eff}} = -\frac{1}{\mu_0 M_s} \frac{\partial E}{\partial \vec{m}}. \quad (2.15)$$

The total energy includes contributions from ferromagnetic exchange energy, magnetocrystalline anisotropy energy, dipolar field energy and the Zeeman energy due to the external field.

To account for energy dissipation mechanisms, a second term (damping term), is introduced. It causes  $\vec{m}$  to finally relax into the direction of the effective field.

### 2.3.2 Extension including spin-transfer-torque (LLGS)

The general LLG equation including the two spin-transfer torque terms as it will be used in this thesis is given in eq. (2.16):

$$\begin{aligned} \frac{d\vec{m}}{dt} = & -\gamma(\vec{m} \times \vec{H}_{\text{eff}}) + \alpha \left( \vec{m} \times \frac{d\vec{m}}{dt} \right) \\ & - \gamma a'_{\parallel} V (\vec{m} \times (\vec{m} \times \vec{p})) + \gamma a'_{\perp} V^2 (\vec{m} \times \vec{p}). \end{aligned} \quad (2.16)$$

Here,  $\vec{m}$  and  $\vec{p}$  are the unit magnetisation vectors of the free and fixed layer, respectively.  $a'_{\parallel} = \frac{a_{\parallel}}{M_s V_{Mag}}$ ,  $a'_{\perp} = \frac{a_{\perp}}{M_s V_{Mag}}$ , where  $V_{Mag}$  is the volume of the free layer and  $V$  is the applied voltage. The prefactors  $a_{\parallel}$  and  $a_{\perp}$  determine the magnitude of the in-plane and perpendicular torques, respectively.

The bias-dependence of the two STTs is still under discussion. In this thesis, the in-plane STT is assumed to depend only linearly on the voltage and the perpendicular STT is assumed to depend only quadratically on the voltage. This is the only dependence for which both theoretical [1, 2] and experimental results [4, 5] are in agreement. An overview about the discussion of the bias-dependence of the STT in the literature is given in chapter 2.5.3. It should be noted that for the bias-dependence and the sign convention used in this thesis the in-plane torque can change its direction with the sign of the current: Positive (negative) current favours the P (AP) configuration. Due to the quadratic voltage dependence, the perpendicular STT favours the AP state for both current polarities.

The directions of the torques on the free layer magnetisation are schematically shown in figure 2.6 for the special case of the effective magnetic field being antiparallel to  $\vec{p}$ .

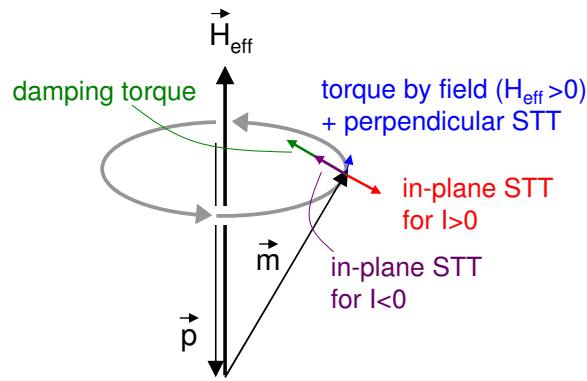


Figure 2.6: Schematic of the torques in the LLGS equation for the special case of  $\vec{H}_{\text{eff}}$  being antiparallel to  $\vec{p}$ . The torque on the magnetisation of the free layer  $\vec{m}$  experiences contributions from the effective magnetic field  $\vec{H}_{\text{eff}}$ , from the damping, from the in-plane STT and from the perpendicular STT. The sign conventions are chosen so that positive current and negative field favour the P state.

## 2.4 Applications of MR and spin-transfer torque

There are many applications of the magnetoresistance effect as field sensors, the most prominent example being the read head in hard disk drives. The introduction of GMR instead of AMR (anisotropic magnetoresistance) read heads has led to an immediate increase in the storage density. This was enabled by the fact that the GMR effect is an interface effect whereas the AMR effect is a volume effect and also by the higher

magnitude of the GMR signal. Any spin-transfer torque effects which are induced by the current through the read head needed for read-out are considered as problematic in these devices since they introduce noise and instability in the system.

Applications of spin-transfer torque are STT oscillators and magnetic random access memory (MRAM). In MRAM cells, the data is stored in magnetic states in devices with a large magnetoresistance, so that the read-out can be achieved by detecting the resistance. Since the first commercial STT-MRAM devices were introduced on the market quite recently, this chapter will concentrate on the two applications of read heads and STT-MRAM.

### 2.4.1 Read heads in hard disk drives

In a hard disk drive, the magnetised material with the stored information rotates below the read and write heads. The read head nowadays consists of two ferromagnetic layers (one of them free to move, the other fixed) with a non-magnetic spacer between. The free layer is used as a field sensor of the magnetic bit below and rotates its magnetisation accordingly. The state of the bit is then read-out by measuring the resistance over the whole stack using the MR effect.

The demand for increased memory densities requires higher track densities and therefore smaller read heads and a larger sensitivity of the read heads. The introduction of GMR-based read heads to replace AMR sensors in the year 1997 by IBM [34] triggered the first immediate increase of the storage density. The new concept of using MTJ-based read heads exploits the inherently high MR ratios arising from the TMR, leading to a higher sensitivity, an increased signal-to-noise ratio (SNR), smaller bit-error rates and allows to further decrease the sensor size.

In 2005, the first commercial TMR read head with an MTJ was introduced by Seagate [35]. It was demonstrated that the TMR read head can outmatch its conventional current in-plane (CIP)-GMR counterpart in terms of signal-to-noise ratio (SNR) and lifetime. The lifetime was found to increase compared to GMR read heads due to the lower power consumption and better thermal dissipation compared to at-that-time-conventional CIP-GMR read heads.

However, this might still be only a short-lived option: Due to the high intrinsic resistance (RA product above  $1 \Omega\mu\text{m}^2$ ), further downscaling leading to a higher resistance will make it difficult to keep a good SNR [34]. This might make spin-valves better candidates at such areal densities. The transition to perpendicular magnetic recording

for reasons of improved stability and increased potential areal density currently taking place will also lead to new demands concerning the writing process and the read/write head structure and design.

### 2.4.2 Spin-transfer torque magnetic random access memory

In contrast to conventional RAM (such as dynamic RAM (DRAM) or static RAM (SRAM)) where the information is stored as electric charge, magnetic random access memory (MRAM) makes use of two stable magnetisation directions of a magnetic layer. This hints to the first advantage of MRAM being non-volatile. Compared to other non-volatile techniques such as Flash memory, MRAM has an unlimited endurance [34]. Being capable of the speed of SRAM and the density of DRAM, the MRAM technique combines the advantages of several techniques and therefore has the potential to serve as a so-called 'universal' memory.

A typical MRAM cell consists of a CPP-MTJ, in which the binary information is stored as the direction of the free magnetic layer magnetisation. In the basic cross-point architecture, the memory elements are set at the cross-points of a rectangular matrix with vertical and horizontal conducting lines (word and bit line). The cells can then be addressed individually by activating both corresponding lines. A major challenge is to avoid thermally activated switching of other 'half-selected' cells in the same row or column. To remove unwanted current paths for reading the cell, usually a transistor is added in series with each MRAM cell (1T-1MTJ MRAM).

Whereas the reading-out always uses an MR effect (nowadays the TMR effect), there are many different writing mechanisms under development. In the conventional field-switched MRAM, the magnetic fields for writing are generated by sending a current through the corresponding word and bit lines. The current pulses are passed through the lines in such a way that their fields only switch the bit at the cross-point of the two lines, see figure 2.7(a). This requires quite a large current to generate the fields conflicting with the requirements of low power consumption. Furthermore, the long ranging magnetic field constrains the downscaling since it lowers the energy barrier for thermal reversal in adjacent memory cells. Approaches for field-switched MRAMs avoiding the problem of switching half-selected cells are the toggle MRAM (switching of a synthetic antiferromagnetic free layer by applying a specific current pulse sequence) and thermally assisted switching [36]. STT-MRAM cells can overcome these problems by applying the spin-transfer torque to directly write the cell by sending a

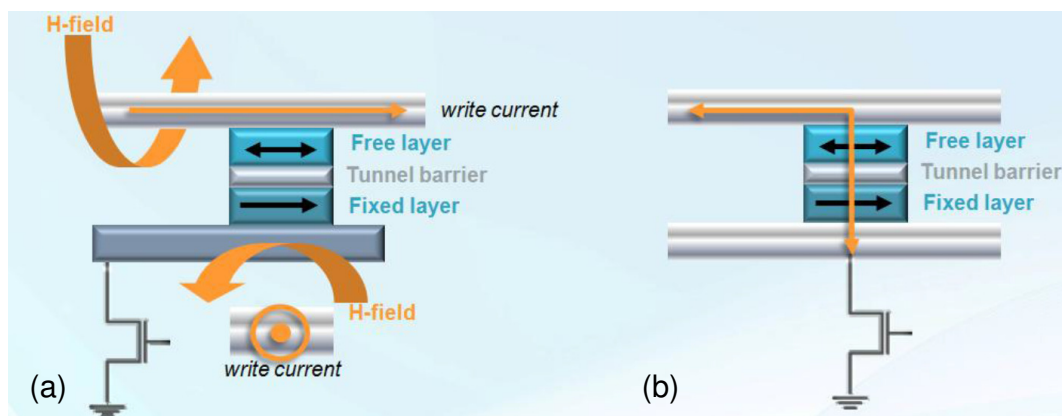


Figure 2.7: Schematic of the MRAM cell design for (a) field switched MRAM and (b) STT-MRAM using a current through the structure to switch the magnetic state of the element. Picture taken from Everspin Technologies [3].

current through the structure (see figure 2.7(b)). Since the amplitude of the torque per unit area is proportional to the injected current density, the writing current decreases proportionally to the cross section area of the cell and this mechanism is especially interesting for very small devices.

A major issue in STT-MRAM development is the reduction of the critical switching current since the size of the transistor supplying it shrinks with smaller current. A desirable critical density of  $1 \text{ MA/cm}^2$  would match the transistor size to the MTJ size [36]. Also, a low RA product is needed so that a sufficient current density can be reached without damaging the MTJ since the breakdown voltage is usually around 1 V. In order to be compatible to complementary metal-oxide semiconductor (CMOS) technology, impedance matching and low switching voltages are required. Problems such as heating, resistance drift and dielectric breakdown of the tunnel barrier have to be controlled [36]. The main development challenges are low write currents while maintaining a good bit stability and readability as well as a high read/write speed.

Many major semiconductor companies are involved in the MRAM development, e.g. IBM, SK Hynix or Samsung (which took over the STT-MRAM developer Grandis in summer 2011). In November 2012 Everspin was finally the first company to commercially produce an STT-MRAM announcing a 64-Megabit-MRAM. The estimated costs for 1 GB are still about 50 times higher than a conventional NAND-Flash memory [3]. Therefore a typical application is preventing critical data losses by replacing battery driven buffer memory, especially taking advantage of the robustness against high temperatures or ionizing radiation (e.g. in aerospace).



There are two main disadvantages of the in-plane magnetised MTJs compared to perpendicularly magnetised material stacks. Firstly, there is a strong dependence of the properties on the precise shape of the element. This leads to a broad distribution of switching fields for a memory cell array. Secondly, for in-plane MTJs, the (out-of-plane) shape anisotropy field increases the critical switching current, but does not contribute to the energy barrier for thermal reversal. This means that from the stability point of view an extra part of the switching current to overcome this field is 'wasted'. One approach to lower the switching current is therefore to provide a material with a perpendicular anisotropy strong enough to overcome the shape anisotropy. By using a perpendicularly magnetised MTJ design it is therefore possible to maintain the thermal stability while reducing the switching current [37]. Another advantage is the fact that the sizes of these elements can be reduced. However, the search and implementation of appropriate materials remain challenging.

Further technological methods to increase the overall MRAM areal density might be the 3D stacking of memory matrices, the multi-cell operation (overcoming the one-transistor per cell requirement) or the development of a three terminal device combining the MR and transistor effect. A way to increase the signal amplitude would be to replace the ferromagnetic layers with 100 % spin-polarised conductors such as Heusler alloys.

## 2.5 STT effects in magnetic tunnel junctions

### 2.5.1 Current-induced switching

In the case of current-induced switching, the spin-transfer torque generated by the passing spin polarised current can reverse the free layer magnetisation. This process can be described as a thermally activated process of crossing an energy barrier. Depending on the time range in which the current is applied, two regimes can be distinguished at a constant temperature: The thermally activated regime for longer pulse lengths ( $\gg 10$  ns) and the adiabatic precessional switching for very short pulses ( $\ll 10$  ns).

An experimental example for the two regimes from a CoFeB/MgO/CoFeB MTJ can be seen in figure 2.8. For long pulse lengths ( $>10$   $\mu$ s), the critical current decreases linearly with  $\ln\left(\frac{\tau}{\tau_0}\right)$ , which corresponds to the thermal activation model. The drastic increase of the switching current for pulse lengths shorter than 10 ns represents the precessional switching regime [38].

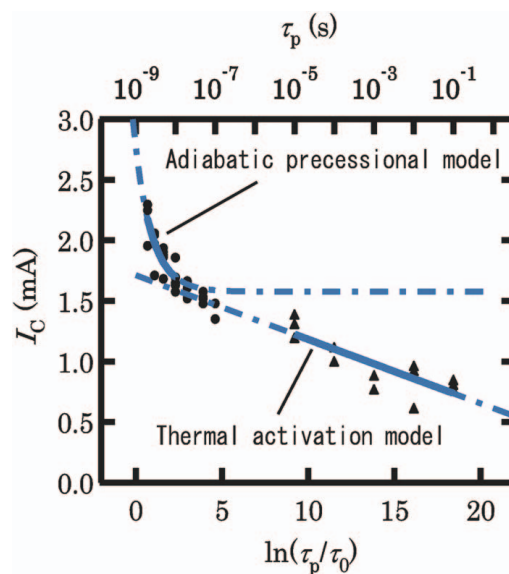


Figure 2.8: Switching current  $I_c$  depending on the pulse width. Marks show the experimental points corresponding to 2-100 ns (dots) and 10  $\mu$ s-100 ms (triangles). Solid lines are fitting curves, dashed lines the extrapolations for each fitting curve. Figure taken from [38].

In the following subsections, the current-induced switching and the two switching regimes are explained in more detail.

### 2.5.1.1 Current-induced switching and bias-dependence of TMR

An example for an R-V characteristic is given in figure 2.9. In this measurement, the resistance is measured while the voltage is looped through positive and negative voltages. Starting from the low resistance (P) state, as the voltage is increased to higher positive values, the increasing spin-transfer torque finally switches the magnetisation to the AP state, which is favoured by the applied voltage polarity. When the voltage is increased further, the magnetisation stays in this configuration. Switching back to the P state is observed after the voltage is reduced and reversed.

The TMR is found to be reduced for increasing applied voltage bias [40]. This effect is not fully understood and there are several mechanisms proposed to explain it, e.g. the fact that the electronic band structure of the magnetic electrodes changes with applied voltage bias [41] or an increased defect-state-assisted tunneling current through the tunneling barrier which leads to a decrease in the spin polarisation. However, this

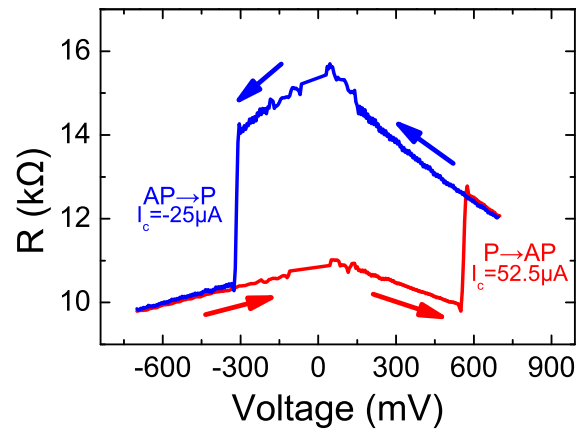


Figure 2.9: Resistance versus voltage loop for a perpendicular MTJ, taken from [39]. Positive voltage favours the AP state, whereas negative voltage favours the P state. An additional magnetic offset field was applied to center the hysteresis loop.

does not explain why the bias-dependence is usually much stronger in the AP state than in the P state, so additional studies are needed to understand the phenomenon.

It should be emphasised, that the switching characteristics for tunnel junctions ought to be analysed as functions of voltage and not current in contrast to metallic samples. This fact was not taken into consideration in the first years after 2000 and has still not become fully established in the literature. The reason is that the spin-transfer torque in MTJs is determined by the applied voltage regardless of the state of the sample (P or AP), in which case the tunnel currents would be significantly different due to the large change in resistance [40]. These differing resistances lead to the observation that the switching *currents* in experiments are typically much smaller when switching away from the AP state than from the P state [42, 43]. The switching *voltages* are typically much closer together. Small differences might be caused by heating effects or different non-uniform magnetic states for the two states [40].

In general, the switching voltages at room temperature are below the intrinsic critical voltages (defined for 0 K) due to thermal fluctuations of the magnetisation. The process of thermal activation will be investigated further in the next subsection.

### 2.5.1.2 Thermal activation model

The reversal process of a nanomagnet at room temperature can be described as a thermally activated process of crossing an energy barrier  $E_{barrier}$ . This thermally activated

scenario is the dominant switching process at longer pulse lengths since longer pulses allow for more switching attempts [38, 44].

In the case of STT-induced switching, when additional thermal activation is provided at elevated temperatures, the dissipation can be overcome at lower currents or voltages compared to the case of lower temperatures. This explains why switching is experimentally observed already at currents or voltages below the critical values. The effect of the random thermal activation leads to a statistical distribution of the switching time after the pulse onset despite an identical measurement condition.

The relaxation (or dwell) time  $\tau$  in one state for a single domain particle with uniaxial anisotropy is expressed by the Néel-Brown (or Arrhenius) formula:

$$\tau = \tau_0 \exp\left(\frac{E_{\text{barrier}}}{k_B T}\right), \quad (2.17)$$

where  $1/\tau_0$  is the attempt-frequency (usually  $\tau_0 \approx 1$  ns [45]),  $k_B$  is Boltzmann's constant and  $T$  is the temperature [46, 47].

The energy barrier height depends on the externally applied magnetic field. If the field's direction is such that it lowers the energy barrier, its magnitude can be increased until switching occurs in the time scale of interest. The energy barrier also depends on the magnetic volume,  $V_{\text{Mag}}$ , and on the anisotropy  $K$ :

$$E_{\text{barrier}} = KV_{\text{Mag}} \left(1 \mp \frac{H_{\text{eff}}}{H_k}\right)^n. \quad (2.18)$$

The effective field  $H_{\text{eff}} = H_{\text{ext}} + H_k + H_{\text{demag}}$ , i.e. it includes the external field, the anisotropy and demagnetising field. For symmetric energy barriers, the exponent is  $n = 2$  [47].  $\Delta = \frac{KV_{\text{Mag}}}{k_B T}$  is referred to as the thermal stability factor.

An important assumption underlying the Néel-Brown formula is that the torque acting on the magnetisation arises from an effective field  $-\nabla_m E(m)$ , where  $E(m)$  is the total magnetic energy [48]. Taking into account STT, there exists no such energy function anymore. This problem of a thermally assisted activation process driven by a nongradient force is still a pending issue in statistical physics.

Li and Zhang [48] have investigated to what extent the thermal activation can still be formulated in the form of a Néel-Brown activation process. For this they proposed the stochastic Landau-Lifshitz equation (including temperature as a fluctuating magnetic field with a Gaussian distribution) and a corresponding Fokker-Planck equation in the presence of a current-induced in-plane STT. It is assumed that the STT does not contain

an additional fluctuating field. A stationary solution for the probability density of the magnetisation was found, in the limit of the energy barrier being much larger than the thermal energy  $k_B T$ .

It is found that the solution can be expressed as a modified Néel-Brown formula in which the STT alters the magnetic energy. Therefore, there is an effective energy barrier associated with the STT [48]:

$$\tau = \tau_0 \exp \left( \Delta \left( 1 \mp \frac{H_{eff}}{H_k} \right)^2 \left( 1 \mp \frac{a}{a_c} \right) \right). \quad (2.19)$$

Here,  $a$  is the STT and  $a_c = \alpha(H_{ext} + H_k + H_{demag})$  the critical STT. Often, the last factor is approximated by the critical voltages:  $1 \mp \frac{V}{V_c}$  [49].

Li et al. [49] have included the perpendicular spin-transfer torque in a similar way as an additional change in the effective magnetic field  $H_{STT\perp}(V)$ :

$$\tau = \tau_0 \exp \left( \Delta \left( 1 \mp \frac{H_{eff} + H_{STT\perp}(V)}{H_k} \right)^2 \left( 1 \mp \frac{V}{V_c} \right) \right). \quad (2.20)$$

In general the change of the effective field due to the perpendicular torque does also effect the last factor, but this causes a rather complex dependence on the voltage and was neglected in [49].

To apply eq. (2.20) in experiments, the bias-dependence of the spin-transfer torque needs to be known. The latter is still largely discussed. Li et al. [49] determined the bias-dependence of the perpendicular spin-transfer torque by using eq. (2.20) (see chapter 2.5.3).

### 2.5.1.3 Adiabatic precessional model

In the adiabatic precessional model, magnetisation switching occurs due to STT-induced amplification of the precessional angle. The applied current is high enough so that the STT can overcome the damping torque. If the speed of the switching is fast enough, the effect of thermal activation on the switching is negligible.

For small pulse widths, the switching time  $\tau$  in an adiabatic precessional model is given by [38, 50, 51]:

$$\tau(\theta_0) = \frac{2}{\alpha\gamma\mu_0 M_S} \frac{I_c}{(I - I_c)} \ln \left( \frac{\pi/2}{\theta_0} \right), \quad (2.21)$$

where  $I_c$  is the intrinsic switching current and  $\theta_0$  the initial angle between the magnetisation and its easy axis [51]. The angular expression means that the STT amplifies the precession angle starting at the initial angle  $\theta_0$  until it reaches  $\frac{\pi}{2}$ , such that the hard axis is overcome, leading to switching. The logarithm describes the exponential amplification of the precession angle at a rate given by the balance between dissipation ( $\alpha\gamma\mu_0 M_S$ ) and the energy supply rate provided by the STT (expressed as an overdrive  $\frac{I-I_c}{I_c}$ ).

From this formula, it can be seen that the speed of the switching ( $\tau^{-1}$ ) is increasing for a higher damping factor  $\alpha$ , for increased applied currents (or voltages) or for large starting angles  $\theta_0$  (close to  $\pi/2$ ). Devolder et al. followed the latter approach by applying an additional hard axis external magnetic field [51] leading to significant reductions of the switching current amplitude. In real applications, this could be implemented by an exchange bias field along the magnetic hard axis of the samples.

The applicability of the two models for different pulse widths was tested by Aoki et al. [52]. The switching probability was measured as a function of the pulse width without any net magnetic fields (external magnetic fields were applied in both the easy and hard axis to cancel out the shift of the hysteresis curve). With increasing pulse length (0.4 ns, 5 ns and 10 ns), the data could not be fitted anymore with the adiabatic precessional model, but the thermal activation model fit well. For the case of the shortest pulse length (0.4 ns), it was found that the switching probability exhibits a step-like behaviour with constant plateaus of a period of 100-200 ps between the steps. These could be ascribed to discrete oscillation cycles of the precessing magnetisation of a reasonable frequency of 2.5-5 GHz prior to switching. This supports the idea that randomisation due to temperature during the switching is negligible. However, temperature does play a role for setting the initial starting angle.

There are different ways to determine the intrinsic zero-temperature threshold current: A commonly used technique is to measure the statistics of switching depending on the pulse lengths and extrapolating to the ns-scale (or directly measuring at a pulse length of 1 ns). Another method estimates  $I_c$  from the probabilistic distribution of the current for a certain pulse length, using the fact that this distribution is also caused by thermal fluctuations. Morota et al. [53] have compared the extrapolation method at different pulse length with the latter method and they found a good agreement for the critical switching current. Another way is to measure the critical current density at different temperatures and then extrapolate to 0 K [25].

#### 2.5.1.4 Real-time observation of current-induced switching

Studying the current-induced switching in the time-domain makes it possible to characterise the full time-dependent magnetic response to a current pulse. This is also important from an application point of view since the operating speed for STT devices can be determined.

The first observation of the magnetisation reversal in the time-domain was performed on asymmetric spin-valves by Krivorotov et al. in 2005 [54]. At that time the signal-to-noise considerations required averaging over multiple signal traces for time-resolved measurements. For the observed oscillatory signals, the phase of the oscillations had to be the same in each trace so that the signal was not lost during the averaging process. For this, the sample was designed in such a way that the initial starting angle between the free and fixed layer was well controlled: The fixed layer was exchange biased at an angle to the free layer (about  $30^\circ$ ) and furthermore, the experiment was performed at a temperature of 40 K. The results supported the STT driven reversal as switching process. The traces show coherent oscillations before the switching and the switching itself looks like a gradual change in the magnetoresistance. However, the authors point out that this gradual change is a measurement artefact due to the averaging of multiple switching events with a sharp transition but a distribution of the initial magnetisation direction angles. This was also confirmed by micromagnetic simulations [54].

This illustrates the limits of the averaging technique for time-resolved studies: It is possible to determine the mean speed and reproducible parts of the magnetisation dynamics, but individual variations in the switching trace are lost. Since the switching process is not deterministic at room temperature, it is essential to examine single events in order to make a precise investigation. Real-time single-shot observations have become possible after the introduction of MTJs with a larger output signal after the year 2008 [55, 56, 57, 58].

For the case of the applied current being larger than the zero-temperature threshold current, most of the switching events were rapidly accomplished after 500 ps [55], probably due to a coherent magnetisation reversal.

In the case where the applied current was smaller than the zero-temperature threshold current for switching, the reversal consisted of an **incubation delay** ('non-reactive time') followed by a **short transition time** ( $< 400$  ps) [55, 56]. The delay was found to fluctuate significantly. This effect might be due to a transition of the system from

the thermally equilibrated initial state to a meta-stable state under a finite current [55]. This was already predicted in a simulation by Lee et al. [59]. Even at 0 K, the so-called ‘stage 1’ corresponds to a transition of the magnetisation from its equilibrium to the excited state.

A study of the time-range **after the switching event** revealed that the resistance traces were reproducible [56]. When 20 traces were averaged with the switching edges aligned, the switching was found to be terminated by a large ringing that was damped progressively. The frequency and decay rate of the ringing indicated a high spatial coherence after switching.

Investigating the time **before** the abrupt switching event, Devolder et al. reported a non-oscillating behaviour with a rather slow regular increase in the magnetoresistance, in which probably only the tips or corners of the magnetisation of the free layer started bending [56]. Cui et al. [58] increased the SNR of their setup by using a pulse subtraction method and studied switching events for both no magnetic field and a 100 Oe hard-axis field. For the analysis, 2000 traces were averaged with their switching edges aligned. The hard-axis field caused oscillations with increasing amplitude before switching, showing that the switching occurred preferentially at a particular phase of the oscillations. Without magnetic field, the oscillatory features vanished almost entirely. The results could be reproduced by a micromagnetic simulation. For the hard-axis field, the switching dynamics were found to be generally more spatially uniform.

Aoki et al. [57] reported an observation of a **dynamic magnetic intermediate state** during the switching process as slow resistance oscillation. This intermediate state was very sensitive to current amplitude and explained with inhomogeneous magnetisation behaviour such as multi-domain or vortex creation.

A **quasiballistic switching** by a single precessional turn of the magnetisation using a hard axis bias field was reported by Serrano-Guisan [60]. This could be exploited in ultrafast, highly reliable STT devices in the future.

### 2.5.1.5 Phase diagrams

Phase diagrams show the stable states of a magnetic structure depending on the externally applied magnetic field and current (or voltage). They provide a summary of the possible static and dynamic states and the switching characteristics at a glance.

An example of an analytically and numerically calculated phase diagram for an **in-plane magnetised metallic spin-valve** in the macrospin approximation is given in



figure 2.10. If the applied field  $H_x$  is smaller than the anisotropy  $H_k$ , both P and AP

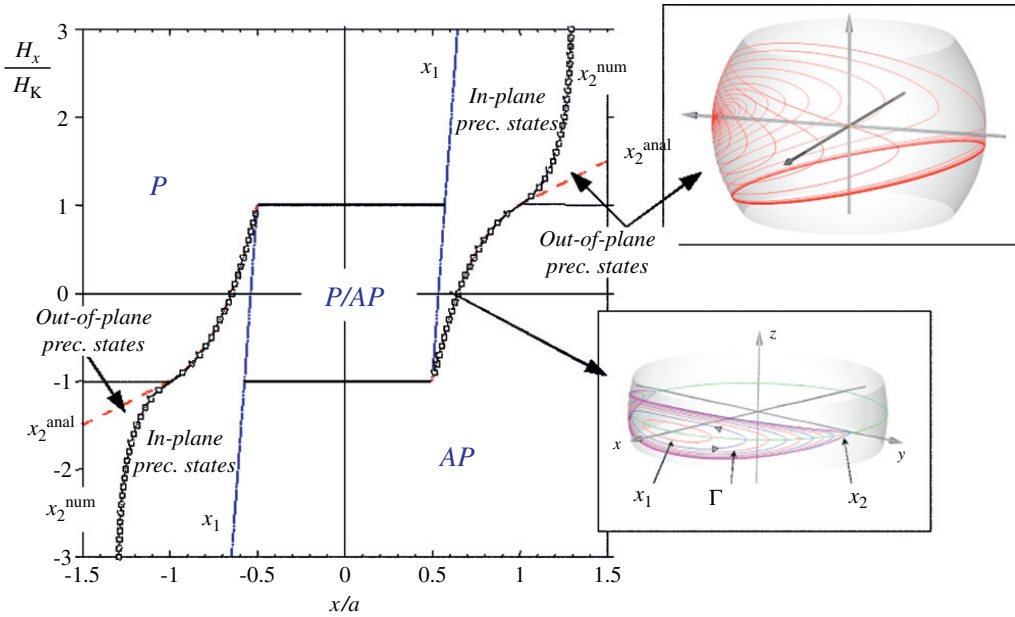


Figure 2.10: Simulated phase diagram by Berkov et al. [61] for a metallic spin-valve at 0 K in the macrospin approximation as functions of reduced coordinates (current  $x/a$  and field  $H_x/H_k$ ). Positive magnetic field and negative current favour the P state. Blue and red lines are calculated analytically whereas the open symbols are obtained from a numerical simulation.

state are stable. In this region, current-induced switching at a constant field is possible. For the current convention used in [61], this corresponds to a horizontal scan in the diagram and switching from P to AP occurs for positive currents, from AP to P for negative currents. However, there are intermediate precessional regions between the two states with an in-plane, clamshell-like orbit and out-of-plane orbits for magnetic fields above the anisotropy  $H_k$  (see figure 2.10). Finally, at high fields and currents favouring opposite states, the P or AP states are no longer stable and only out-of-plane precessional states should be observed.

A corresponding experimental phase diagram was obtained by Kiselev et al. in 2003 [28] and can be seen in figure 2.11. The sample was a metallic nanopillar with a stack composition of 40 nm Co/10 nm Cu/3 nm Co with an extended reference layer and an elliptical cross-section of 130 nm  $\times$  70 nm. Both differential resistance and microwave spectra were measured for different combinations of field and current. The results are in good agreement with the theoretical diagram: For applied magnetic fields smaller than the coercivity ( $\approx 600$  Oe), current induced switching is observed. Hys-

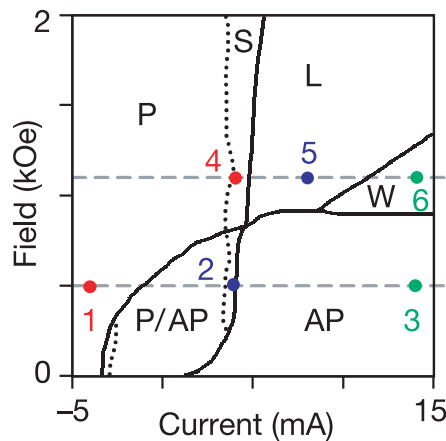


Figure 2.11: Experimental phase diagram measured at room temperature by Kiselev et al. [28]. S corresponds to a the small-amplitude precessional regime, L to the large-amplitude dynamical regime, and W is a state with a resistance between P and AP and only small microwave signals.

teretic magnetic field switching is also possible (here a vertical scan in the phase diagram). For fields larger than the coercivity, the applied currents lead to peaks in the differential resistance corresponding to dynamical regimes which can be distinguished by the microwave power output. When changing from the small-amplitude to the large-amplitude regime, the microwave power grows by two orders of magnitude and the peak frequencies shift abruptly. In the large-amplitude regime, the peaks shift down in frequency with increasing current. The comparison with the theoretical phase diagram suggests that the large-amplitude microwave signals correspond to large-angle, approximately in-plane precession of the free layer magnetisation. The region 'W' in the experiment with an experimental resistance between P and AP and only small microwave signals could not be reproduced by the macrospin simulation. Soon after, Lee et al. [59] identified the region 'W' with micromagnetic simulations: It corresponds to a formation and annihilation of dynamic vortices through the interplay of the large current-induced Oersted fields and the STT.

The appearance of the region 'W' shows that a simple macrospin approximation can not account for all features of the dynamical behaviour of real samples. The effect of temperature also leads to differences between the (zero temperature) calculation and the room temperature experiment:

- A rounding off of the sharp transitions in the phase diagram is obtained.
- Microwave signals can not only be observed at large fields above the coercivity,

but also at lower field-regions. This might be due to small fluctuations of the free layer magnetisation away from the easy axis that would lead to a measurable precession but not to switching.

Two examples for experimental phase diagrams of **asymmetric in-plane MTJs** were published by Park et al. [11] and Oh et al. [10]. Figure 2.12 displays the phase diagrams measured at 300 K and 4.2 K by Oh et al. [10]. The authors ascribe the

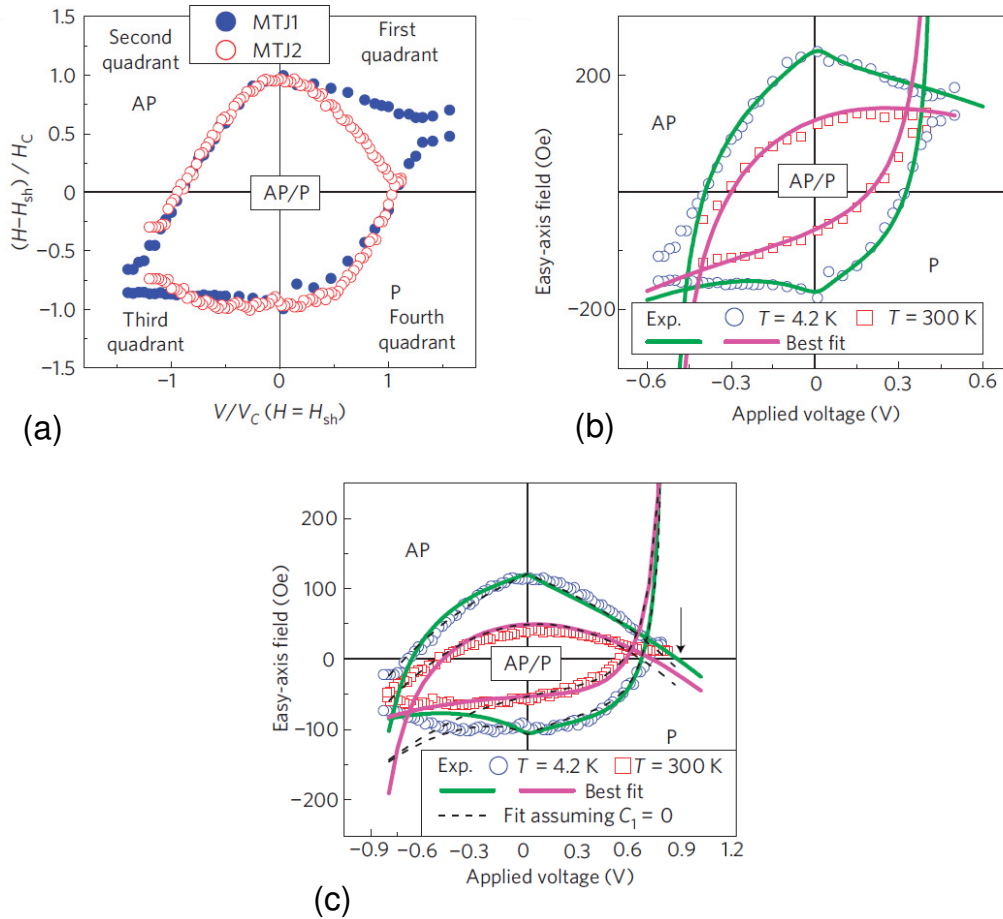


Figure 2.12: Switching phase diagrams of asymmetric MgO-based MTJs at room temperature and 4.2 K, taken from [10]. (a) shows normalised phase diagrams of MTJ1 and MTJ2 at 4.2 K, (b) and (c) depict phase diagrams at 300 K and 4.2 K of MTJ1 and MTJ2, respectively, as well as the fits to the critical switching voltages. Both MTJs are asymmetric with a free layer composition of 1.8 nm of  $\text{Co}_{20}\text{Fe}_{60}\text{B}_{20}$  (MTJ1) and 2.3 nm of  $\text{Co}_{49}\text{Fe}_{21}\text{B}_{30}$  (MTJ2).

differences in the first and third quadrant of the phase diagrams for the two samples to the different composition of the free layer of the MTJs, leading to a different bias-dependence of the perpendicular STT [10].

For the case of fully **perpendicularly magnetised metallic spin-valves**, the theoretical phase diagram looks much simpler, as was derived by Le Gall et al. [62]. It is plotted in figure 2.13 (a). Due to the absence of any in-plane anisotropy components,

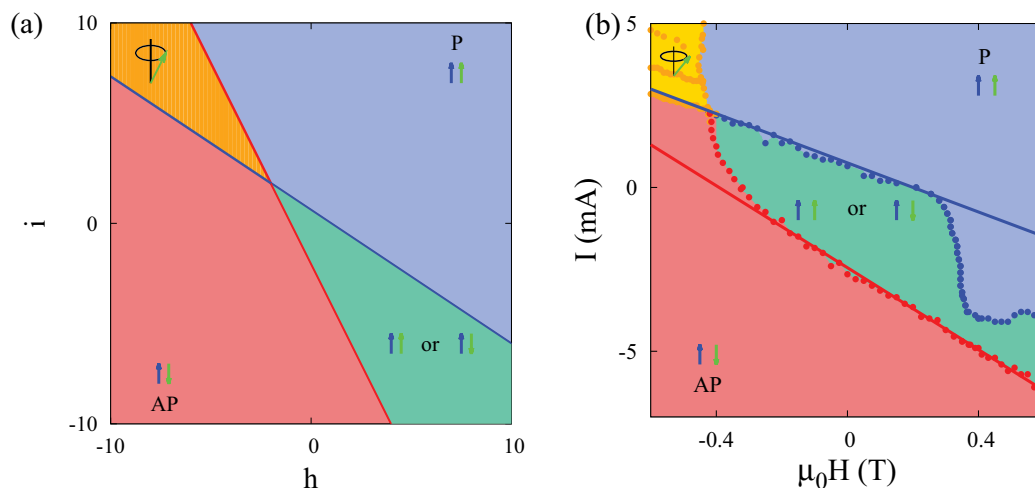


Figure 2.13: Phase diagrams of a metallic nanopillar with perpendicular magnetisation, taken from [62]. Positive field and current favour the P state. (a) Theoretical phase diagram in the macrospin approximation with reduced coordinates (see [62] for exact definitions) and (b) experimental phase diagram, dots are the measured switching fields, orange triangles indicate the presence of a peak in the differential resistance. The blue and green small arrows indicate the reference and free layer magnetisation direction, respectively. The red coloured area corresponds to the AP state being stable, the blue area to P, green to a bistable state and orange to a precessional region.

the diagram only consists of two critical lines. Since for metallic structures the STT asymmetry parameter is different from 1 in most cases, the slope of the lines is different. Therefore they cross and divide the field-current-space into four different regions: two regions where only P or AP are stable, a bistable region and a region without any stable static states. In this last region, a steady magnetisation precession around the perpendicular axis is expected.

Figure 2.13 (b) shows an experimentally obtained phase diagram from [62] for the case of a perpendicular magnetisation direction. The sample used in the experiment was a hexagonal nanopillar of lithographical dimensions of 100 nm by 200 nm. The magnetic layer structure consists of a Pt(3 nm)/[Co(0.25 nm)/Pt(0.52 nm)]<sub>5</sub>/Co(0.2 nm)/[Ni(0.6 nm)/Co(0.1 nm)]<sub>2</sub>/Co(0.1 nm) reference layer and a Co(0.1 nm)/[Co(0.1 nm)/Ni(0.6 nm)]<sub>4</sub>/Pt(3 nm) free layer separated by a 4 nm Cu spacer layer. As in the theoretical diagram, there are the two critical lines dividing the diagram into the same four

regions. In the region with large positive currents and large negative fields (upper left corner), the differential resistance shows peaks. It is not as easy to detect if these peaks are related to magnetisation precession as in the in-plane case: A uniform precession of the free layer magnetisation around the perpendicular axis does not affect the angle between the magnetisations of the free and the reference layer which is used as read-out mechanism via the GMR effect.

The large difference to the theoretical phase diagram is the strong deviation from linearity around the zero current switching field. The magnetisation reversal becomes almost independent of the current and the current has to increase to a certain threshold until the linear behaviour appears. The reasons for this were experimentally investigated by varying temperature, measurement speed, nanopillar size and magnetic field angle. It was shown that the angle of the applied field and therefore a break of the uniaxial symmetry has a huge effect on the slope of the critical lines.

Finally, theoretical phase diagrams for perpendicular metallic structures with symmetry breaking of the anisotropy were derived, which can account for magnetocrystalline anisotropy or distributions of the anisotropy direction due to a granular structure of the material [62].

### 2.5.2 Magnetisation precession

Spin-transfer torque can also be used to exert a stable precession of the magnetisation if it opposes the damping. The precessional motion and the quick change in the magnetisation transforms to a rapid change in resistance and therefore to a fast varying voltage across the device. The precession frequency of the oscillator is adjustable by the current. Such a tunable conversion from DC current to AC voltage has been proposed as current-controlled microwave source and resonator, e.g. for telecommunication systems.

The first observation of STT induced precession in CPP spin-valve devices was reported by Kiselev et al. in 2003 [28]. The applied current was favouring the opposite state compared to the external magnetic field, so that switching was prevented, but the free layer was driven into a cyclic trajectory with a frequency in the GHz range. An increase in current will change the orbital form from small angle to large angle in-plane oscillation. At even higher currents, the trajectory changes to an out-of-plane orbit. An in-plane trajectory was accompanied by a redshift of the signal with increasing current, whereas the out-of-plane oscillation frequency was blue-shifting. However,

the output power from such CPP spin-valve devices in the order of pW is much too low for practical applications, which require an output power in the range of  $\mu\text{W}$  [63].

MgO-based MTJs with larger MR ratios are potentially able to achieve a higher output power. An output in the  $\mu\text{W}$  range was achieved with a CoFeB/MgO/CoFeB MTJ with a TMR ratio of 110 % in 2008 [64]. It showed a rather large linewidth ( $\approx 100$  MHz), but in general the two requirements of large output power and low linewidth are difficult to achieve simultaneously.

One way to reduce the linewidth and increase the output power would be the phase-locking of several oscillators. Due to the coherence of the individual oscillators, their combined power in the phase-locked state is expected to scale with the square of the number of the locked oscillators. This was demonstrated experimentally with two GMR-devices by Kaka et al. [63]. However, it is technologically challenging to phase-lock more than two devices.

### 2.5.3 Bias-dependence of STT

In order to control the influence of spin-transfer torque on the magnetisation, its magnitude and bias voltage dependence are of great interest. Note that the derivative of the torque with respect to the voltage has been given the name 'torkance' [40]. There are several different approaches to measure the torkances in MgO-based MTJs experimentally.

For low-to-moderate voltages, spin-transfer driven ferromagnetic resonance (ST-FMR) [4, 5, 65, 66, 67, 68] and thermally excited ferromagnetic resonance (TE-FMR) [64, 69, 70, 71, 72] can be used. The latter technique will be introduced in more details in section 3.3.3.

Another method is the analysis of statistics of thermally excited switching; this is done at large bias voltages [49] or moderate bias by fitting plots of the switching fields as function of the applied bias voltage [10]. This method needs to assume a particular functional form for the bias-dependence on the torque and is sensitive to assumptions made on the heating [73]. Wang et al. have measured the resonant magnetic precession due to an oscillating STT in the time-domain [73] whereas Xue et al. determined the oscillating resistance due to an oscillating STT with a network analyser [74].

The bias voltage dependence as well as the actual values of the two components are currently widely discussed in the literature. An overview about this discussion will be given in the next two subsections. The two STT components are predicted by theory

to depend on the symmetry of the structure as well as on the layer thicknesses, the magnitude of the exchange splitting and on the interfacial microstructure [6, 7].

### 2.5.3.1 Bias-dependence of the in-plane spin-transfer torque

Kubota et al. [5] and Sankey et al. [4] report a linear dependence of the in-plane STT for MgO-based MTJs. This is in good agreement with first-principle calculations by Heiliger and Stiles [75]. It has to be noted, that there was a deviation from the linear behaviour observed for large voltage bias (above 300 mV) for samples of comparable composition if ST-FMR [4, 5] or TE-FMR [64] were used. Other groups also found a linear behaviour with deviation already at  $V > 200$  mV [73] or  $V > 100$  mV [74], but the sample compositions were different to the ones mentioned before (see table 2.1).

Jung et al. [71] also report a linear dependence of the in-plane STT, but with a factor of 2 difference between the P and AP state although it should be independent of the state.

Table 2.1 summarises the values obtained for the in-plane STT parameter in different units. The often experimentally determined unit of mT/V can be converted to an energy (J/V) if both the saturation magnetisation and the volume are known. The unit of  $1/(\Omega\text{m}^2)$  is obtained from J/V by dividing by the cross sectional area of the device and multiplying with the constants  $\gamma \frac{e}{\mu_B}$ .

### 2.5.3.2 Bias-dependence of the perpendicular spin-transfer torque

For **symmetric** junctions, the perpendicular STT vanishes at zero voltage [6, 5]. An experimental non-zero perpendicular torque at zero bias voltage would therefore provide information on asymmetries in the MTJ.

For non-zero bias voltage, in most of the experiments the perpendicular spin-transfer torque is found to be quadratic in the applied voltage [5, 64, 67, 68], which is in good agreement with first-principle calculations by Heiliger and Stiles [75]. The perpendicular STT parameter reached up to 25-30 % of the in-plane torque for an applied bias of max. 300 to 500 mV [4, 64].

However, Petit et al. [69] measured the change of the resonance frequency peak in circular  $\text{Al}_2\text{O}_3$ -MTJs as a function of bias current and found that the perpendicular torque was proportional to the bias current and therefore changes sign with bias voltage. This is in qualitative agreement with another measurement on MgO-MTJs by Li et al. [49], who have accounted for heating effects due to large current densities required

for switching. However, this measurement was also done as a function of current (not voltage) and at a higher bias regime than Sankey et al. [4], Deac et al. [64] or Kubota et al. [5].

If the MTJs are **asymmetric**, i.e. the free and reference layer are not identical, an additional linear dependence of the perpendicular STT on the bias voltage was found [10]. This is also in agreement with theoretical predictions [6]. An experimental affirmation of this are the TE-FMR measurements on asymmetric MgO-MTJs by Petit et al. [70]. For the perpendicular STT, a quadratic dependence on the voltage was found with an additional linear term either from unbalanced Oerstedt fields or the sample asymmetry. Another TE-FMR measurement of Heinonen et al. [72] on slightly asymmetric CoFeB-based MgO-MTJs with different thickness showed a solely linear dependence of the perpendicular torque and the same order of magnitude as the in-plane STT. Oh et al. [10] determined the bias-dependence for the STT from switching phase diagrams (at 4.2 K and 300 K) for asymmetric MTJs. They also concluded that the perpendicular STT includes a linear and a quadratic bias-dependence term.

Table 2.2 summarises some literature values obtained for the quadratic part of the perpendicular STT parameter in different units.



1st author	$a_{  } [10^{10} \frac{1}{\Omega m^2}]$	$a_{  } [10^{-20} \frac{J}{V}]$	$a'_{  } [\frac{mT}{V}]$	free layer/tunnel barrier [nm]	voltage dependence for $a_{  }$	ref.
Heiliger	<b>3.5</b>			Fe/MgO	linear	[75]
Wang <sup>1</sup>	$3.25 \pm 0.65$	$3.29 \pm 0.66$	$3.1 \pm 0.6$	Co <sub>60</sub> Fe <sub>20</sub> B <sub>20</sub> (2.5)/MgO (1.25)	linear (V<0.3 V)	[67]
Sankey	$3.37 \pm 0.52$	$4.27 \pm 0.66$	$4.0 \pm 0.6$	Co <sub>60</sub> Fe <sub>20</sub> B <sub>20</sub> (2.5)/MgO (1.25)	linear (V<0.3 V)	[4]
Kubota	7.82	<b>45.5</b>		Co <sub>60</sub> Fe <sub>20</sub> B <sub>20</sub> (2)/MgO (1)	linear (V<0.3 V)	[5]
Deac	0.96	<b>2.78</b>	<b>2.4</b>	Co <sub>60</sub> Fe <sub>20</sub> B <sub>20</sub> (1.5)/MgO (0.6)	linear (V<0.3 V)	[64]
Wang <sup>2</sup>	6.92	$0.145 \pm 0.033$		CoFe (0.5)+ CoFeB (3.4)/MgO	linear (V<0.2 V)	[73]
Xue	19.7	0.411		CoFe (0.5)+ CoFeB (3.4)/MgO	linear (V<0.1 V)	[74]
Petit	21.3	0.05	<b>14</b>	Co <sub>90</sub> Fe <sub>10</sub> (1)+ Ni <sub>80</sub> Fe <sub>20</sub> (5)/MgO (0.7)	linear (V up to 0.3 V applied)	[70]
Skowronski <sup>3</sup>	5.2	<b>0.5</b>		Co <sub>40</sub> Fe <sub>40</sub> B <sub>20</sub> (2.3)/MgO (0.7-1.1)	linear (V up to 0.4 V applied)	[68]
Jung	78.8 – 145	0.4 – 0.75	<b>6-12</b>	Co <sub>60</sub> Fe <sub>20</sub> B <sub>20</sub> (3)/MgO (0.85)	linear, but factor of 2 difference P/AP	[71]

Table 2.1: Overview of literature values for the in-plane STT in different units. The bold values were taken directly from the references.

<sup>1</sup>The values discussed here are from sample 1 in ref. [67]. <sup>2</sup>Please note that the data from Wang et al. is at high bias voltage (0.38 V).

<sup>3</sup>The data from Skowronski et al. is from the sample with 0.95 nm thick MgO tunnel barrier.

1 <sup>st</sup> author	$a_{\perp}$ [ $10^{10} \frac{1}{\Omega \text{m}^2 \text{V}}$ ]	$a_{\perp}$ [ $10^{-20} \frac{\text{J}}{\text{V}^2}$ ]	$a'_{\perp}$ [ $\frac{\text{mT}}{\text{V}^2}$ ]	free layer/tunnel barrier [nm]	voltage dependence for $a_{\perp}$	ref.
Heiliger	<b>6-9</b>			Fe/MgO	quadratic	[75]
Wang <sup>1</sup>	5.19	5.26	4.96	Co <sub>60</sub> Fe <sub>20</sub> B <sub>20</sub> (2.5)/MgO (1.25)	quadratic	[67]
Sankey	2.18 ± 0.34	2.76 ± 0.43	2.6 ± 0.4	Co <sub>60</sub> Fe <sub>20</sub> B <sub>20</sub> (2.5)/MgO (1.25)	quadratic	[4]
Kubota	2.97	<b>17.3</b>		Co <sub>60</sub> Fe <sub>20</sub> B <sub>20</sub> (2)/MgO (1)	quadratic	[5]
Deac	7.22	<b>20.9</b>	18	Co <sub>60</sub> Fe <sub>20</sub> B <sub>20</sub> (1.5)/MgO (0.6)	quadratic	[64]
Wang <sup>2</sup>	7.39	15.5 ± 0.9		CoFe (0.5)+ CoFeB (3.4)/MgO	quadratic (V<0.3 V), then linear	[73]
Xue	12.3	25.7		CoFe (0.5)+ CoFeB (3.4)/MgO	quadratic	[74]
Petit	33.5	780	<b>22</b>	Co <sub>90</sub> Fe <sub>10</sub> (1)+ Ni <sub>80</sub> Fe <sub>20</sub> (5)/MgO (0.7)	linear + quadratic	[70]
Skowronski	2.1	20		Co <sub>40</sub> Fe <sub>40</sub> B <sub>20</sub> (2.3)/MgO (0.7-1.1)	quadratic	[68]
Jung	8.71 – 10.6	45 ± 55	<b>7.4-9.0</b>	Co <sub>60</sub> Fe <sub>20</sub> B <sub>20</sub> (3)/MgO (0.85)	quadratic	[71]
Li	1.30 – 2.19	5.44 ± 9.15	<b>3.4-5.8</b>	CoFeB (2.2)/MgO(1)	linear with $ I V$ , changes sign with current	[49]
Oh			<b>7-13</b>	MT11: Co <sub>20</sub> Fe <sub>60</sub> B <sub>20</sub> (1.8)/MgO (0.7), MT12: Co <sub>40</sub> Fe <sub>21</sub> B <sub>30</sub> (2.3)/MgO (0.7)	linear+quadratic	[10]

Table 2.2: Overview of literature values for the perpendicular STT. The bold values were taken from the references. <sup>1</sup> The values discussed here are from sample 1 in ref. [67]. <sup>2</sup>Please note that the data from Wang et al. is at high bias voltage (0.38 V).

### 2.5.4 Back-hopping

For the potential application as MRAM cell, in order to switch the magnetisation direction typically a larger voltage bias than the critical voltage ( $V_c$ ) is applied to compensate sample to sample variations. It has been reported, however, that this can induce a telegraph-noise like behaviour [8, 9], typically referred to as ‘back-hopping’ [8, 9, 76] or ‘abnormal switching-back phenomenon’ [10, 77]. This means that the magnetisation of the free layer switches back to its original state after a successful write operation although the applied voltage is exceeding the critical voltage for switching. It is not observed in metallic structures, but characteristic for MTJs and very inconvenient for the design of industrially-competitive MRAM devices [76].

An experimental example for the back-hopping is shown in figure 2.14, taken from [10]. Back-hopping occurs when the voltage is increased above the switching voltage

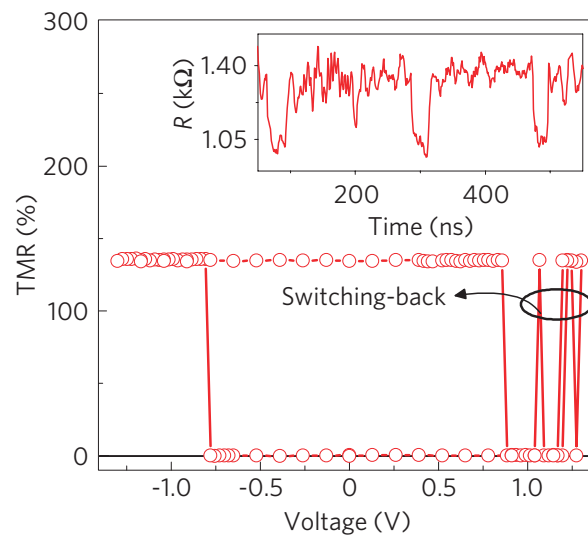


Figure 2.14: Example of an R-V curve of an MTJ exhibiting back-hopping (or ‘switching-back’) at voltages above 1 V, taken from [10]. The data were obtained in an off-pulse measurement (pulse width = 50 ns). The inset shows a time trace of the random telegraphic noise measured at 1 V.

(around 0.8 V): The resistance alternates between the P and AP state.

Back-hopping has been observed both in off-pulse measurements [9, 11, 77] as well as in on-pulse measurements [8, 77]. It has been seen in symmetric MTJs [8, 9] as well as in asymmetric MTJs with Co-rich FeCoB free layer [10, 11], whereas in the latter case the back-hopping could be suppressed by changing the composition of the free layer to an Fe-rich CoFeB. The back-hopping is typically one-sided for one

constant applied field, i.e. it only appears or is more pronounced either in the switching direction from antiparallel (AP) to parallel (P) (electrons flow from the reference to the free layer) [8, 10, 11, 77] or in the P to AP switching direction (electrons flow from free layer to reference layer) [9]. However, back-hopping does not appear in fully perpendicular MTJs [78].

The different groups reporting on the back-hopping observation interpret their results based on a variety of effects, such as thermally activated magnetisation reversal [8, 9, 10, 11] or hot electron processes [8]. Junction heating had also been proposed as a possible origin [8], but was ruled out later, since it is not large enough to account for the effects [9]. Also, it would not explain the asymmetry of the back-hopping phenomenon. Park et al. [11] and Min et al. [9] mention the perpendicular STT as being the cause for this phenomenon but do not address the issue any further.

It should be noted that the back-hopping is not identical with another phenomenon occurring at high voltage biases called ‘bifurcated switching’ [76, 79], in which there are two (highly repeatable) switching branches. One is the regular switching between the P and AP state, whereas the other is a switching to a semi-stable state with intermediate resistance [79]. One explanation could be subvolume excitation.

# Experimental

---

In this chapter, the samples which are used in this thesis are introduced. The stack composition and the purpose of the individual layers are explained and the properties of the individual samples are listed.

During the course of this work, an experimental setup to perform measurements of the DC and high frequency switching behaviour was built. The parts of the setup that are shared by all experiments are described (electromagnet, sample contacting) and the characteristics of the equipment relevant for the work presented here are listed.

In the last section, the three experimental techniques used to gain information on the samples are described: DC R-H and R-I loops, the measurement of phase diagrams and thermally excited ferromagnetic resonance.

## 3.1 Samples

The samples used in this thesis were supplied by Dr. Jonathan Sun from IBM Research (New York, USA) via Prof. Stéphane Mangin (Université de Lorraine, France) and Prof. Jeffrey McCord (previously at the HZDR, now at the University of Kiel, Germany). The samples are CoFeB/MgO-based MTJs having both the reference and the free layer magnetised in-plane.

### 3.1.1 Stack composition

State-of-the-art MTJ stacks have a complex composition that has historically developed. The evolution in the stack design is shown in some principle steps in figure 3.1. In principle, two ferromagnetic layers with a non-magnetic material in between are sufficient to observe the magnetoresistance effect if the two layers have a different

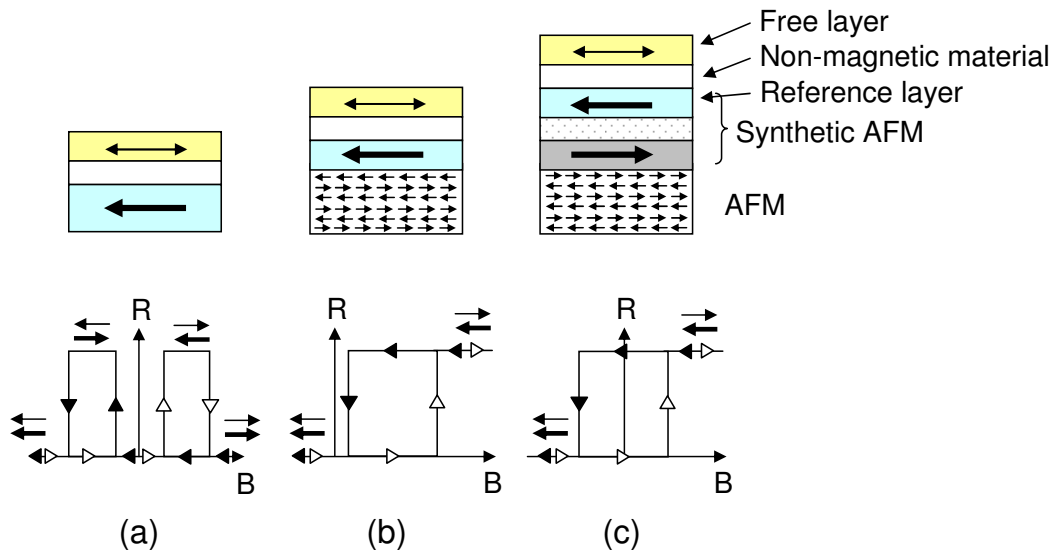


Figure 3.1: Historical evolution of the MTJ stack: (a) FM/NM/FM, (b) AFM/FM/NM/FM and (c) AFM/SAF/NM/FM where FM is the ferromagnetic material, NM the non-magnetic material, AFM the antiferromagnet and SAF the synthetic antiferromagnet consisting of two ferromagnets with a non-magnetic spacer. The small arrows in the MR loops refer to the magnetisation directions of the free and reference layer, respectively.

coercivity. This can be achieved if the layers differ in certain respects, for example if the thickness is different as in figure 3.1(a), or by using different materials. The layer with the larger coercivity is called the reference (or fixed) layer, while the other layer is referred to as the free layer. The MR loop of such a system consists of two switching events per branch since first the free layer and then the reference layer switches due to their different coercivity. This is problematic for an application as a storage device because only one state would be stable at zero applied magnetic field.

For applications it is desirable to 'fix' the magnetic moment of the reference layer in one direction. This can be achieved by placing an antiferromagnet (AFM, typically IrMn or PtMn) in contact with the reference layer, thereby making use of the exchange coupling arising at their common interface (see figure 3.1(b)). In the example shown here, a positive magnetic field is defined in the direction opposite to the magnetisation of the reference layer, setting the sample in the AP state, whereas switching to the P state will be observed for large enough applied negative magnetic field. The hysteresis curve is shifted from zero as a consequence of the uncompensated stray field arising from the reference layer. This shift can lead to the fact that still only one state is stable at zero magnetic field.

To circumvent this problem, state-of-the-art MTJ stacks designed for applications such as STT-MRAM or read heads include a so-called synthetic antiferromagnetic layer (SAF) as reference layer (see figure 3.1(c)). It consists of two ferromagnetic layers coupled antiferromagnetically via a thin, non-magnetic layer, with the lower film exchange coupled to the antiferromagnet and the upper layer serving as reference layer to the free layer. The closed magnetic field flux of the SAF reduces the stray field (dipolar coupling) on the free layer, and therefore the shift of its hysteresis curve.

The fabrication of these stacks is technologically very challenging: All of the layers need to be deposited in contact with their adjacent layers without loss of electrical or structural properties (lattice match). The stack optimisation in order to improve the TMR represents an extensive research field in itself. The following structural and material issues have to be addressed:

The **bottom electrode** should have a low roughness and a low resistance contribution.

The structure and quality of the **tunnel barrier** are essential for the TMR ratio. Typically, crystalline MgO is required to obtain high TMR values. This can be deposited either by direct rf sputtering from a stoichiometric target or by sputtering of metallic Mg and subsequent oxidation.

The anisotropy of the **free layer** should be neither too large (resulting in a high switching current density) nor too low (thermally not stable). Nowadays, typically  $\text{Co}_{20}\text{Fe}_{60}\text{B}_{20}$  is the free layer material of choice, since as-deposited CoFeB layers with a B concentration larger than 15 % are amorphous [80] and MgO films with highly ordered (001) texture can be grown on these amorphous layers (as long as the MgO films are thicker than four monolayers) [81]. After the deposition of the stack, the structures are annealed (around 350-400 °C [83]). Then, the B diffuses away from the CoFeB layer, initiating its subsequent crystallisation using the adjacent MgO(001) barrier as a template. Finally, a crystalline structure of bcc CoFe(001)/MgO(001)/CoFe(001) is formed. An example of the such a structure can be seen in a cross-sectional transmission electron microscope (TEM) image in figure 3.2 (taken from [82]).

Where the B is diffusing to is still under discussion: It is either diffusing towards the MgO barrier (forming an Mg-B-O composite at the interface MgO/CoFe, [84]) or further away from the barrier into the capping layer [83], which might be related to the quality of the barrier and/or the oxygen content (boron has a high affinity towards oxygen [80]).

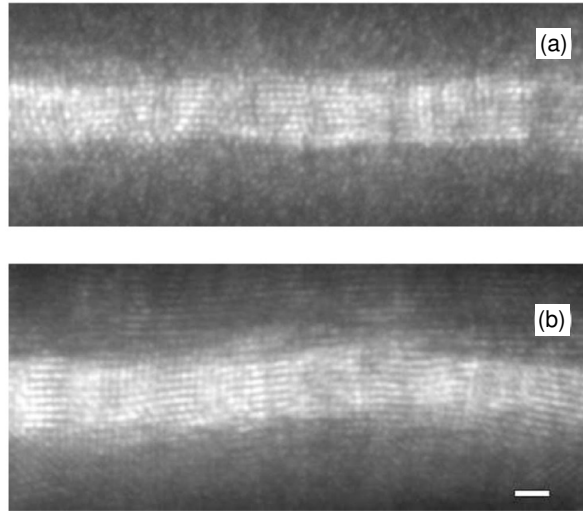


Figure 3.2: TEM image of an electron beam-grown 2.5 nm thick MgO barrier (a) as grown and (b) after annealing at 400 °C for 1 h, showing the bcc crystallisation of the two adjacent CoFe layers. The picture was taken from [82], the scale bar indicates 1 nm length.

### 3.1.2 Properties of samples used in this work

The stack composition of the IBM samples used in this thesis is given in table 3.1. The

Layer (purpose)	Material	Thickness (nm)
Top electrode (conductor)	PtMn	70
Top electrode (oxidation barrier, B getter)	Ru	10
Free layer	CoFeB	1
Free layer (increased lattice matching)	Fe	0.5
Tunnel barrier	MgO	0.95
SAF	Co <sub>70</sub> Fe <sub>30</sub>	0.5
	CoFeB	1.9
	Ru	0.85
	Co <sub>70</sub> Fe <sub>30</sub>	1.4
	CoFeB	0.5
Bottom electrode + AFM (conductor)	PtMn	17.5
Seed layer	Ru	1

Table 3.1: Stack composition of IBM-MTJ.

data presented in this work were obtained from six different samples whose properties are summarised in table 3.2.



Sample number	Size of ellipse (nm)	TMR	R(P)	H <sub>c</sub>	H <sub>shift</sub>
1	85 × 128	71 %	1023 Ω	1.64 mT	0 mT
2	85 × 128	70 %	1140 Ω	3.23 mT	-0.98 mT
3	85 × 128	78 %	993 Ω	3.33 mT	-0.2 mT
4	97 × 166	70 %	866 Ω	0.38 mT	+0.5 mT
5	97 × 166	72 %	1035 Ω	1.81 mT	-1.1 mT
6	85 × 140	63 %	1090 Ω	0.25 mT	-0.2 mT

Table 3.2: Properties of samples used in this thesis. A positive shift indicates a total coupling field favouring the P state.

## 3.2 Experimental setup

### 3.2.1 Overview of equipment for the different measurement techniques

There are three different types of measurement presented in this thesis:

1. DC resistance vs. field (R-H) and resistance vs. current (R-I) loops
2. Pulsed switching experiments and
3. Thermally excited ferromagnetic resonance.

All three different measurements use equipment which is connected to the same magnetoresistance setup. It consists of a Suss PM5 wafer prober for contacting the sample by high frequency (HF) prober tips, a water cooled electromagnet with a Kepco power supply for the magnetic field and a Keithley nanovoltmeter and current source for resistance measurements. The high frequency equipment includes a Picosecond pulse generator, a Tektronix oscilloscope and an Agilent spectrum analyser. A schematic of the different combinations of the parts of the equipment used for the various measurement techniques is given in figure 3.3. In the pulsed switching experiments, nanosecond voltage pulses were sent by the pulse generator and their reflections were recorded by the oscilloscope. A power splitter was used to connect both instruments simultaneously to the HF port of the bias tee in reflection mode. The frequency spectra in the TE-FMR measurements were recorded by the spectrum analyser. In both techniques a bias tee separated the DC and high frequency components of the signal.

The experimental setup that was built during the PhD, including all instruments, is shown in figure 3.4. Additional information about the setup concerning contacting, wiring and specifications can be found in the appendix A. Before the three measurement

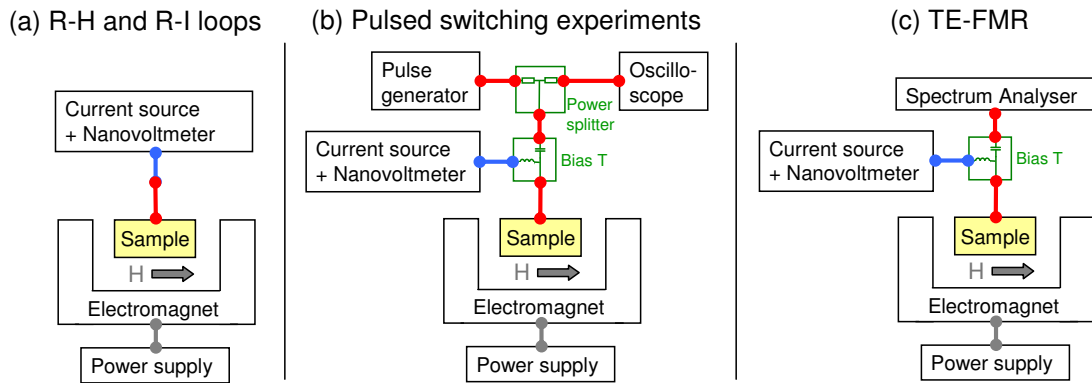


Figure 3.3: Overview over equipment used for the three different types of measurements presented in this work: (a) DC resistance vs. field and current loops, (b) pulsed switching experiments and (c) thermally-excited ferromagnetic resonance.

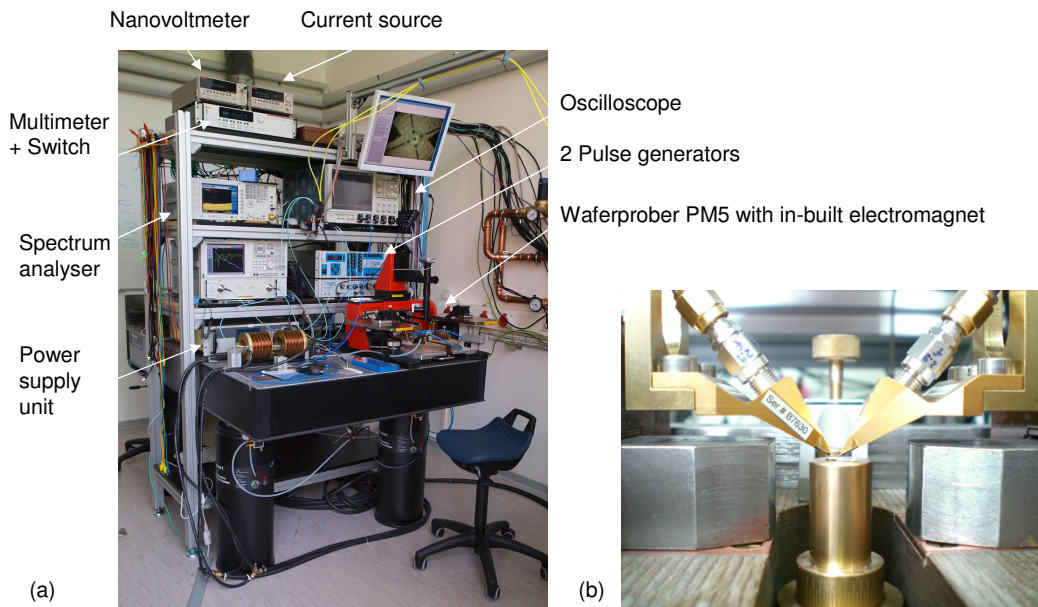


Figure 3.4: Experimental magnetotransport setup. (a) Overview of setup and equipment, (b) zoom on the sample contacting with two high frequency tips.

techniques are described in detail, the shared parts of the setup are discussed, namely the electromagnet and the sample contacting structure.

### 3.2.2 Electromagnet and Kepco power supply

The Kepco power supply (BOP 100-10 MG) for the electromagnet can be used either in constant current or constant voltage mode. In constant current mode it was noted that while setting the current value the coil current overshoots by 160 % as consequence

of the large inductance of the magnet. About 150 ms are required in order to finally adjust to the desired value. This overshoot would result in the scale of the R-H loop being incorrect. To avoid the overshoot, the magnetic field was therefore set to change in small steps with an amplitude of about half of the allowed overshoot. This reduced the speed of setting the field, but ensured that the desired field value is not exceeded. The magnetic field was calibrated before the measurements were performed by using a Hall probe in the place of the sample. The maximum field for a pole shoe gap of 50 mm (which was used in this thesis) was about 0.12 T. The minimum step size at this distance is about 0.1 mT. Smaller step sizes or higher maximum fields can be easily achieved by increasing or decreasing the pole shoe distance.

### 3.2.3 Contacting of the sample

An example of contacting a sample for both the DC and high frequency measurements is given in figure 3.5. It should be noted that a ground-signal-ground (GSG) tip was used even though the measurement was performed in the 2-point-probe method. There are two reasons for that: The sample design included only two contact pads and the pulse generator can only generate pulses of one current sign. Therefore, the contact needed to be changed by changing the tip connection to invert the sign of the current for the pulsed measurements. For a GSG tip, this is conveniently done by moving the tip such that the signal tip either touches the bottom or top electrode. The third tip connects to the ground electrode of the next sample and does not influence the measurement.

Figure 3.6 shows the IBM samples with a larger magnification. The MTJ itself is hidden beneath the current lead to the top electrode.

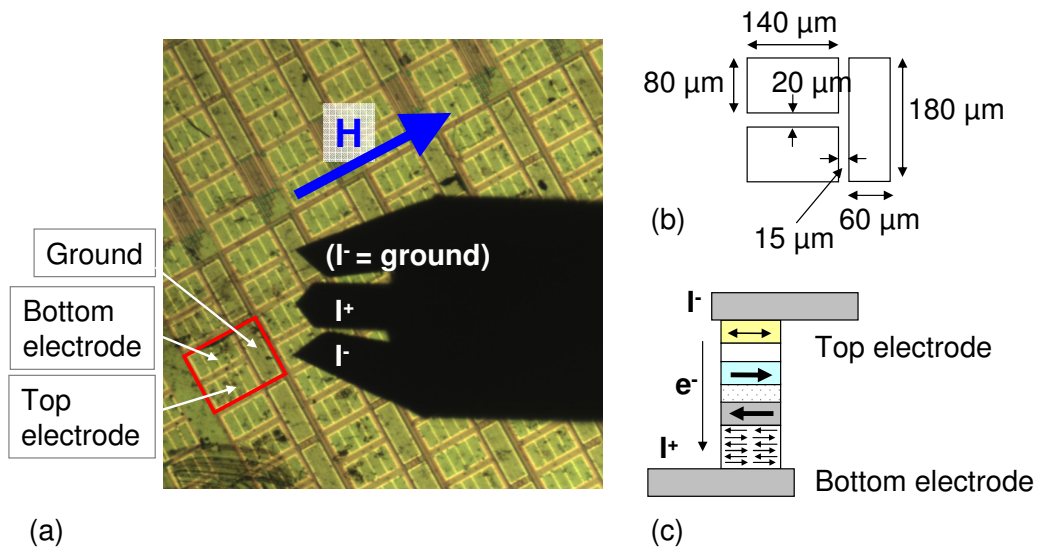


Figure 3.5: (a) Contacting of IBM-sample with  $150\ \mu\text{m}$  GSG HF tip. The sample to the left of the contacted sample is indicated by a red frame, the field direction is in the plane parallel to the easy axis of the sample (blue arrow). Here, the sample was contacted so that positive current favours the AP state (electrons are flowing from the top electrode to the bottom electrode). (b) Geometrical dimensions of sample electrodes and (c) side view of sample including the top and bottom electrode.

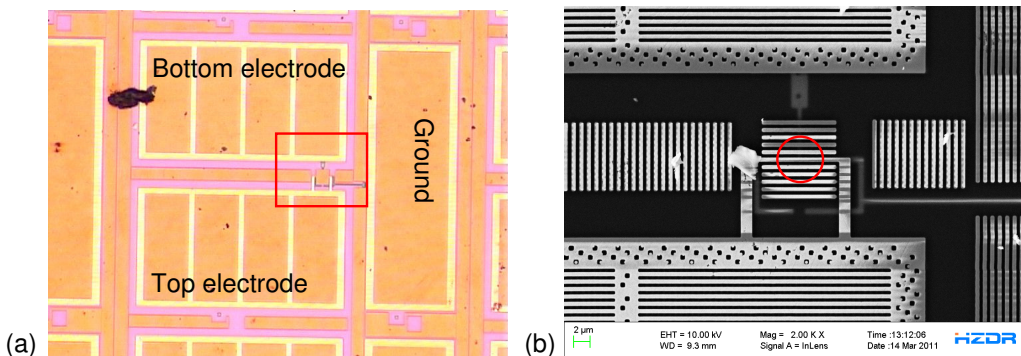


Figure 3.6: IBM sample pictures: (a) Light microscopy image, the red frame indicates the zoomed area of (b) SEM image with bottom contact (at top) and top contact (at bottom). The nanopillar with the MTJ is hidden below the current lead to the top electrode (indicated by red circle). The SEM image was taken by M. Höwler.

### 3.2.4 Principle specifications of equipment

Principle specifications of the **DC equipment** which are relevant for the work presented in this thesis are given in table 3.3. More general information is included in table A.1 in the appendix. The Keithley nanovoltmeter and current source were used to determine the DC resistance in all three measurement types presented in section 3.3. The

Name of device	Principle specifications
Keithley 2182A Nanovoltmeter	Resolution: 10 mV range: 1 nV with internal R > 10 GΩ 100 mV range: 10 nV with internal R > 10 GΩ 1 V range: 100 nV with internal R > 10 GΩ
Keithley 6221 DC/AC current source	Typical noise: 2 μA range: 200 pA peak-peak/40 pA RMS 20 μA range: 2 nA peak-peak/0.4 nA RMS 200 μA range: 20 nA peak-peak/4 nA RMS 2 mA range: 200 nA peak-peak/40 nA RMS
Keithley 2401 source meter	Source accuracy (2 V range): 0.02 % + 600 μV Resolution for R measurement (2 kΩ range): 10 mΩ

Table 3.3: Selected specifications of DC equipment of setup relevant for the measurements in this work.

specified resolution and noise of the two instruments was considered when estimating the error bars for the R-I and R-V loop measurements presented in section 3.3.1. The Keithley 2401 source meter served as both a voltage source and current meter for the low temperature measurement presented in section 4.1.2.4.

The principle specifications of the **HF equipment** are given in table 3.4. More general information is included in table A.2 in the appendix. The specifications can be used to estimate the bandwidth limitations and the attenuation of the system. For near-Gaussian response systems, the bandwidth can be calculated from the rise time of the pulse [85]:

$$BW = \frac{0.35}{t_r}, \quad (3.1)$$

where  $BW$  is the bandwidth (defined at an attenuation of -3 dB) and  $t_r$  is the rise time (defined as the time the pulse takes to rise from 10 % to 90 % of the pulse amplitude). For a cascade of Gaussian response systems, the output rise time  $t_r(out)$  of the whole system is the root-sum-of-squares of the individual rise times  $t_{rn}$  [85]:

$$t_r(out) = \sqrt{(t_{r1})^2 + (t_{r2})^2 + \dots + (t_{rn})^2}. \quad (3.2)$$

Using eq. (3.1) and (3.2) several estimations can be made:

- The rise time of the pulse generator (55 ps) corresponds to a bandwidth of about 6.4 GHz. Therefore, even if the oscilloscope bandwidth is limited to 10 GHz in order to reduce the noise level, this is still sufficient to record the full frequency content of the pulse from the pulse generator.
- The output rise time of the whole system used for the pulsed switching experiments can be estimated from the rise time of the cables (13.2 ps), the splitter

Name of device	Principle specifications
Picosecond pulse generator PSPL 10060A	Rise time: 55 ps Fall time: 115 ps Range of duration: 100 ps...10 ns (in 2.5 ps steps)
Tektronix Oscilloscope DPO72004B	Rise time: 18 ps Sensitivity range: 10 mV/div to 1 V/div in 1-2-5 sequence Noise in 10 mV range: 0.49 mV (at 10 GHz)
Agilent Spectrum analyser MXA N9020A	Frequency range: 20 Hz...26.5 GHz Internal preamplifier: +20 dB gain between 100 kHz to 26.5 GHz; noise figure (at 5 GHz): 9 dB Resolution bandwidth: 1 Hz...8 MHz Average noise level (at 5 GHz): -166 dBm (preamp on)
Picosecond Power Splitter 5336	Bandwidth: DC to 20 GHz Delay: 180 ps Insertion loss, AC: 6.0 dB $\pm$ 0.5 dB Input impedance: 50 $\Omega$ $\pm$ 0.3 $\Omega$ max.
Mini-Circuits Bias-Tee ZX85-12G+	Frequency range: 0.2...12 GHz DC resistance from DC to RF+DC port: 1.8 $\Omega$ Insertion loss: 0.6 dB Max. DC voltage and current: 25 V; 400 mA
True Blue high frequency cables	Max. operating frequency: 26.5 GHz Attenuation (at 5 GHz): 0.59 dB/m Propagation delay: 4.56 ns/m

Table 3.4: Selected specifications of the high frequency equipment of the setup.

- (17.5 ps) and the bias tee (30 ps) as  $t_r(out) = 37$  ps (corresponding to a bandwidth of 9.4 GHz). This is the shortest rise time that can be applied in the circuit. Since the rise time of the pulse generator is larger than this value, the equipment is sufficient to transmit all frequency components from the generated pulses.
- In section 3.3.2.5 the losses in the system and the time delay of the pulse are estimated for the pulsed switching experiment for the applied voltage pulse amplitudes and cable lengths of the setup. The losses in the signal path are determined by summing up the attenuation values from the cables (times the length), the splitter and the bias tee. Furthermore, the time delay of the pulse can be calculated from the cable lengths and reflected parts of the pulse from the oscilloscope time trace can then be assigned to reflections at certain interfaces in the system.

### 3.3 Experimental techniques

The DC and high frequency behaviour of the MTJ samples was investigated by several experimental techniques. These include resistance versus field loops (R-H loops), resistance versus current loops (R-I loops), measurements of full phase diagrams (off- and on-pulse) and thermally excited ferromagnetic resonance. The working principles and basics of the individual techniques are explained in the following subsections.

#### 3.3.1 Measurement of DC R-H and R-I loops

Two LabVIEW programs were set up that use the Keithley current source, Keithley nanovoltmeter and the magnet (controlled by the Kepco power supply unit) to loop through the magnetic field at a constant current (R-H) or through the applied current at a constant magnetic field (R-I) while measuring the resistance. Input parameters are the waiting time between the individual steps, the respective start, stop, step and constant values for both field (in voltage for the power supply) and current. The current/field sweep loops from the maximum positive value to the maximum negative value and back.

A typical hysteresis loop for the MTJ samples used in this thesis can be seen in figure 3.7. Here, positive magnetic field favours the AP state whereas negative field

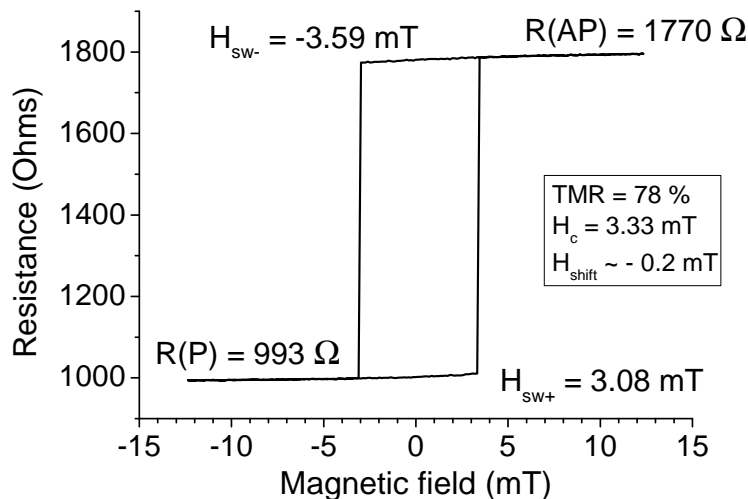


Figure 3.7: Typical minor magnetoresistance loop of sample 3 taken at a constant current of 10  $\mu$ A. In the small magnetic field range applied only the free layer is changing the magnetisation direction.

favours the P state. The switching fields  $H_{sw+}$  and  $H_{sw-}$  are not symmetric. This

shift can be due to a small AP dipolar coupling to the reference layer and/or an AP interlayer exchange coupling across the tunneling barrier. Switching occurs abruptly and without any steps, thereby indicating a single-domain-like behaviour with coherent magnetisation reversal. The sample has an elliptical cross-section with axes lengths of 85 and 128 nm. The TMR is 78 % and the RA product  $8.5 \Omega\mu\text{m}^2$ .

An example for switching the magnetisation by STT can be seen in figure 3.8. For

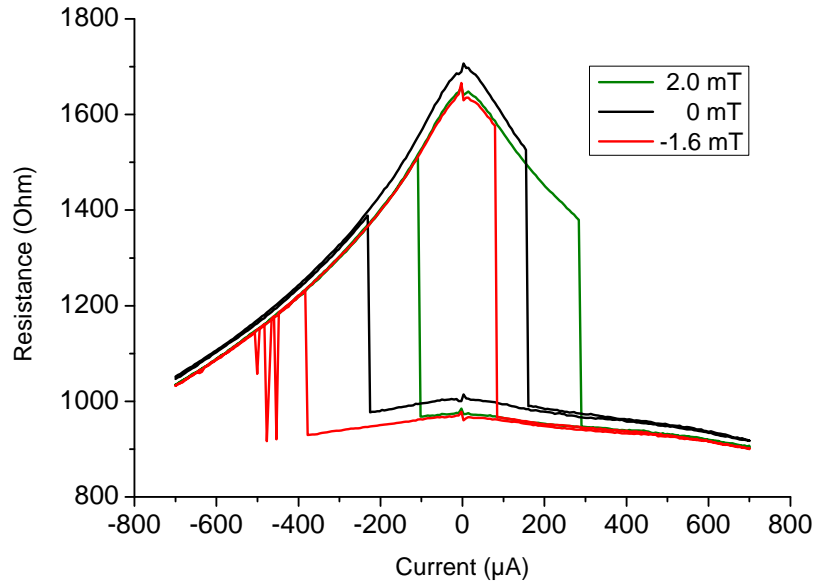


Figure 3.8: Current-induced switching with a DC current and different applied magnetic fields in the easy axis direction for sample 1. Switching between the P and AP states is indicated by sharp changes in the resistance. The critical switching current at zero magnetic field is around  $200 \mu\text{A}$  which corresponds to a critical current density of  $2.3 \times 10^6 \text{ A/cm}^2$ .

the positive current direction, the electrons flow from the fixed to the free layer, thus favouring the P state. Accordingly, a negative applied current favours the AP state. The bistable hysteretic region is shifted by applying an additional magnetic field: If the field favours the same state as the current, it is easier to switch and the switching occurs at lower current values (for positive field and negative current and vice versa). The irregular resistance values for negative field and large negative current show the so-called 'back-hopping' phenomenon which is discussed in detail in section 2.5.4.

An example for an approximate **sweep time** for the R-H loop is 120 s for a total of 200 points (measuring between  $\pm 12.4 \text{ mT}$  in  $0.25 \text{ mT}$  steps), with a waiting time between the magnetic field steps of 0.5 s. A typical R-I loop between  $\pm 700 \mu\text{A}$  with  $5 \mu\text{A}$  step size (560 points) and 0.2 s waiting time takes about three minutes.



The specifications of the current source and nanovoltmeter given in table 3.3 can be used to estimate the limits of the measurements for the specific samples properties. With a noise of the current source of 200 nA (peak-to-peak) in the range for the R-I loops, the **switching currents** (around 200  $\mu\text{A}$ ) are larger by a magnitude of three and can therefore be determined with a good accuracy. As a rough estimate of the **limit of the resistance resolution** for both the R-H and R-I loop, the specified resolution of the nanovoltmeter at the smallest range (1 nV) and the typical current for the determination of the MR loop (10  $\mu\text{A}$ ) give a resistance resolution of 0.1  $\text{m}\Omega$ .

### 3.3.2 Measurement of phase diagrams: off and on-pulse

#### 3.3.2.1 Goal of experiment

The goal of measuring the switching phase diagram is to determine the borders of the stability regions for P and AP for the MTJ and compare them with the analytical phase diagram. Ideally, the spin-transfer torque parameters can then be extracted and compared with the results from other measurement techniques (TE-FMR, ST-FMR). There are two ways to perform the measurement: off- and on-pulse. In an off-pulse experiment, the state of the sample is determined by detecting the resistance at a low voltage bias before and after the pulse. On-pulse measurements detect the reflected pulse signal itself to determine the state of the sample (time-resolved in single shot mode). Measurements were performed combining both the on-pulse and off-pulse technique. The two techniques are outlined in detail below.

#### 3.3.2.2 Real-time (on-pulse) measurement

Voltage pulses of ns-scale duration and variable amplitude were applied to the sample in reflection mode (see figure 3.9). The MTJ sample terminates a 50  $\Omega$  coaxial cable. A voltage pulse from the pulse generator is split by a power splitter, so that half of the pulse is injected into the MTJ, whereas one quarter is reflected and the other quarter is terminated by the single-shot 20 GHz oscilloscope. The voltage pulse is partially reflected by the MTJ because of its impedance mismatch. The ratio of the reflected voltage is given by the so-called reflection coefficient  $\rho$  [86]:

$$\rho = \frac{Z_{term} - Z_0}{Z_{term} + Z_0}, \quad (3.3)$$

where  $Z_{term}$  and  $Z_0$  are the impedance of the sample and that of the transmission line ( $50 \Omega$ ), respectively. The reflected voltage pulse is then again split by the power splitter, and half of the reflected signal is recorded by the oscilloscope, whereas the other half is terminated by the pulse generator. Depending on the state of the sample (P or AP),

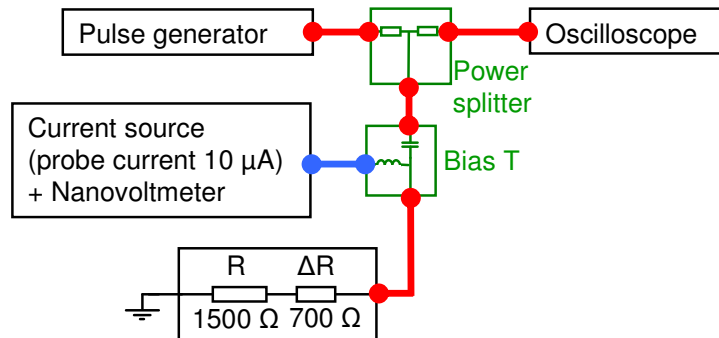


Figure 3.9: Schematic of the experimental setup for the phase diagram measurement in reflection mode. Switching of the sample state results in a resistance change that can be detected both by the DC current as well as with the single-shot oscilloscope.

the reflection coefficient differs and therefore the current state of the sample is revealed by the amplitude of the reflected pulse. Since switching is non-deterministic at room temperature and there are small angle deviations of the magnetisation from the easy axis for each switching attempt due to thermal fluctuations, it is essential to detect the reflected pulse in single-shot mode in order to investigate individual switching events.

To separate the change in the magnetoresistance from the background of the reflected pulse, reference signals at positive and negative magnetic fields slightly above the coercivity were taken before the measurement. To increase the signal-to-noise ratio (SNR), these reference signals were averaged for ten times. By subtracting the reference signal from the actual measurement signal all pulse distortions introduced from the setup could be removed. The state of the sample during the pulse can then be determined from analysing the oscilloscope traces for the different magnetic fields and voltage amplitudes. The results are summarised as the on-pulse phase diagram.

### 3.3.2.3 Off-pulse measurement

A small DC detection current ( $10 \mu\text{A}$ ) was applied to the MTJ through a bias tee during the experiment to determine the MTJ resistance (using the nanovoltmeter) after saturation, as well as before and after the voltage pulse, thus yielding the off-pulse phase

diagram. By combining the high frequency oscilloscope data and the off-pulse resistance measurements the resistance state of the MTJ can be tracked at all times.

### 3.3.2.4 Measurement sequence

The measurement sequence for both types of phase diagram (shown in figure 3.10) was performed as follows:

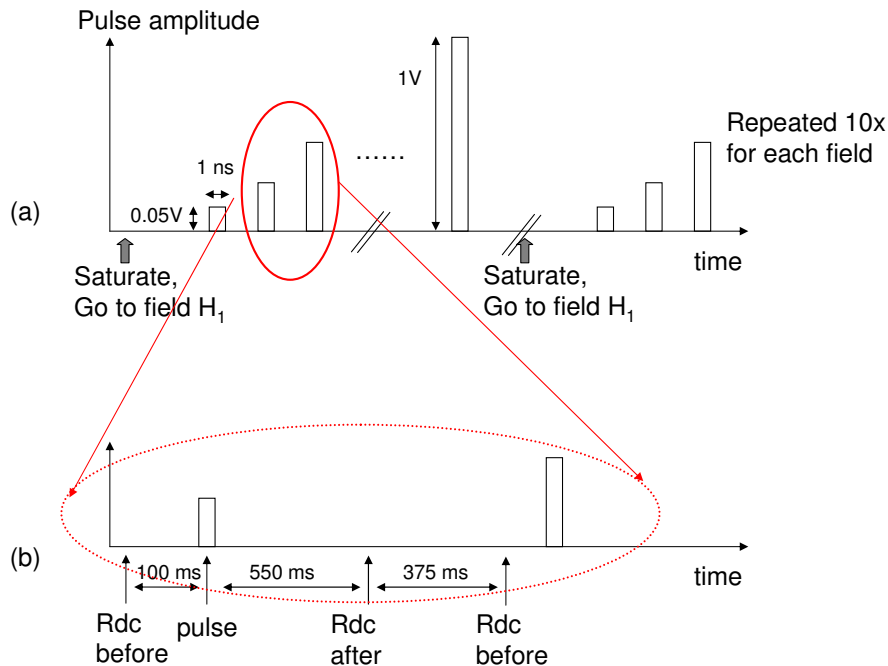


Figure 3.10: Schematic of measurement sequence for obtaining the phase diagram. (a) shows the application of a pulse sequence with increasing amplitudes (repeated ten times at each magnetic field) and (b) shows the time scale of the DC resistance measurements before and after the pulse.

1. Take 10 reference measurements in each state (P/AP), average;
2. Saturate sample in the P (AP) state;
3. Set magnetic field to the desired field in small steps to prevent an overshoot of the magnetic field;
4. Apply a sequence of voltage pulses with increasing amplitude and a step of 0.05 V (if adjustable by the pulse generator) in one sequence;
5. Repeat steps 2-4 for 10 times at the same magnetic field;
6. Repeat steps 2-5 for the next magnetic field.

The resistance of the sample was probed both by measuring the DC resistance before and after the pulse as well as by detecting the time-resolved pulse reflection with the

single-shot oscilloscope. Therefore the state of the sample was probed at all times: before, during and after the pulse. Repeating the measurement 10 times at the same field value allowed to gain a statistical average of the switching probability.

### 3.3.2.5 Measurement example and discussion

An example of a single-shot measurement is given in figure 3.11, depicting the detected

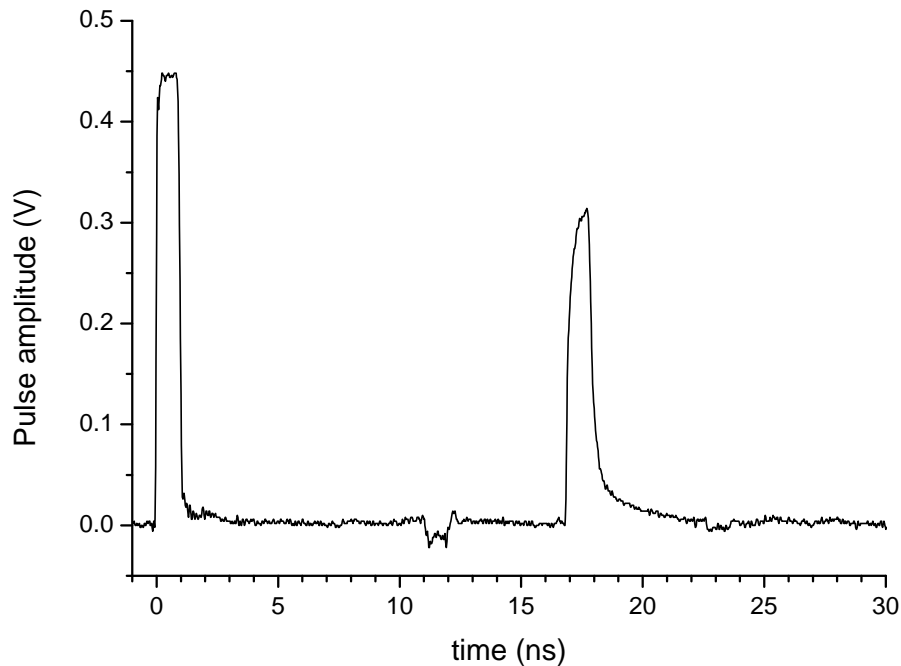


Figure 3.11: Full reflection of pulse as detected by the oscilloscope at a pulse amplitude of 0.9 V. The sample is in the AP state ( $R = 1430 \Omega$ ).

signal at the scope for a 1 ns pulse of 1.8 V amplitude. The time scale is adjusted so that the first pulse arrives at  $t = 0$  ns at the scope. This is the part of the pulse directly transmitted to the scope after passing the splitter ( $1/4$  of the amplitude = 0.45 V). The second pulse, with a delay of 16.3 ns, was sent to the sample and got reflected. The delay is equivalent to a transmission line length of 3.6 m, which is double the length of the cable from the splitter to the sample.

A small negative pulse is recorded after a delay of about 11 ns, which is equivalent to a transmission line length of 2.4 m. This is double the length of the cable between the splitter and the bias tee. Therefore, this pulse can be identified as a reflection at the bias tee, which is negative for the case of an impedance below  $50 \Omega$ .

The signature of an open end pulse reflection (with floating HF tips) is similar to the reflection shown in figure 3.11, since the sample also has a higher impedance than the

50  $\Omega$  circuit. The distortions of the pulse shape are therefore mainly due to impedance mismatches and reflections at several interfaces or bandwidth limitations in the system (cables, adapters, bias tee).

Taking the losses of splitter and bias tee into account, the height of the reflected pulse detected on the oscilloscope is smaller than the expected value of 0.367 V. Table 3.5 gives some examples for the differences between theoretical and real signal heights for the different voltage pulse amplitudes. For the calculation of the theoretical signal,

$V_{\text{pulse}}$	signal (AP)		signal (P)	
	experiment	% difference from theoretical value	experiment	% difference from theoretical value
0.05	0.0195 V	4.7 %	0.0181 V	7.5 %
0.5	0.1863 V	9.5 %	0.1852 V	6.7 %
1	0.3456 V	17.9 %	0.3418 V	13.9 %

Table 3.5: Comparison of maximum theoretical and actual signal height for some selected voltage pulse amplitudes for the P and AP configuration in the on-pulse phase diagram measurement. The theoretical values are given as the percentage by which they exceed the experimentally obtained data.

the attenuation of splitter (-6 dB) and bias tee (-0.6 dB) were taken into account twice and the reflection of the sample was calculated from the reflection coefficient at the specific DC resistance for the P and AP configuration. The reasons for the discrepancy between theory and experiment are likely to be additional losses in the cables and an increased attenuation at the sample at higher frequencies. The cable attenuation is given as 0.59 dB/m at 5 GHz and 0.85 dB/m at 10 GHz in the data sheet. If the value for 5 GHz was taken into account, the theoretical signal would be smaller than the experimentally determined. Although this seems contradictory at first, it confirms the calculations shown here because the attenuations are frequency dependent and the values given in the data sheets are maximum values.

From the actual signal heights it is already visible that the signal difference is very close to the resolution limit for the lowest pulse amplitude (noise at 10 GHz bandwidth and 10 mV/division  $\approx$  0.49 mV). The maximum actual difference signal increases from 1.4 mV for 0.05 V pulses to 4.0 mV at the largest pulse height of 1.0 V, which is clearly detectable.

The sample rate was set to the maximum of 50 GS/s corresponding to taking data points every 20 ps. To achieve a maximum SNR, the bandwidth of the oscilloscope was reduced to 10 GHz and it was kept at the smallest possible vertical range (10 mV/di-

vision) while the reflected pulse of the sample was offset to detect the top of the pulse at higher amplitudes. This is an internal function by the oscilloscope applying a DC offset voltage to the input, which brings the top of the pulse into the input range of the amplifier, but implies that the normal line voltage is out of range. At the start of the pulse, the input amplifier has to come out of saturation, but since the actual pulse is not overshooting, it appears to recover quickly enough so as not to distort the signal.

### 3.3.2.6 Analysis

An automated analysis was performed in order to maintain defined and constant conditions for the determination of switching events and to save time. During the analysis, the user has to monitor the individual oscilloscope traces to check if there are any deviations caused by changes in the contact resistance, which would lead to incorrect results for the switching events. The analysis was programmed in LabView and was carried out in several steps:

1. Removal of jitter: To adjust the measurements horizontally, the derivatives of AP/P reference and measurement are cross-correlated, respectively. Since all pulses of the same amplitude are equivalent in shape except for a certain factor due to the reflection coefficient, the maximum slope during the rising edge occurs at the same time. The cross correlation yields a shift of maximum  $\pm 1$  data point ( $\pm 20$  ps) which is accounted for in the further analysis.
2. Background subtraction: Calculation of the difference signal with the two reference signals: (reference(AP) minus measurement) and (measurement minus reference(P)), thus identifying the state of the sample at each time of the pulse.
3. Determination of the MTJ state at the start and the end of the pulse: Both difference signals are integrated over a period from 0.22 to 0.42 ns (start of pulse) and 0.72 to 0.92 ns (end of pulse). The state is defined by the smaller of the two integrals. (Ideally, one should cancel, the other should correspond to the signal height).

To illustrate the temporal definition of the start and end states, figure 3.12 displays a series of on-pulse traces, measured with 1 ns voltage pulses of different amplitudes on the same sample as used in paragraph 4.1.2.2. The signal had to be offset vertically for voltage amplitudes above 0.25 V in order to detect the top of the pulse at the smallest possible vertical range, leading to a cut-off of the lower part of the reflected pulse.

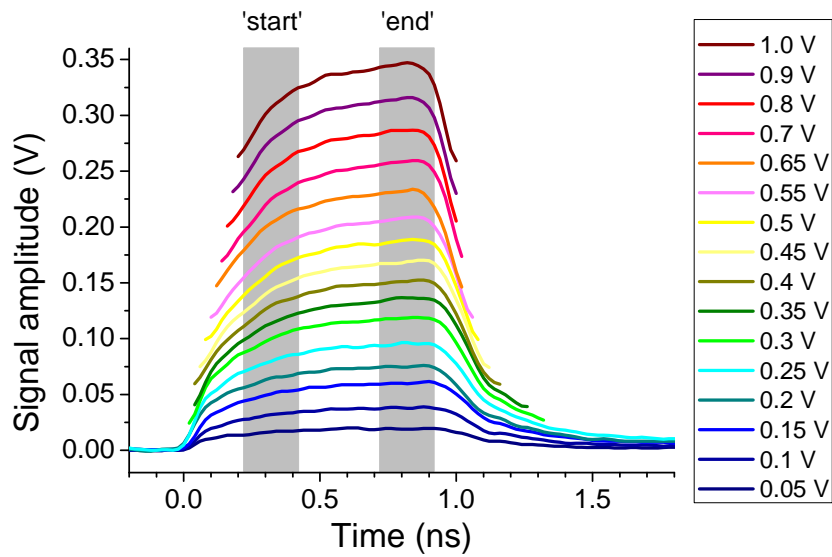


Figure 3.12: Reflected signals from sample 3 while switching from the AP state for different applied voltage pulse amplitudes at a magnetic field of  $-1.5$  mT. The vertical offset of the oscilloscope had to be increased for larger pulse amplitudes - therefore, the start of the pulse could not be detected for higher amplitudes. All pulses start at 0 ns and are 1 ns long, deviations from the rectangular shape are due to reflections or imperfect impedance matching of the setup. The time ranges used for the automated analysis of the start and end state are indicated by the grey areas.

This explains why the start and end states of the sample were not determined exactly at the edges of the pulse, but in the time range of 0.22 to 0.42 ns (start) and from 0.72 to 0.92 ns (end) after the start of the pulse (highlighted in grey in figure 3.12). Consequently, this analysis method might miss switching events at the very end of the pulse, and will detect switching events at the very start as an already altered start state. The fact that the start and end states are determined over a time range and not at an exact point in time was necessary for a stable analysis but might also result in missing switching events at the borders of the time range. Moreover, back-hopping events between these time intervals would not be detected with this analysis method. Therefore the time ranges were kept as short as possible while retaining a reliable analysis.

### 3.3.3 Thermally-excited ferromagnetic resonance

Thermally excited ferromagnetic resonance (TE-FMR) can be used to determine the spin-transfer torque parameters [69]. In this technique, the (in-plane magnetised) sample is subjected to both an in-plane magnetic field and a DC current but, in contrast to current-driven magnetisation precession, both field and in-plane STT favour the same

state (parallel or antiparallel) [64]. Therefore, the in-plane spin-transfer torque acts to increase the damping and cannot drive magnetisation dynamics. The high frequency signals obtained appear at the ferromagnetic resonance frequency corresponding to the effective field which includes the perpendicular STT [64].

The measurement setup is shown in figure 3.13. Negative field and positive current

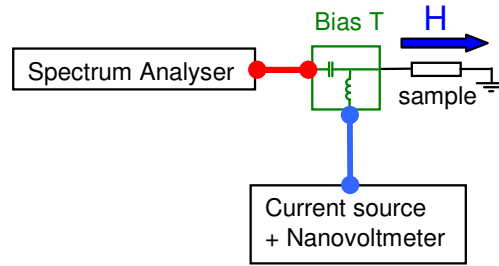


Figure 3.13: Schematic of the experimental setup for the thermally excited ferromagnetic resonance (TE-FMR). An internal preamplifier of the spectrum analyser was used to increase the signal-to-noise ratio while a certain DC bias was applied. The applied magnetic field was in the direction of the easy axis of the sample.

favour the parallel state. The magnetic field was applied along the easy axis of the elliptical sample and the current perpendicular to the nanopillar interfaces. The spectra were recorded with a spectrum analyzer with a built-in preamplifier. For each constant field, different DC current values were applied, so that the equivalent maximum voltage across the barrier did not exceed 0.3 V. For this, the current-voltage characteristic of the sample was determined previously in the two (saturated) states. Before the analysis, the background spectrum (at zero DC current) and the amplification were subtracted.

Increasing the DC bias voltage at the sample influences both the peak frequency  $f_r$  and the linewidth  $\Delta f$ . It was shown by Petit et al. [69] that in the linear regime the perpendicular (field-like) spin-transfer torque changes the peak frequency, while the in-plane torque influences the linewidth of the signal. Depending on the field direction, the effective field  $B_0$  is either increased (if both perpendicular torque and external field favour the same state) or decreased (if they favour opposite states). This leads to an increase or decrease in  $f_r$  according to the Kittel formula [87]:

$$2\pi f_r = \gamma \sqrt{B_0(B_0 + \mu_0 M_s)}. \quad (3.4)$$



To a first order approximation, the resonance frequency for the TE-FMR is given by [69]:

$$f_r = \frac{\gamma}{2\pi} \sqrt{(B_{\text{eff}} + B_{\perp})(B_{\text{eff}} + B_{\perp} + \mu_0 M_s)}, \quad (3.5)$$

where  $B_{\perp} = \frac{a_{\perp}}{M_s \text{Vol}}$ . Therefore, the bias-dependence of the perpendicular spin-transfer torque can be determined from the shift in the peak position with the applied voltage.

In the LLG macrospin model, the linewidth of the peak is set by the damping. In the case of TE-FMR, the in-plane spin-transfer torque acts in the same direction as the damping and it will therefore increase the linewidth of the peak independently of the state of the sample. To a first order approximation, the linewidth for a precessional peak of the TE-FMR near static equilibrium is given by [69]:

$$\Delta f_r(V) = \frac{\gamma}{2\pi} \alpha (\mu_0 M_s + 2B_{\text{eff}}) + 2 \frac{\gamma}{2\pi} B_{\parallel}(V). \quad (3.6)$$

Here,  $B_{\parallel} = \frac{a_{\parallel}}{M_s \text{Vol}}$ . The damping factor  $\alpha$  can be determined from the linewidth extrapolation to zero bias voltage, where the bias-dependence of the in-plane STT does not contribute. The in-plane spin-transfer torque is then estimated from the linewidth change with the applied voltage.

The two spin-transfer torque components can thus be independently calculated from the TE-FMR spectra.

It should be noted that for small damping factors  $\alpha$ , the power spectral density of the TE-FMR precessions has a Lorentzian shape with an amplitude inversely proportional to  $\Delta f B_{\text{eff}}$  [70], therefore lower external magnetic fields will result in signals with larger amplitudes.



# 4

## Results and discussion

---

This chapter summarises the theoretical and experimental work carried out in order to extract the in-plane and perpendicular spin-transfer torque parameters. At first, the critical switching voltages and switching fields for a magnetic tunnel junction are derived. For this, the Landau-Lifshitz-Gilbert equation is analytically and numerically solved, taking into account both the in-plane and perpendicular STT terms. We consider a generalised device configuration which can describe nanopillars with in-plane and/or perpendicular-to-the-plane anisotropy. The calculated phase diagrams are then extrapolated to three particular configurations and compared to theoretical and experimental results on metallic nanopillars as well as our measured phase diagrams on in-plane MgO-based MTJs.

We present phase diagrams measured via two methods: ‘on-pulse’ and ‘off-pulse’ (see chapter 3.3.2), which can, in principle, be fitted with the analytical formulae in order to extract the bias-dependence of the two STT terms. Alternatively, the in-plane and perpendicular STT parameters can be determined from thermally-excited ferromagnetic resonance (TE-FMR), discussed in section 3.3.3. At room temperature, the two methods yield values which differ by one order of magnitude, reflecting the different impacts of thermal effects on the two approaches.

### 4.1 Switching phase diagrams of MTJs

Phase diagrams summarise the states allowed for the free layer of the magnetic tunnel junction for given external conditions at different applied fields and electrical bias (see figure 2.13). Experimentally, on such a phase diagram a cross-section along the horizontal (field) axis corresponds to a typical R-H sweep measured at constant bias. The horizontal line at  $V = 0$  intersects the critical lines in two points corresponding to the

anisotropy field  $\pm\mu_0 H_k$ . A vertical cut corresponds to an R-I (or R-V) measurement. Critical lines marking the stability of given states can be fitted with analytical formulae. In the next section, the critical voltages and their dependence on the external field are derived for an MgO-based MTJ, assuming a linear (quadratic) dependence of the in-plane (perpendicular) STT term on the bias voltage.

### 4.1.1 Theory: Calculating the phase diagram

We analytically and numerically solve the Landau-Lifshitz-Gilbert (LLG) equation. To this end, we employ a similar approach as described by Grollier et al. for fully metallic devices [88]. Note that there are two main differences between spin-valves and MTJs:

1. Metallic spin-valves demonstrate a strongly skewed dependence of the in-plane STT on the angle between the magnetic moments of the free and the reference layer [30], while this asymmetry is not present in MgO-based MTJs [4, 5, 75].
2. The field-like STT can be neglected in metallic structures [89], whereas it can reach up to 30 % of the in-plane STT in MgO-based MTJs and needs to be considered [4, 5, 75].

Unlike in the calculations of Grollier et al., here, we take into account both STT terms. Furthermore, we assume that the in-plane (perpendicular) STT term has a linear (quadratic) dependence on the applied voltage, and that the perpendicular STT always favours the AP state [4, 5, 75].

The system we consider is an Fe/MgO/Fe-type MTJ with a generalised geometry, characterised by the following:

- The free layer has two generalised orthogonal anisotropy components: one along an in-plane direction ( $H_{kx}$ ) and the other normal to the plane of the layers ( $H_{kz}$ ), as seen in figure 4.1. The latter can be positive or negative, depending on whether the free layer is magnetised in- or out-of-plane.
- The magnetic moment of the reference layer is parallel to the negative  $z$ -direction, hence  $\vec{p} \parallel -\vec{u}_z$ .
- The external field is applied along the  $z$  axis and positive field favours the AP state.
- Positive voltage implies electrons flowing from the reference layer to the free layer (i.e. for positive voltage, the in-plane STT favours the P state).
- Magnetostatic coupling fields are not considered.

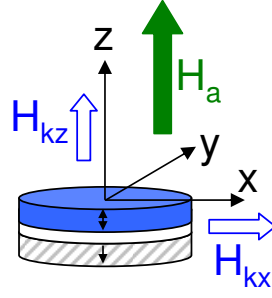


Figure 4.1: Schematic of the MTJ and field definitions for the general case of an MTJ with two orthogonal anisotropy components. The external field  $H_a$  is applied along the  $z$  axis.

- The orders of magnitude for various material parameters are assumed to be in the typical range for Fe/MgO/Fe-MTJs.

For this system, the LLG equation in the presence of an applied bias voltage is written as:

$$\frac{d\vec{m}}{dt} = -\gamma(\vec{m} \times \mu_0\vec{H}_{\text{eff}}) + \alpha \left( \vec{m} \times \frac{d\vec{m}}{dt} \right) - \gamma a'_{\parallel} V (\vec{m} \times (\vec{m} \times \vec{p})) + \gamma a'_{\perp} V^2 (\vec{m} \times \vec{p}) . \quad (4.1)$$

Here,  $\vec{m}$  and  $\vec{p}$  are the unit magnetisation vectors of the free layer and the polarisation of the incident electrons (assumed to be collinear with the reference layer magnetisation), respectively.  $\gamma$  is the gyromagnetic ratio and  $\alpha$  is the Gilbert damping coefficient.  $\mu_0\vec{H}_{\text{eff}}$  is the effective field. It includes the external magnetic field  $\mu_0 H_a$  and the anisotropy field  $\mu_0 H_k$ :  $\mu_0\vec{H}_{\text{eff}} = \mu_0(H_{kx}m_x\vec{u}_x + H_a\vec{u}_z + H_{kz}m_z\vec{u}_z)$  ( $\vec{u}_i$  being the unit vector along the  $i$  axis).  $a'_{\parallel} = \frac{a_{\parallel}}{M_s \text{Vol}}$  and  $a'_{\perp} = \frac{a_{\perp}}{M_s \text{Vol}}$  contain  $M_s$ , the saturation magnetisation, and  $\text{Vol}$ , the volume of the free layer. The prefactors  $a_{\parallel}$  and  $a_{\perp}$  determine the magnitude of the in-plane and perpendicular torques, respectively.  $V$  is the applied voltage across the system.

To analyse the stability of the P and AP states as function of the applied field and bias voltage, we impose  $m_z = \mp 1$  and  $m_y, m_x \ll 1$ . Under these conditions, the projection of the Landau-Lifshitz-Gilbert equation on the  $x$ ,  $y$  and  $z$  axes yields the following system:

$$\begin{aligned} \dot{m}_x &= \mp \gamma a'_{\parallel} V m_x + \gamma \left( -\mu_0 H_a \pm \mu_0 H_{kz} - a'_{\perp} V^2 \right) m_y \pm \alpha \dot{m}_y \\ \dot{m}_y &= \gamma \left( +\mu_0 H_a \mp \mu_0 H_{kz} \pm \mu_0 H_{kx} + a'_{\perp} V^2 \right) m_x \mp \gamma a'_{\parallel} V m_y \mp \alpha \dot{m}_x \end{aligned} \quad (4.2)$$

Second order terms in  $m_x$ ,  $m_y$  and  $\alpha$  can be neglected due to the fact that  $m_x, m_y, \alpha \ll 1$ . By separating the variables ( $m_x$  and  $m_y$ ), we arrive at the following equation:

$$\ddot{m}_y - (A + D) \dot{m}_y + (AD - BC) m_y = 0, \quad (4.3)$$

where A, B, C and D are given by:

$$\begin{aligned} A &= \gamma \left( \pm \alpha \mu_0 H_a - \alpha \mu_0 H_{kz} \mp a'_{\parallel} V \pm \alpha a'_{\perp} V^2 + \alpha \mu_0 H_{kx} \right) \\ B &= \gamma \left( -\mu_0 H_a \pm \mu_0 H_{kz} - \alpha a'_{\parallel} V - a'_{\perp} V^2 \right) \\ C &= \gamma \left( +\mu_0 H_a \mp \mu_0 H_{kz} + \alpha a'_{\parallel} V + a'_{\perp} V^2 \pm \mu_0 H_{kx} \right) \\ D &= \gamma \left( \pm \alpha \mu_0 H_a - \alpha \mu_0 H_{kz} \mp a'_{\parallel} V \pm \alpha a'_{\perp} V^2 \right) \end{aligned} \quad (4.4)$$

The solutions of eq. (4.3) are of the type  $m_y = A^* \cdot e^{kt}$ . Replacing  $m_y$  in eq. (4.3) leads to the quadratic equation  $k^2 - (A + D)k + (AD - BC) = 0$ , which has the following discriminant:

$$\begin{aligned} \Delta &= -4\gamma^2 \left( \mu_0 (H_a \mp H_{kz}) + \alpha a'_{\parallel} V + a'_{\perp} V^2 \right) \\ &\quad \times \left( +\mu_0 (H_a \mp H_{kz}) + \alpha a'_{\parallel} V + a'_{\perp} V^2 \pm \mu_0 H_{kx} \right). \end{aligned} \quad (4.5)$$

The sign of this discriminant dictates whether the solutions are real or complex. For either state (P or AP), if the real part of  $k$  is positive,  $m_y$  grows in time and thus the initial state becomes unstable. The stability of the P and AP states is hence given by the following condition:  $Re(m_y) < 0$ .

We now examine the case for positive and negative discriminants. From eq. (4.5) we find that the discriminant is negative for the P state if

$$\mu_0 H_a < \mu_0 H_{kz} - \alpha a'_{\parallel} V - a'_{\perp} V^2 - \mu_0 H_{kx} \quad \text{or} \quad \mu_0 H_a > \mu_0 H_{kz} - \alpha a'_{\parallel} V - a'_{\perp} V^2. \quad (4.6)$$

For the AP state, the discriminant is negative for

$$\mu_0 H_a < -\mu_0 H_{kz} - \alpha a'_{\parallel} V - a'_{\perp} V^2 \quad \text{or} \quad \mu_0 H_a > -\mu_0 H_{kz} - \alpha a'_{\parallel} V - a'_{\perp} V^2 + \mu_0 H_{kx}. \quad (4.7)$$

Under these conditions, the two states P and AP are stable if the real part of  $k$  is negative, i.e. if

$$\gamma \left( \pm 2\alpha\mu_0 H_a - 2\alpha\mu_0 H_{kz} \mp 2a'_{\parallel} V \pm 2\alpha a'_{\perp} V^2 + \alpha\mu_0 H_{kx} \right) < 0. \quad (4.8)$$

Therefore, the P state is stable (with negative discriminant) within the field region set by eq. (4.6) and the voltage region  $V_1 > V > V_2$  given by

$$V_{1,2} = \frac{a'_{\parallel}}{2\alpha a'_{\perp}} \pm \sqrt{\left(\frac{a'_{\parallel}}{2\alpha a'_{\perp}}\right)^2 + \frac{\mu_0}{a'_{\perp}} \left(-H_a + H_{kz} - \frac{1}{2}H_{kx}\right)}. \quad (4.9)$$

Similarly, the AP state is stable (with negative discriminant) within the field region defined by eq. (4.7) and the voltage region  $V < V_2$  or  $V > V_1$ :

$$V_{1,2} = \frac{a'_{\parallel}}{2\alpha a'_{\perp}} \pm \sqrt{\left(\frac{a'_{\parallel}}{2\alpha a'_{\perp}}\right)^2 + \frac{\mu_0}{a'_{\perp}} \left(-H_a - H_{kz} + \frac{1}{2}H_{kx}\right)}. \quad (4.10)$$

Considering the order of magnitude of the parameters involved in eq. (4.9) and (4.10), for Fe/MgO/Fe MTJs, only one of the solutions of each equation is physically meaningful, namely  $V_2$  for both of them. They will be referred to in the following as  $V_{2P}$  and  $V_{2AP}$ .

For the P state, the discriminant is larger than zero when:

$$\mu_0 H_{kz} - \alpha a'_{\parallel} V - a'_{\perp} V^2 - \mu_0 H_{kx} < \mu_0 H_a < \mu_0 H_{kz} - \alpha a'_{\parallel} V - a'_{\perp} V^2, \quad (4.11)$$

and for the AP state if:

$$-\mu_0 H_{kz} - \alpha a'_{\parallel} V - a'_{\perp} V^2 < \mu_0 H_a < -\mu_0 H_{kz} - \alpha a'_{\parallel} V - a'_{\perp} V^2 + \mu_0 H_{kx}. \quad (4.12)$$

The additional condition that the solutions should be negative leads to:

$$\begin{aligned} \gamma^2 \left[ (1 + \alpha^2) (\mu_0 H_{kx})^2 - \left( 2 \left[ -\mu_0 H_a \pm \mu_0 H_{kz} - \alpha a'_{\parallel} V - a'_{\perp} V^2 \right] \mp \mu_0 H_{kx} \right)^2 \right. \\ \left. - \left( \pm 2\alpha\mu_0 H_a - 2\alpha\mu_0 H_{kz} \mp 2a'_{\parallel} V \pm 2\alpha a'_{\perp} V^2 + \alpha\mu_0 H_{kx} \right)^2 \right] < 0. \end{aligned} \quad (4.13)$$

Estimating and comparing the relative magnitude of the different terms for experimentally relevant values, this expression can be reduced to<sup>1</sup>:

$$-a'_{\perp}{}^2 V^4 + \left[ 2a'_{\perp} (-\mu_0 H_a \pm \mu_0 H_{kz}) \mp \mu_0 H_{kx} a'_{\perp} - a'_{\parallel}{}^2 \right] V^2 + \left[ -(-\mu_0 H_a \pm \mu_0 H_{kz})^2 + \mu_0 H_{kx} (\mp \mu_0 H_a + \mu_0 H_{kz}) \right] < 0. \quad (4.14)$$

Eq. (4.14) is a fourth degree equation in  $V$ , which can be reduced to a second degree equation by substituting  $V$  with  $V = \sqrt{W}$ . The solutions to these quadratic equations then give the final critical lines for the voltages for the case of the positive discriminant. The P state is stable for  $V > V_{1a}$  or  $V > V_{2a}$ , defined by

$$V_{1a} = +\sqrt{W_1}, V_{2a} = +\sqrt{W_2}, \quad (4.15)$$

whereas the AP state is stable if  $V < V_{2b}$  or  $V < V_{1b}$  according to:

$$V_{1b} = -\sqrt{W_1}, V_{2b} = -\sqrt{W_2}. \quad (4.16)$$

Here,

$$\begin{aligned} W_{1,2} &= \xi \pm \sqrt{\xi^2 + \kappa} \text{ with} \\ \xi &= \frac{1}{a'_{\perp}} (-\mu_0 H_a \pm \mu_0 H_{kz}) \mp \frac{\mu_0 H_{kx}}{2a'_{\perp}} - \frac{a'_{\parallel}{}^2}{2a'_{\perp}{}^2} \\ \kappa &= \frac{1}{a'_{\perp}{}^2} \left[ -(-\mu_0 H_a \pm \mu_0 H_{kz})^2 + \mu_0 H_{kx} (\mp \mu_0 H_a + \mu_0 H_{kz}) \right]. \end{aligned} \quad (4.17)$$

Equations 4.6, 4.7, 4.9, 4.10, 4.15 and 4.16 define the critical lines on the phase diagram as functions of the various parameters. These are plotted in figure 4.2 assuming the following values:  $a'_{\parallel} = 0.0067246$  T/V,  $a'_{\perp} = 0.0153707$  T/V<sup>2</sup> (taken from [75] using a film thickness of 1 nm),  $\mu_0 H_{kz} = 0.2$  T,  $\mu_0 H_{kx} = 0.04$  T and  $\alpha = 0.005$ .

In total, four types of regions are found in the phase diagram: one (each) where either only P or AP is stable, labeled P and AP respectively; a bistable region (P/AP) and finally two regions (shaded grey) where none of the states is stable.

Lines 1 and 2 correspond to the field dependent critical voltages. The AP state is stable in the region below line 1 (black, eq. (4.10)), the P state is stable in the region above line 2 (green, eq. (4.9)).

<sup>1</sup>Note that some additional solutions were excluded as they do not satisfy the condition of  $A+D < 0$ .



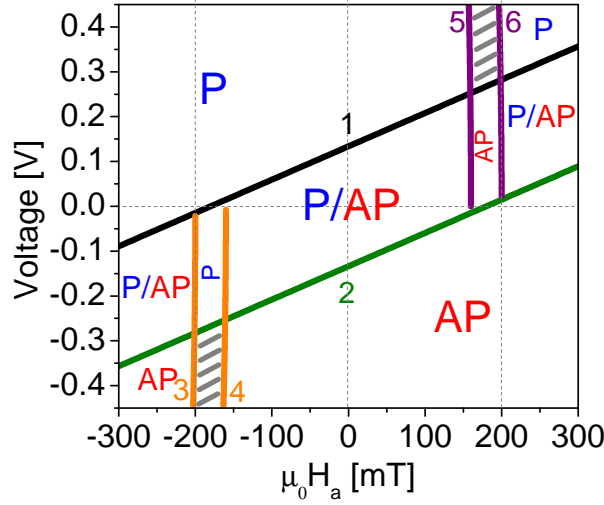


Figure 4.2: Analytically calculated phase diagram for the general case of an MTJ with two orthogonal anisotropy components  $\mu_0 H_{kx} = 0.04$  T and  $\mu_0 H_{kz} = 0.2$  T. P and AP denote to regions where the parallel and antiparallel states are stable, respectively. The dashed areas are regions where neither of the two states is stable.

These two lines are intersected by four lines, opening regions in the phase diagram in which the number of stable states is further reduced. The AP state is only stable outside of lines 3 and 4 (orange), which are defined by eq. (4.7). Additionally, for voltages below the critical line 2, AP is also stable for voltages smaller than those defined by eq. (4.16). Please note that these additional lines superimpose lines 3 and 4 in figure 4.2. The P state is stable outside of lines 5 and 6 (purple), which are defined by eq. (4.6). For voltages above line 1, P is also stable as given in eq. (4.15), the lines of which are superimposing lines 5 and 6 in the figure.

Lines 3 to 6 cross the horizontal axis at  $-\mu_0 H_{kz}$ ,  $-\mu_0 H_{kz} + \mu_0 H_{kx}$ ,  $\mu_0 H_{kz} - \mu_0 H_{kx}$  and  $\mu_0 H_{kz}$ . The opening up of the neither stable regions (grey-shaded areas) is therefore a direct result of the inclusion of  $\mu_0 H_{kx}$ .

Lines 1 and 2 in figure 4.2 are functions including a square root as given by  $V_{2P}$  in eq. (4.9) and  $V_{2AP}$  in eq. (4.10). The square-root-dependence is a signature of the perpendicular STT term. Indeed, for systems in which the field-like torque is negligible ( $a'_{\parallel} \gg a'_{\perp}$ ), lines 1 and 2 extrapolate to a linear dependence: The AP state is stable for voltages smaller than

$$V = -\frac{\alpha}{a'_{\parallel}} \left( -\mu_0 H_a - \mu_0 H_{kz} + \frac{1}{2} \mu_0 H_{kx} \right) \quad (4.18)$$

and P is stable for voltages larger than

$$V = -\frac{\alpha}{\alpha_{\parallel}} \left( -\mu_0 H_a + \mu_0 H_{kz} - \frac{1}{2} \mu_0 H_{kx} \right). \quad (4.19)$$

We directly compare the analytical solution with the numerical integration of the LLG equation. The Maple code used for the numerical integration was written by Dr. Volker Sluka. The calculations were carried out with the system set initially in the P or AP state, respectively. The results of the numerical simulation are shown in figure 4.3, using the same parameters as in the analytical phase diagram (figure 4.2). A combination of the two simulations in figure 4.3 yields an excellent agreement with the analytical solution.

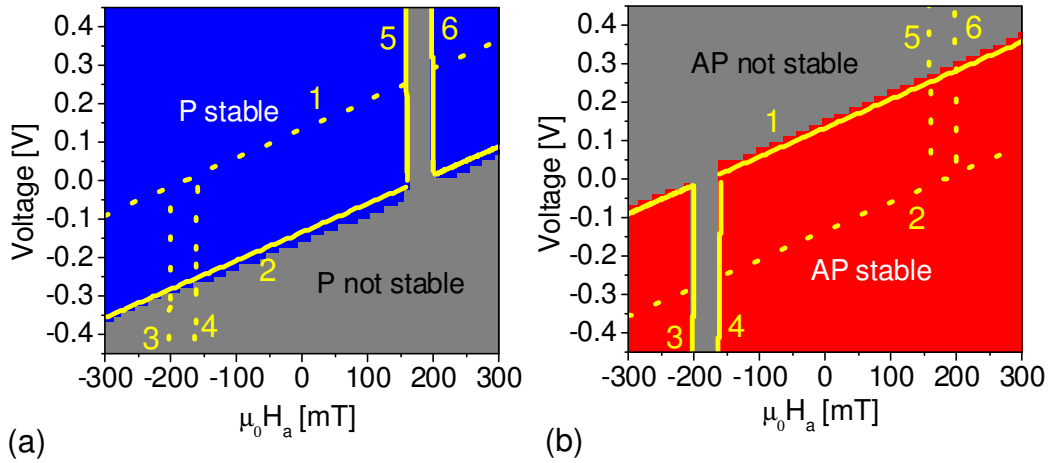


Figure 4.3: Numerically simulated phase diagram for general case starting from (a) P and (b) AP. The yellow lines are the analytical solutions.

### Special cases

By suitably defining the  $x$  and  $z$  axis of the coordinate system with respect to the plane of the layers, as well as the magnitude and sign of the two generalised anisotropies,  $\mu_0 H_{kx}$  and  $\mu_0 H_{kz}$ , the formalism described above can be applied to three different, experimentally relevant geometries:

1. A perpendicular MTJ with an additional in-plane easy axis (for example an elliptically shaped MTJ with perpendicular anisotropy). The  $x$  and  $z$  axes are defined as in the previous section and in figure 4.1, and both  $\mu_0 H_{kx} > 0$  and  $\mu_0 H_{kz} > 0$ .

2. A perpendicular anisotropy MTJ without in-plane shape anisotropy (for example a nanopillar with circular cross-section),  $\mu_0 H_{kx} = 0$  T. The only intrinsic field component is the effective out-of-plane anisotropy  $\mu_0 H_{kz}$ . The normal to the plane also defines the direction of the  $z$  axis. This is the highest symmetry case.
3. An in-plane magnetised MTJ with an in-plane shape anisotropy, such as a nanopillar with an elliptical cross-section. Here, the  $x$  axis is perpendicular to the plane of the film.  $\mu_0 H_{kx}$  is negative and represents the demagnetising field of the free layer, but might also include a perpendicular-to-the-plane anisotropy component, as long as it does not overcome the demagnetising field.  $z$  is the in-plane easy axis direction and  $\mu_0 H_{kz}$  is the easy axis (shape) anisotropy.

Note that in all three cases the reference layer and, hence, the current polarisation are defined as being oriented antiparallel to  $u_z$  as for the generalised geometry. The applied field  $\mu_0 H_a$  is along the  $z$  axis and a positive field favours the AP state, whereas for a positive voltage, the in-plane STT favours the P state.

#### 4.1.1.1 Limiting case 1: Perpendicular MTJ with additional in-plane anisotropy component

An MTJ with both the reference and the free layer magnetised out-of-plane and an additional in-plane shape anisotropy corresponds to the general case derived at the start of the chapter and represented in figure 4.1 as specified before.

The in-plane anisotropy component breaks the symmetry of the system as all other fields in the system as well as the current polarisation are perpendicular to the plane (along the  $z$  axis). This symmetry breaking is responsible for lines 3 to 6 in figure 4.2, opening up two regions, where only P (between lines 1 to 4) or AP (between lines 1, 2, 5 and 6) are stable, as well as two regions, where neither of the two states is stable (dashed grey).

Similar conclusions have been pointed out by Le Gall et al. who compared analytically calculated phase diagrams with experimental results on metallic layers with a perpendicular anisotropy and additional in-plane shape anisotropy [62]. The authors state that the differences in the analytical model and experimental results (see figure 2.13) might be induced by breaking of the uniaxial symmetry assumption of the analytical model used [62]. The regions where neither of the two states is stable are ascribed to steady magnetisation precessions around the perpendicular axis [62] or to canted

states of the magnetisation before the onset of precessional modes (obtained by micro-magnetic simulations by Mangin et al. [37]). It should be noted that there are further differences between our and the results by Mangin et al. and Le Gall et al. which are direct consequences of the different STT properties in MTJs and metallic structures as described in section 2.2.2. Indeed, for the metallic spin-valves, in addition to the field-like torque being negligible (which transforms lines 1 and 2 into linear functions on the field), the angular dependence of the in-plane STT introduces different slopes in these lines, which can therefore cross.

#### 4.1.1.2 Limiting case 2: Full perpendicular MTJ

As mentioned above, for this high symmetry case, lines 3 to 6 disappear. Indeed, when imposing  $\mu_0 H_{kx} = 0$ , the discriminant  $\Delta$  is found to be symmetric and always negative:

$$\Delta = -4\gamma^2 \left( \mu_0 H_a \mp \mu_0 H_{kz} + \alpha a'_{\parallel} V + a'_{\perp} V^2 \right)^2. \quad (4.20)$$

Therefore, the solutions to the differential equation are always complex and there is only one condition for the stability for each state. The P state is stable within the voltage region  $V_1 > V > V_2$  given by:

$$V_{1,2} = \frac{a'_{\parallel}}{2\alpha a'_{\perp}} \pm \sqrt{\left( \frac{a'_{\parallel}}{2\alpha a'_{\perp}} \right)^2 + \frac{\mu_0}{a'_{\perp}} (-H_a + H_{kz})}. \quad (4.21)$$

The AP state is stable for the voltage region  $V < V_2$  or  $V > V_1$ :

$$V_{1,2} = \frac{a'_{\parallel}}{2\alpha a'_{\perp}} \pm \sqrt{\left( \frac{a'_{\parallel}}{2\alpha a'_{\perp}} \right)^2 + \frac{\mu_0}{a'_{\perp}} (-H_a - H_{kz})}. \quad (4.22)$$

Similar to the general case, considering the order of magnitude of the parameters involved for Fe/MgO/Fe MTJs, only one of the solutions ( $V_2$  in both cases) of each equation is physically meaningful.

The phase diagram for a perpendicular anisotropy MTJ with circular cross-section is plotted in figure 4.4. Line 1 (corresponding to eq. (4.22)) and 2 (eq. (4.21)) separate two regions where either P or AP is stable with a bistable region in between. The P (AP) state is stable above (below) line 2 (1). In between we predict hysteretic behaviour as both configurations are allowed. Note that as the two lines do not cross over the experimentally relevant voltage and field range, neither canted states nor STT

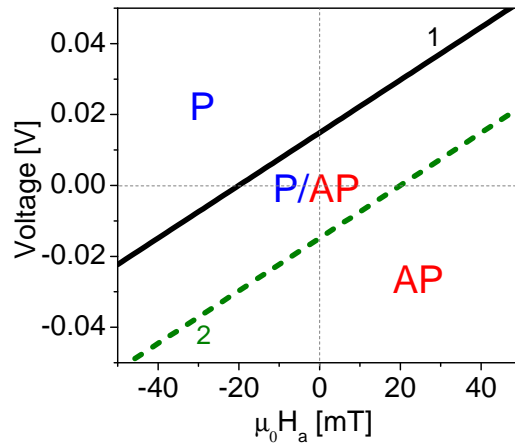


Figure 4.4: Analytically calculated switching phase diagram for fully perpendicular MTJ ( $\mu_0 H_{kx} = 0$  T) using  $a'_{\parallel} = 0.0067246$  T/V,  $a'_{\perp} = 0.0153707$  T/V<sup>2</sup> [75],  $\mu_0 H_{kz} = 0.02$  T and  $\alpha = 0.005$ .

driven precession are expected. This is confirmed by numerical integration, which is in excellent agreement with the analytical results as in the previous case. The comparison between the analytical calculation and the numerical integration is displayed in figure 4.5 using the same parameters as in the analytical phase diagram (figure 4.4).

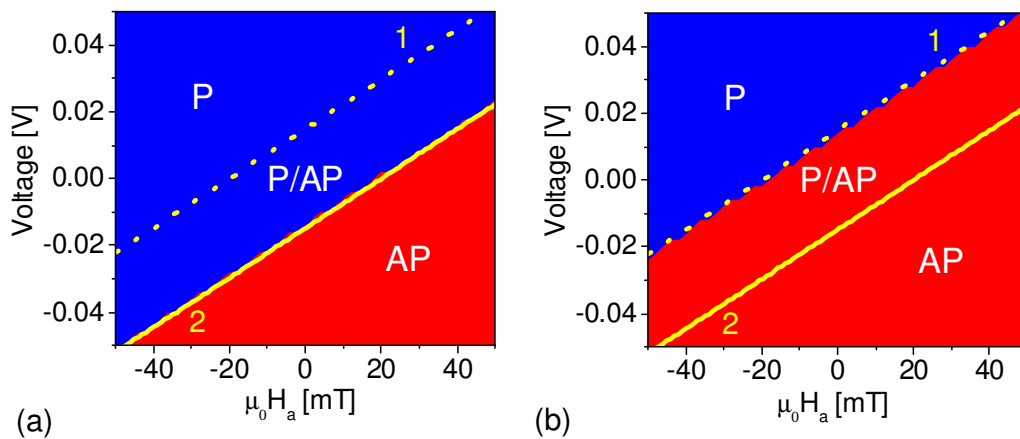


Figure 4.5: Numerically simulated phase diagram for fully perpendicular MTJs ( $\mu_0 H_{kx} = 0$  T) starting from (a) P and (b) AP. No additional regions compared to the analytical solution were obtained.

#### 4.1.1.3 Limiting case 3: Fully in-plane MTJ

The generalised formulae can also be used to describe MgO-MTJs with both the reference and the free layer magnetised along an in-plane easy axis, by rotating the sample

by  $90^\circ$ , as depicted in figure 4.6 (b), and imposing  $\mu_0 H_{kx} < 0$  to account for the effective demagnetising field. As in cases 1 and 2, the external field is applied along the  $z$  axis and a positive field favours the AP state. The polarisation remains  $\vec{p} \parallel -\vec{u}_z$ , so that positive voltage favours the P state. This configuration is especially relevant as a considerable number of experimental results published so far have been carried out on in-plane MgO-MTJs with elliptical cross-section.

For this particular geometry the critical lines are defined as follows: The P state is stable for voltages larger than

$$V = \frac{a'_{\parallel}}{2\alpha a'_{\perp}} - \sqrt{\left(\frac{a'_{\parallel}}{2\alpha a'_{\perp}}\right)^2 + \frac{\mu_0}{a'_{\perp}} \left(-H_a + H_{kz} - \frac{1}{2}H_{kx}\right)}, \quad (4.23)$$

whereas the AP state is stable for voltages smaller than

$$V = \frac{a'_{\parallel}}{2\alpha a'_{\perp}} - \sqrt{\left(\frac{a'_{\parallel}}{2\alpha a'_{\perp}}\right)^2 + \frac{\mu_0}{a'_{\perp}} \left(-H_a - H_{kz} + \frac{1}{2}H_{kx}\right)}. \quad (4.24)$$

Additionally, the following magnetic field conditions have to be fulfilled: The P state is stable for

$$\mu_0 H_a < \mu_0 H_{kz} - \alpha a'_{\parallel} V - a'_{\perp} V^2, \quad (4.25)$$

and the AP state is stable for

$$\mu_0 H_a > -\mu_0 H_{kz} - \alpha a'_{\parallel} V - a'_{\perp} V^2. \quad (4.26)$$

Note that in general  $\alpha a'_{\parallel} V \ll a'_{\perp} V^2$  and can be neglected. The additional solutions derived for the case of a positive discriminant (eq. (4.15) and (4.16) in the general calculation) are neglected here since they are congruent with eq. (4.25) and (4.26) for the experimentally relevant region and magnitude of parameters.

Figure 4.6 displays the coordinate system and the calculated analytical phase diagram for the in-plane case using  $a'_{\parallel} = 0.0067246$  T/V,  $a'_{\perp} = 0.0153707$  T/V<sup>2</sup> [75],  $\mu_0 H_{kx} = -2.15$  T,  $\mu_0 H_{kz} = 0.02$  T,  $\alpha = 0.005$  [90]. Compared to the analytical diagram for the generalised case (figure 4.2), only four critical lines remain, mainly because  $\mu_0 H_{kx}$  is orders of magnitude larger than the other fields in the system. Indeed, since  $\mu_0 H_{kx}$  determines the width of the regions opening up due to the symmetry breaking, lines 4 and 5 are shifted to an experimentally not relevant field range for this geometry

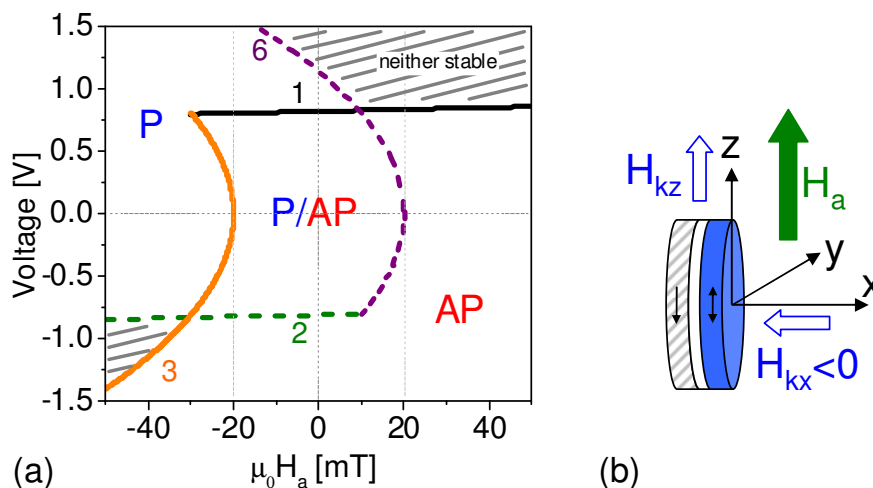


Figure 4.6: Switching phase diagrams for the case of in-plane magnetic tunnel junctions: (a) Analytical solution, (b) schematic of the coordinate system.

(above  $\pm 2$  T).

The AP state is stable within the borders defined by lines 1 (black, eq. (4.24)) and 3 (orange, eq. (4.26)), whereas the P state is stable in the region enclosed by the critical lines 2 (green, eq. (4.23)) and 6 (purple, eq. (4.25)).

Similar to the generalised case, there are four types of regions: one (each) where only P or AP is stable, a bistable region and two neither stable regions at high field and voltage values, which favour opposite states. Several important aspects can be derived from the phase diagram:

The curvature of the critical lines 3 and 6 is a consequence of the quadratic bias-dependence of the perpendicular STT, as can be seen in the corresponding eq. (4.26) and (4.25). This implies that the bias-dependence of the field-like STT can be directly determined by fitting these lines on experimentally obtained phase diagrams with eq. (4.25) and (4.26).

Both lines 3 and 6 curve to the left, reflecting the assumption that the field-like torque always favours the AP state. This will have consequences for experimental magnetoresistance curves at constant voltage (horizontal scans in the phase diagram). A hysteresis loop at  $V = 0$  yields the anisotropy value of the magnetic free layer, as the horizontal cross section through  $V = 0$  crosses lines 3 and 6 at  $-\mu_0 H_{kz}$  and  $+\mu_0 H_{kz}$ . If the voltage is increased, both switching fields shift to the left for both voltage polarities, but the width of the loop remains twice the anisotropy. Indeed, as the field-like torque favours the AP state, it will assist the external field for switching to the AP state and

oppose it for the AP to P reversal. Switching to the AP state will thus require less field to be applied, while the field necessary to induce the opposite transition will be increased in the presence of a finite bias voltage.

The square-root-dependence of lines 1 and 2 is also a consequence of the perpendicular STT. As mentioned previously, the two lines extrapolate to a linear dependence for the assumption of a negligible perpendicular STT ( $a'_{\parallel} \gg a'_{\perp}$ ).

The analytical calculation demonstrates that the critical lines intersect each other at fields and voltages which depend on the characteristics of the device (such as the anisotropy), rather than on the field and voltage axis. Using one fitting formula for each quadrant of the phase diagram, such as described by Oh et al. [10], is thus incorrect.

We also carried out numerical calculations for the in-plane MTJ configuration using a Maple code. The results with the system set initially in the P or AP state are shown in figures 4.7 (a) and (b), respectively. The switching borders agree very well with the

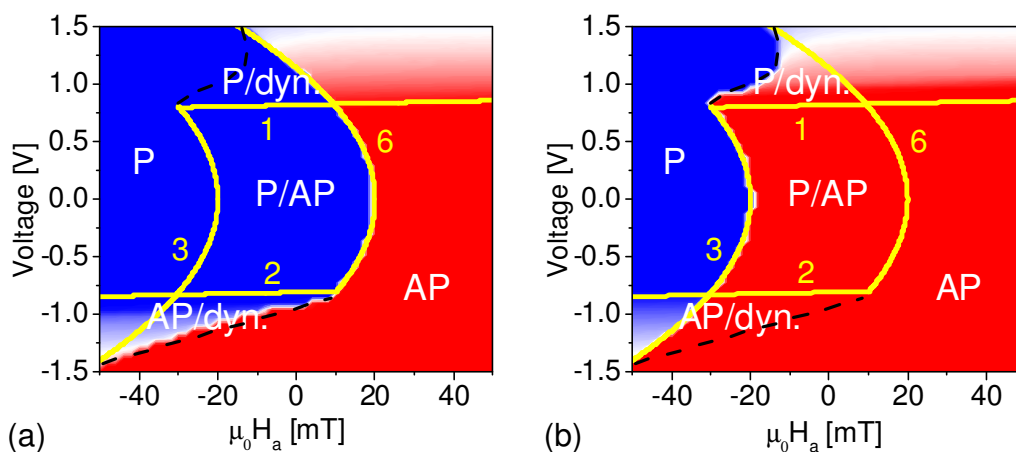


Figure 4.7: Switching phase diagrams for in-plane magnetic tunnel junctions, numerical simulations starting from (a) P and (b) AP. The yellow lines are the analytical solutions. The dotted lines are guides for the eye marking the bistable stable state/clamshell precession areas. White color marks intermediate resistance values. The values used are  $a'_{\parallel} = 0.0067246$  T/V,  $a'_{\perp} = 0.0153707$  T/V<sup>2</sup>,  $\mu_0 H_{kx} = -2.15$  T,  $\mu_0 H_{kz} = 0.02$  T and  $\alpha = 0.005$

analytical solution (yellow lines). Two additional bistable regions (P/dyn and AP/dyn) are obtained by numerical integration. In these additional regions, the magnetisation of the free layer can be either in a stable state (P or AP), or perform steady-state precession on a clamshell trajectory around the opposite state (AP or P, respectively). The opening of the clamshell trajectory along the  $x$  axis is low, reflecting the large demagnetising field pushing the magnetisation towards the plane of the layer. The two regions can not



be obtained analytically by the method presented here, as this approach only determines the critical lines where either P or AP become unstable and the borders of the two additional regions appearing on the numerical phase diagram correspond to switching from a dynamical state.

These regions have also been observed in GMR devices [28], and are not specific for MTJs. In a simulation where  $a'_{\perp} = 0$ , the curvature of lines 3 and 6 disappears but the bistable clamshell precession/static state regions remain. This can be seen in figure 4.8.

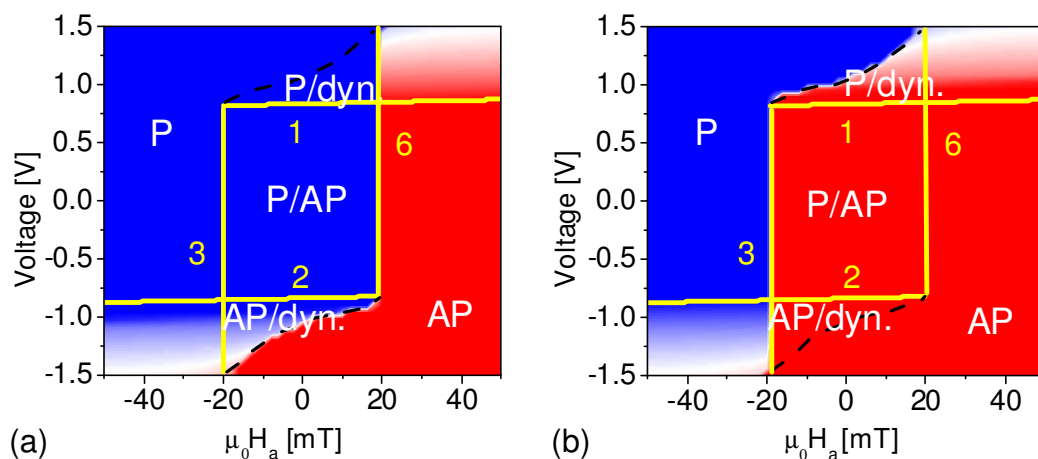


Figure 4.8: Switching phase diagrams for in-plane magnetic tunnel junctions, numerical simulations calculated without perpendicular STT starting from (a) P and (b) AP. The yellow lines are the analytical solutions. The dotted lines are guides for the eye marking the bistable stable state/clamshell precession areas. The values used are  $\mu_0 H_{kz} = 0.02$  T,  $\mu_0 H_{kx} = -2.15$  T,  $\alpha = 0.005$  and  $a'_{\parallel} = 0.00656$  T/V.

The curvature of lines 3 and 6 can potentially lead to back-hopping, especially in an off-pulse measurement. A resistance versus voltage curve taken at constant field corresponds to a vertical scan on the phase diagram. Such an example is depicted in figure 4.9. Starting with the sample in the P state, as the voltage is decreased, this state will remain stable until reaching line 2, above which, only the AP state is allowed. Point 1 on figure 4.9 marks the P to AP transition. Larger negative bias will not induce further switching events as no other critical lines can be crossed beyond this point. When scanning the voltage from negative to positive values, the free layer magnetisation will remain in the AP configuration, until crossing line 1, with point 2 on figure 4.9 marking the AP to P state transition. At higher positive voltages, the P state remains stable until crossing line 6, beyond which neither of the two states is allowed (point 3). Experiments, as well as numerical studies indicate that in this region, two

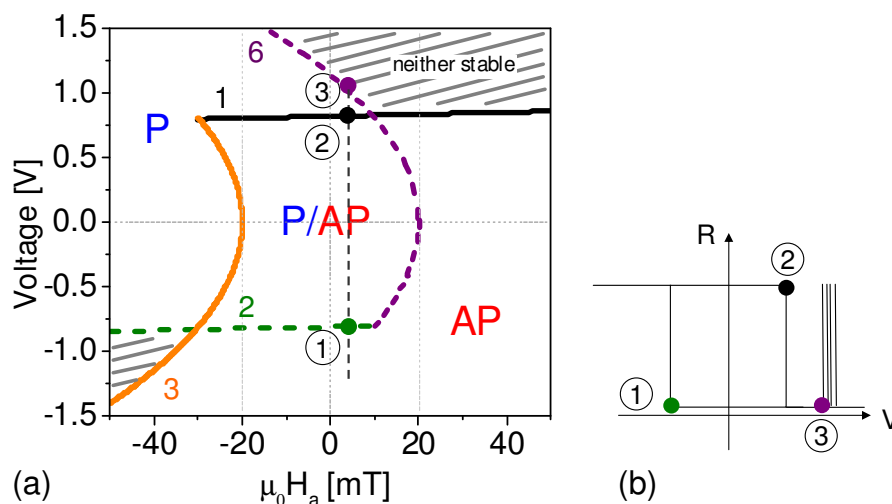


Figure 4.9: Schematic of one possible origin for the back-hopping phenomenon in in-plane magnetised MTJs. (a) Analytically calculated phase diagram of an in-plane MTJ with an indicated R-V sweep at low magnetic field (around 5 mT), (b) schematic of the equivalent R-V measurement with back-hopping events at voltages corresponding to the 'neither stable' region in the phase diagram.

types of steady-state precession can be excited (clamshell precession around the  $z$  axis or circular precession around the demagnetising field), depending on the magnitude of the voltage and the field applied [28]. Steady-state precession around  $x$  would appear as 'back-hopping' on a off-pulse resistance measurement. Indeed, steady-state precession is only maintained as long as the bias is applied and after the pulse the magnetisation has an equal probability for relaxing towards either P or AP state from an out-of-plane trajectory. Note that from the analytical phase diagram, at one given applied field, back-hopping after a hysteresis is only expected for positive voltage if the perpendicular STT has a quadratic bias-dependence favouring the AP state. Moreover, in the absence of a finite field-like torque, the curvature of line 6 disappears (as discussed previously) and crossing this line after the sample has switched to the P state is no longer possible. This implies that this type of back-hopping is intrinsic to MTJs, and does not require thermal activation. Other thermally excited mechanisms remain possible. Indeed, at finite temperature the free layer has a non-zero probability to hop between different states within the voltage-field-ranges which correspond to bistable regions on the phase diagram. For example, in the P/dyn and AP/dyn areas, telegraph-noise like behaviour may be observed between a static and dynamic state, which corresponds to an intermediate static resistance level (as a result of precessional motion).

#### 4.1.1.4 Summary

The critical switching voltages and switching fields of MTJs were calculated including both the in-plane and the perpendicular STT, for a generalised case of two orthogonal anisotropy directions. The symmetry breaking due to an additional in-plane anisotropy component for fully perpendicular MTJs can explain experimental results reported by several groups [37, 62, 91]. For in-plane magnetised MTJs, the perpendicular STT may induce back-hopping, even at 0 K, and its magnitude can be obtained by fitting lines 3 and 6 on experimentally obtained phase diagrams. Knowing the bias-dependence of the field-like STT, the in-plane component can be determined by fitting lines 1 and 2, if the material parameters are known. Results for this approach, as well as an additional method (TE-FMR) for determining the STT bias-dependence, are described in the next sections of this chapter.

### 4.1.2 Experimental phase diagrams

#### 4.1.2.1 DC Phase diagram

A quick and straightforward way to obtain information about the switching characteristics is to measure the DC switching properties. This can either be done by detecting the resistance while sweeping the field and keeping the applied voltage constant (MR or R-H curve), or by sweeping the voltage at a constant field (R-V curve). If the obtained switching fields and voltages are displayed together, both methods will yield a consistent phase diagram. However, some critical lines of the phase diagram might only be accessible by one method.

Figure 4.10 (a) displays a typical MR loop measured with an applied bias of 1 mV (at least two orders of magnitude below the switching voltage), as well as a series of MR curves measured at applied voltages between +0.6 V and -0.6 V. The resistance of the sample in the P state is 1035  $\Omega$ , the TMR ratio is 72 % and the coercivity is 1.8 mT. The hysteresis loop is shifted towards the negative fields by 1.1 mT. The shift (favouring the AP state) is the result of Néel coupling through barrier roughness and dipolar coupling from the reference layer. If an additional positive bias (with the in-plane STT favouring the P state) is applied, switching towards P occurs at smaller (negative) magnetic fields. The P to AP transition does not shift significantly at first, but above 0.2 V, the corresponding switching fields start to shift towards lower values. At 0.6 V, the hysteretic behaviour is completely suppressed and the transition between

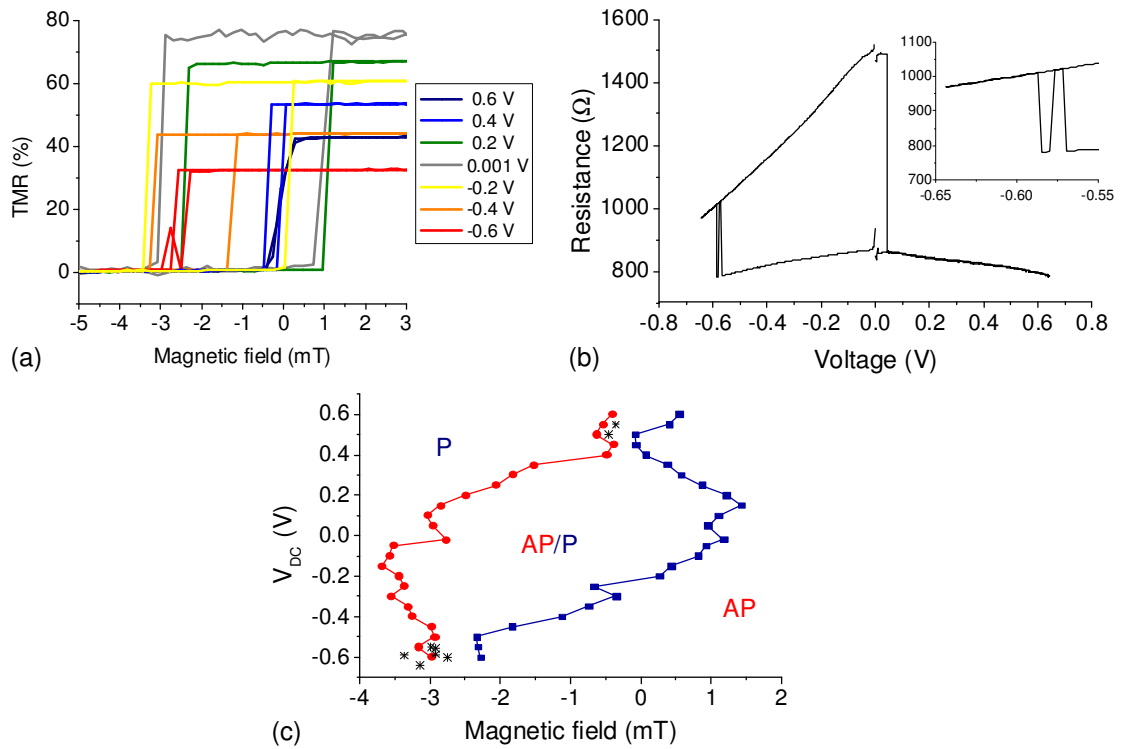


Figure 4.10: (a) Magnetoresistance curves of sample 5 for different constant DC voltage biases and (b) R-V loop at constant field of -2.7 mT, the inset zooms into the area with the back-hopping events for large negative voltages. Measurements were performed with assistance from Dr. Ciarán Fowley. (c) The obtained phase diagram from the R-H loops shows regions where P, AP or both states are stable. The black stars indicate the occurrence of instabilities in the resistance values in the R-H or R-V curves (back-hopping).

the two states becomes reversible. For the case of negative applied voltages (with the in-plane STT favouring the AP state), the switching fields towards the AP state are reduced; the hysteresis is almost suppressed at an applied bias of -0.6 V. Depending on the applied voltage, back-hopping can be observed either from the P or the AP state. An example can be seen in the MR loop at -0.6 V in figure 4.10 (a) (red curve).

Figure 4.10 (b) presents an R-V loop measured with an applied field of -2.7 mT. The bias-dependence of the resistance of the AP state (and thus the TMR) with increasing bias voltage, also obvious in figure 4.10 (a), is a well known phenomenon for MTJs, although the responsible mechanisms are still discussed. Possible reasons include the bias-dependent electronic band structure of the magnetic electrodes [41] or an increase in defect-state-assisted tunneling at elevated bias [40].

The curve in figure 4.10 (b) exhibits back-hopping from the AP state for biases

above  $-0.55$  V. A similar behaviour was observed up to  $-3.4$  mT. Back-hopping occurred both for increasing and decreasing voltage values. For fields below  $-3.4$  mT, the AP state is stable and neither current-induced switching nor back-hopping were observed.

The phase diagram extracted from the R-H curves can be seen in figure 4.10 (c). It shows the stability regions for P and AP as function of the applied magnetic field and DC voltage. The critical switching fields were extracted from each R-H loop as the largest (lowest) field value for which the P (AP) state was still stable. The critical switching voltages, as extracted from R-V loops, agree well. The black stars mark the onset of back-hopping.

Compared to the analytical phase diagram for in-plane MTJs, described in paragraph 4.1.1.3, the experimental DC phase diagram exhibits the following differences:

- There is no clear separation between line 1 and 3 and between 2 and 6, respectively. The corners corresponding to their intersection are rounded.
- The bending of lines 3 and 6 is different from the theoretical calculation: Both lines are bent outwards and the coercivity is decreased for larger bias voltages (possibly due to Joule heating).
- Back-hopping after hysteresis is observed for both voltage polarities, while in theory this is only possible for positive voltages.

We attribute the differences in the shape of the phase diagram mostly to thermal activation, which is not taken into account in the analytical calculation. Both magnetic field- and current-induced magnetisation switching are thermally activated processes at room temperature, especially for DC measurements. Indeed, the measurement time is of the order of ms, orders of magnitude larger than the characteristic time for thermally activated reversal, which is about 1 ns. In order to reduce the impact of this effect on the phase diagram, switching induced by voltage pulses in the ns-range was investigated and will be discussed in the next section.

#### 4.1.2.2 Off-pulse measurement of phase diagram

Figure 4.11 presents a series of phase diagrams measured on a similar sample for different voltage pulse lengths. The state of the sample was detected off-pulse, i.e. by measuring the DC resistance after the pulse had been applied with a probe current well below the switching value ( $10 \mu\text{A}$ ). These phase diagrams were obtained by averaging the resistance of the sample when switching from the P and AP state, for each value of

the applied field and voltage pulse magnitude. The original LabView programme was written by Dr. Huadong Gan, a visiting scientist in our group. All later changes after Dr. Gan's stay were implemented by myself. These results exhibit clear differences

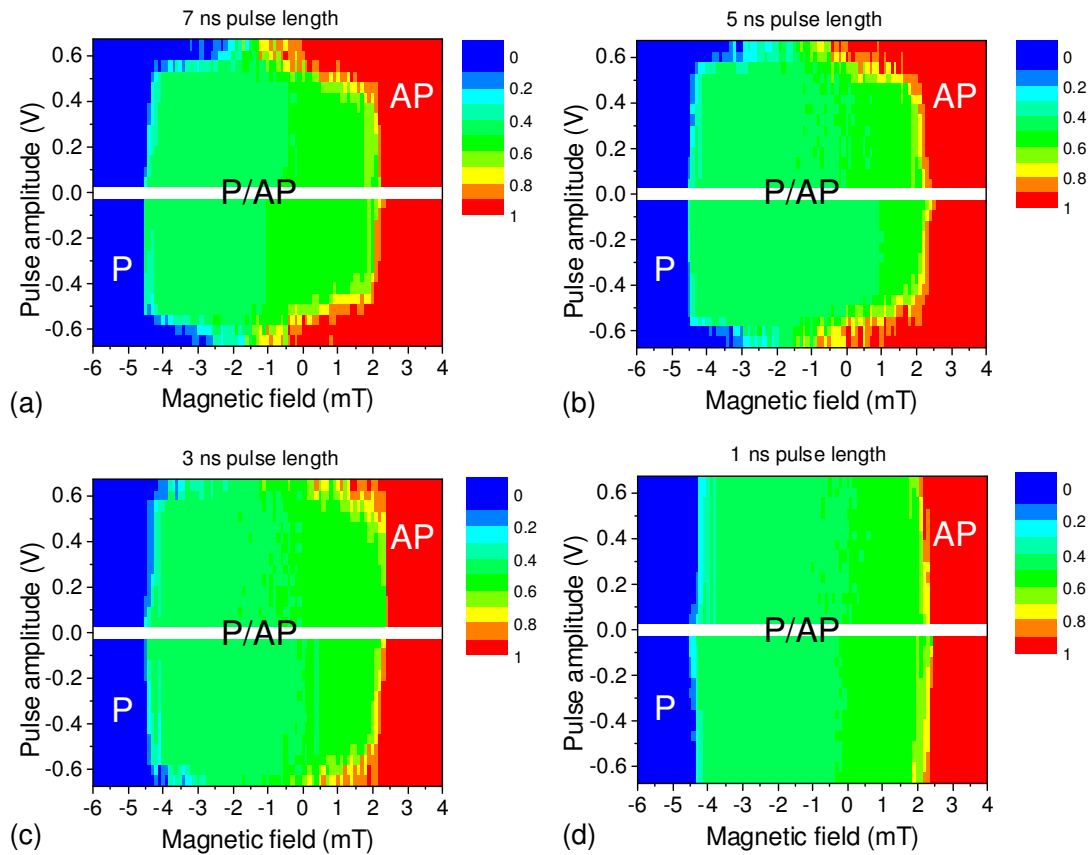


Figure 4.11: Switching phase diagrams for sample 2 in an off-pulse measurement for different pulse lengths: (a) 7 ns, (b) 5 ns, (c) 3 ns and (d) 1 ns. Shown is the average of two measurements (from P and AP). Red corresponds to the AP state, blue to the P state. The measurements were performed by Wen Feng, a summer student. The field stepsize was 0.1 mT, the voltage stepsize was 50 mV.

compared to the DC phase diagram in fig. 4.10. For the phase diagrams measured with 3, 5 and 7 ns pulse lengths, the borders marking the stability of the P and AP state, respectively, have two inflection points each (at approximately  $\pm 0.5$  V). As the pulse length is reduced, the pulse amplitude required to induce reversal increases, and at 1 ns, switching by voltage can no longer be achieved in the investigated range of voltage pulse amplitudes. For pulses longer than 1 ns, thermal activation still plays a role, as evidenced by the fact that switching is non-deterministic at high voltage amplitudes (speckled areas in the phase diagrams in figure 4.11 (a)-(c)). Assuming that the low voltage (meaning in-between the two inflection points) parts of the borderlines,

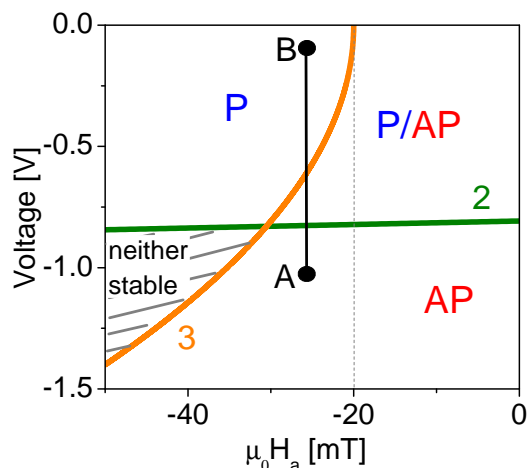


Figure 4.12: Schematic of the artefact in the off-pulse measurements for in-plane magnetised samples at fields higher than the anisotropy and negative voltages. The black points mark the voltages at which the DC resistance is probed (point B) and at which the pulse is applied (A).

marking the stability of the P and AP state, correspond to lines 6 and 3, respectively, the speckled areas can be associated with thermal activation either in the P/AP bistable region, or in one of the P/dyn or AP/dyn regions in figure 4.7.

While the low voltage part of the border marking the stability of the P state exhibits a slight curvature, this is absent on the border marking the AP to P switching. This is caused by an artefact in off-pulse measurements. Switching events are not detectable if the state after the switching is not stable in the phase diagram region where the resistance is probed (close to  $V = 0$ ). This is schematically shown in figure 4.12. For magnetic fields below line 3, the sample will switch to the AP state at voltages amplitudes below line 2, such as point A on the figure. However, the resistance of the sample is probed after the pulse, at low voltages, where the only stable state is the P state (e.g.  $10 \mu\text{A}$ , point B). The same argument applies for the regions where neither state is stable. There, only the states which are stable at low voltage bias will be detected by the measurement. Back-hopping will also only be detected for fields below the coercivity.

Nevertheless, it should still be possible to determine the bias-dependence of the perpendicular STT parameter  $a'_{\perp}$  by fitting the low voltage part of the P to AP switching border identified as line 6, which is not influenced by the off-pulse method. However, before attempting the fit, the measurement procedure used to obtain the phase diagrams in figure 4.11 was improved as follows:

- When setting the magnetic field, the Kepco power supply overshoots and causes a corresponding overshoot of the magnetic field with a magnitude of about half of the step size. For the data presented in figure 4.11, the magnetic field steps to and away from the saturation field and the associated overshoot were set to be large (1 mT and 0.5 mT, respectively) compared to the interval between the data points (0.1 mT). For all further measurements, the step size from saturation to the desired field value was set so that the overshoot was approximately half of the interval between the data points in order not to introduce additional errors in the measurement.
- The initial programme increased the voltage amplitudes in equidistant steps, not taking into account that the generator steps the output signal in dB. This induced large deviations between the set and the applied voltage amplitudes, especially at large bias. For instance, when setting 0.6 or 0.65 V in the programme, the actual applied voltage was 0.65 V in both cases. For all further measurements, these 'not-available' voltage values were excluded from a voltage amplitude list that was sent to the pulse generator.

A phase diagram with the improved measurement procedure can be seen in figure 4.13. A clear difference to figure 4.11 (d) are the differentiated switching fields in the phase diagram. Since the field stepping was reduced, the broader distribution of the switching fields caused by thermal activation is now observable.

The pulse length was 1 ns and the maximum voltage amplitude applied was 1 V. Higher voltages could not be addressed, since the breakdown voltage at this pulse length was determined as 1.1 V. As in the previous cases, the experiment was carried out twice: starting from P (figure 4.13 (a)) and from AP (4.13 (b)). Figure 4.13 (d) displays the average resistance values calculated from the data of the two measurements. Unlike on the phase diagrams in figure 4.11 (a)-(c), the borderlines marking the stability of each state of figure 4.13 (d), exhibit only one inflection point, as expected from the theoretical model. We associate the part of the transition to the AP (P) state above approximately -0.75 V (below 0.75 V) with line 6 (3) and the parts between -0.75 V and -1 V (0.75 V and 1 V) with line 2 (1).

In order to extract the bias-dependence of the perpendicular STT term, we analyse the part of the phase diagram associated with line 6 and fit the data according to equation (4.25), taking into account the experimentally determined coercivity of the sample. This is shown in figure 4.14. For each pulse amplitude, the P to AP switching



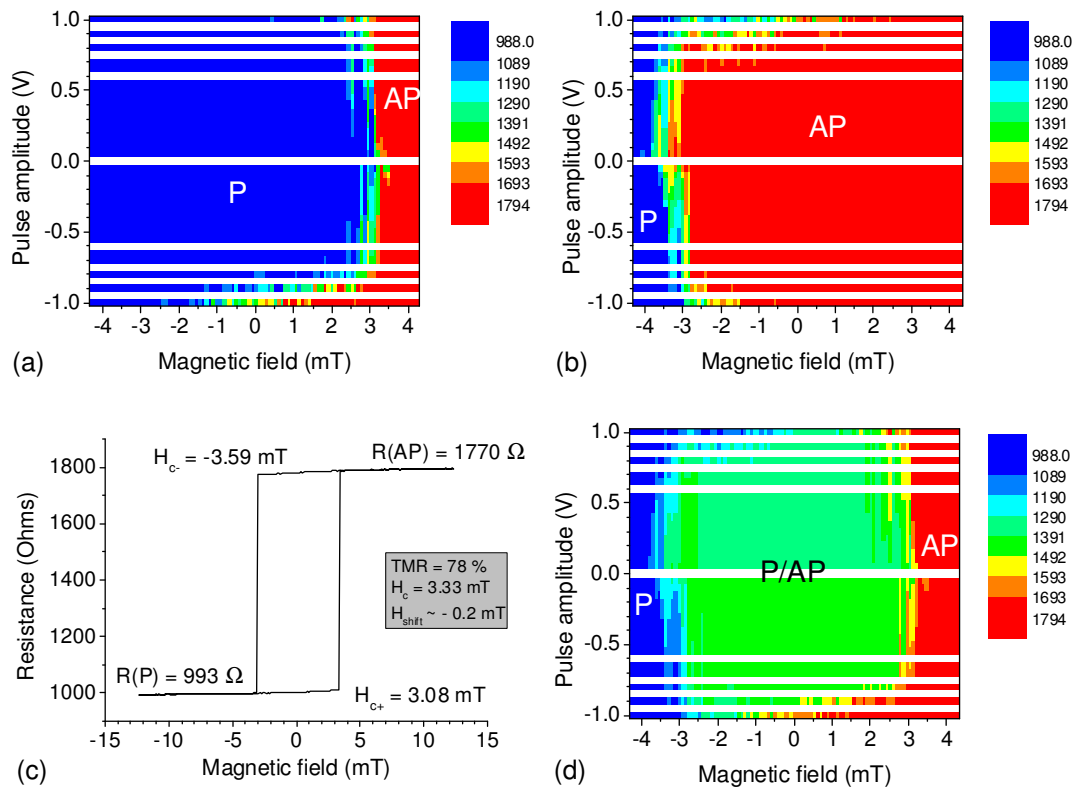


Figure 4.13: Experimentally obtained switching phase diagrams for sample 3 in an off-pulse measurement. The applied magnetic field was in the plane of the sample. The colour code shows the resistance of the sample after the pulse (off-pulse) (a) from P, (b) from AP state, and (d) on average. (c) shows a magnetic hysteresis curve of the same sample at a current of  $10 \mu\text{A}$ . The field step size was  $0.09$  mT, the voltage stepsize was  $50$  mV when available.

field had to be extracted from the experiment. This was defined as the lowest field value for which the resistance was still within  $90\%$  of the AP resistance, as shown in figure 4.14 (a). The resistance changes between P and AP through intermediate resistance levels. This was the combined result of averaging over ten measurements and thermal fluctuations in the switching field (since the field was not pulsed).

In figure 4.14 (b) the switching fields such determined for the different pulse amplitudes are shown. A parabolic fit of the data (excluding two values at the highest negative voltage amplitudes) yields the following value for the perpendicular STT bias-dependence:  $a'_{\perp} = 0.5$  mT/V<sup>2</sup>. The small linear component in the fit might be an artefact (related to the error bar in setting the voltage and/or field value) or stem from an asymmetry in the MTJ.

In the next paragraph, we discuss real-time on-pulse measurements which should bring about the following advantages:

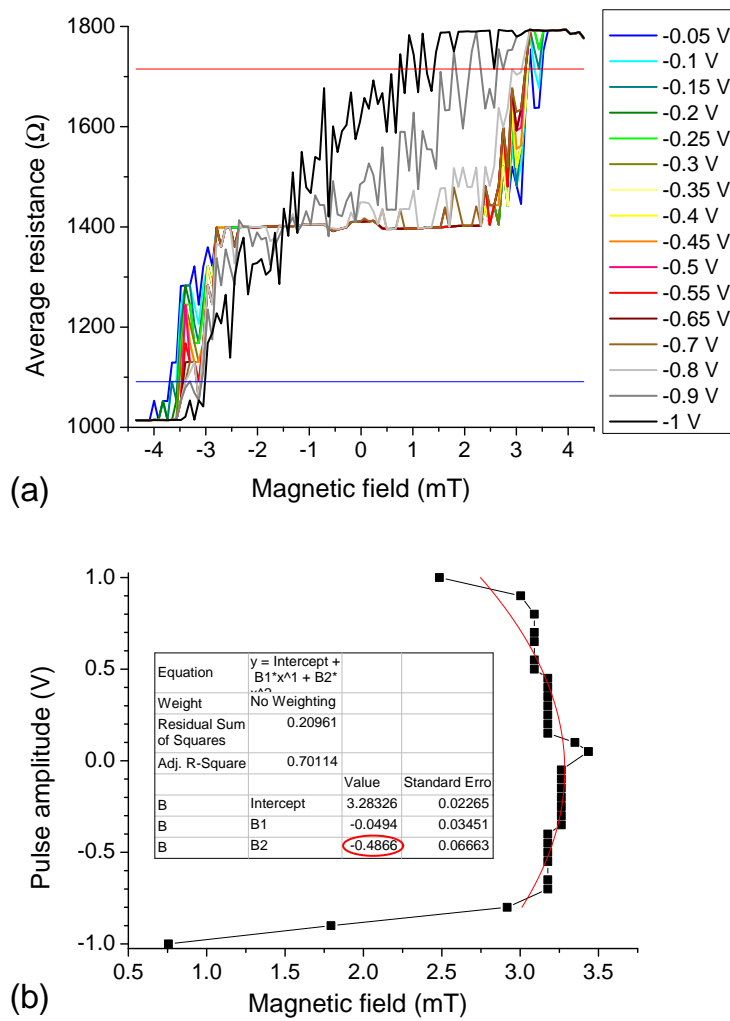


Figure 4.14: Determination of  $a_{\perp}'$  from the off-pulse phase diagram. (a) The smallest magnetic field value where the AP state is still stable is determined as being within 90 % of the resistance in the AP state. Shown are resistance vs. magnetic field loops for negative pulse amplitudes of figure 4.13 (c). (b) The determined field values are fitted with a parabolic formula to yield the perpendicular STT parameter (highlighted in red circle).

- An off-pulse measurement does not allow line 3 to be determined experimentally, but this is expected to appear on an on-pulse measurement.
- A direct observation of the switching event is only possible through an on-pulse measurement. The switching time can thus be determined and the evolution of the resistance during the switching event, correlated with the trajectory during reversal, can be investigated.

### 4.1.2.3 On-pulse measurement of phase diagram (single shot)

On- and off-pulse experiments were carried out simultaneously. The real-time on-pulse measurement method was described in detail in section 3.3.2. Specifically, nanosecond voltage pulses were applied to the device and the reflected signals were recorded using a 20 GHz real-time oscilloscope.

Figures 4.15 (a), (c) and (e) present three examples of traces measured at  $-0.02$  mT,  $+4.21$  mT and  $-1.58$  mT, respectively, for a pulse amplitude of 1 V (green), applied to the same device as discussed in the previous paragraph. For comparison, on each of the three figures, the traces corresponding to the reference signals measured in the P or AP saturated state are shown in blue and red, respectively. In the case of figure 4.15 (a) and (c), the sample remains in the P and AP state during the pulse, respectively. Figure 4.15 (e) shows a typical example of a switching event. The sample stays in the AP state for the first approximately 0.4 ns of the pulse. After 0.4 ns, the recorded signal starts to deviate from the reference trace corresponding to the AP state, until it finally settles at the P state level at around 0.65 ns.

Given that the signal-to-noise ratio in this experiment is rather low, further data processing was required in order to reduce errors introduced by experimental artefacts, such as jitter. The start/end state of the sample was defined by comparing the measured signal with the reference traces for the P and AP state. Figures 4.15 (b), (d) and (f) show the difference signals at each point in time between the AP reference and the actual measurement (in red), and the measurement and the P reference trace (in blue), for the same values of the applied field and voltage amplitude as in the corresponding figure on the left. In order to identify the state of the device at the start of the pulse, each of these two signals was then integrated between 0.22 and 0.42 ns (as explained in section 3.3.2.6). The sample state was defined by the integral yielding the lowest value. A similar analysis was performed for the end state with the integrals being calculated between 0.72 and 0.92 ns.

Based on this method of processing the signals, there are several options for constructing the phase diagram. The results obtained through each approach are shown in figures 4.16 and 4.17 for the case of the sample initially being saturated in the P and AP state, respectively. The straight-forward option is to plot the probability that a given configuration (P or AP) represents the end state of the device (Figure 4.16 (b) and figure 4.17 (b)). However, the set field is applied over a period of several seconds before the beginning of the pulse. During this time, the device is still subjected to ther-

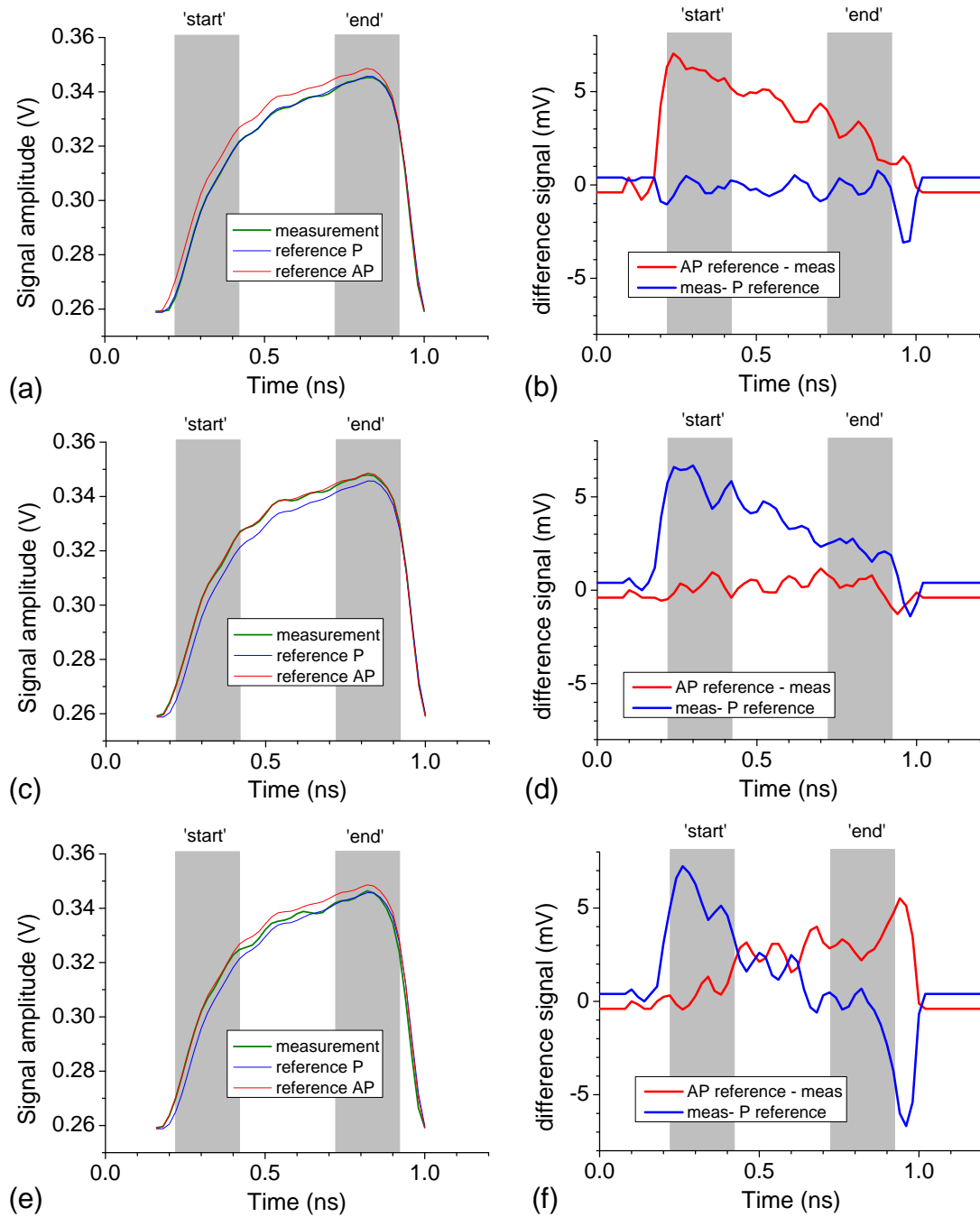


Figure 4.15: Examples for the automated analysis of the on-pulse measurement of sample 3: (a), (c), and (e) signal amplitudes and (b), (d), and (f) difference signals to the reference signals. In (a) and (b) there was no switching from the P state (at  $-0.02$  mT), in (c) and (d) no switching from the AP state (at  $+4.21$  mT), whereas (e) and (f) show a switching event from AP to P (at  $-1.58$  mT). All pulses favoured the P state and had an amplitude of 1 V.

mal activation. This is clearly demonstrated by the fact that the coercivity determined

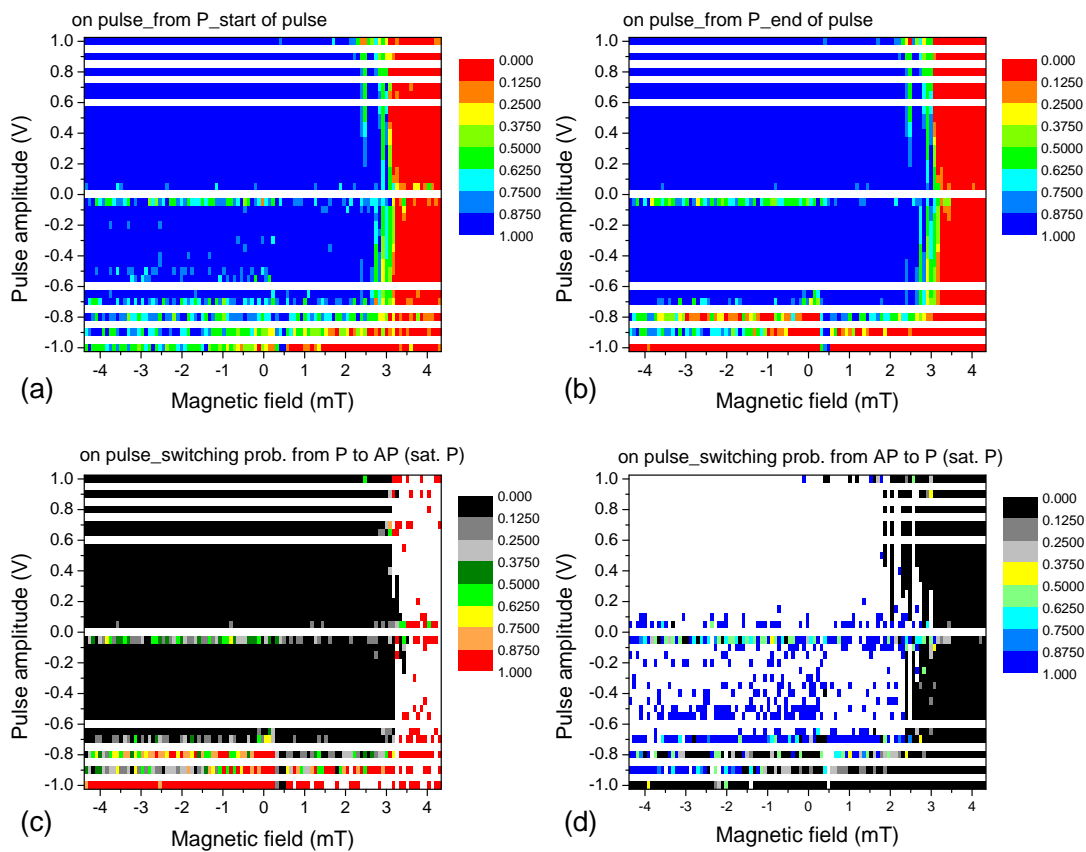


Figure 4.16: On-pulse phase diagram for sample 3 starting from P saturation. (a) shows the determined start state of the sample, (b) the end state. (c) shows the real switching probability from all P start states to AP, (d) shows the switching probability from all AP start states to P. The colour code corresponds to the switching probability, white pixels indicate that no data was available.

from these phase diagrams is the same as measured on the DC MR loops. Therefore, end-state phase diagrams include measurements where the initial start state had already been altered through thermal activation before the voltage pulse was applied. Another consequence of thermal activation is a switching field distribution at each pulse amplitude, reflecting the stochastic nature of the process. This causes the difference between the end-state phase diagrams and those plotting the state at the start of the pulse (figure 4.16 (a) and figure 4.17 (a)).

The probability that the sample actually switches during the pulse is plotted in figures 4.16 (c), 4.16 (d), 4.17 (c) and 4.17 (d).

For the case of the sample initially saturated in the P state ( $N=10$ ), the number of traces recorded with the sample actually starting in the P state ( $N_P$ ) was determined for every field and voltage pulse amplitude. For these measurements, the number of

switching events was determined and subsequently normalised by  $N_P$  in order to obtain the P to AP switching probability during the pulse. Note that the absolute value of  $N_P$  is different for every point of the phase diagram and this procedure yields no values in the case of  $N_P = 0$ . This is plotted in figure 4.16 (c). Figure 4.16 (d) plots the AP to P switching probability for the case when the sample was saturated in the P state, but nevertheless was in the AP configuration at the beginning of the pulse.

A similar analysis was performed for the data obtained after the device was saturated in the AP state (figures 4.17 (c) and 4.17 (d)).

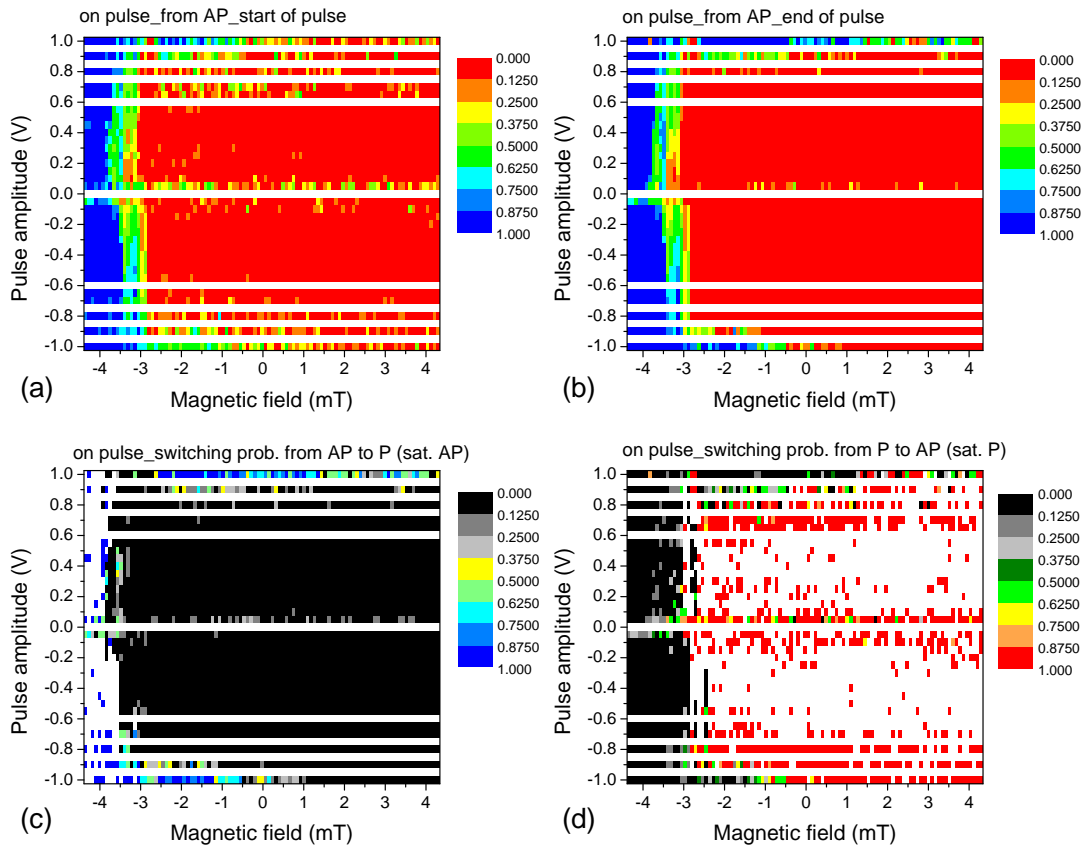


Figure 4.17: On-pulse phase diagram for sample 3 starting from AP saturation. (a) shows the determined start state of the sample, (b) the end state. (c) shows the real switching probability from all AP start states to P, (d) shows the switching probability from P start states to AP. White pixels indicate that no data was available.

The SNR at  $\pm 50$  mV was too low to reliably analyse the state of the sample. This can be seen in all of the on-pulse phase diagrams as the speckled horizontal lines. A second source of artefact for the on-pulse phase diagrams was a change in the contact resistance during the measurement, probably due to slight movements of the HF tips on the sample surface. This effects the phase diagrams in fig. 4.16 for fields smaller than

0.5 mT and negative voltage pulses and in figure 4.17 for fields smaller than -2.61 mT and positive voltage pulses. Consequently, the data does not allow for any reliable fit aiming at extracting the bias-dependence of the in-plane STT component. An attempt at estimating the bias-dependence of the perpendicular STT term yields a torkance in the same range as the off-pulse measurement. This is unsurprising, since in both approaches the perpendicular STT is determined from line 3 and 6 on the phase diagram. These lines correspond to field-induced switching, which remains thermally activated in these experiments.

It is worth pointing out that the critical voltages for switching are generally lower in the on-pulse phase diagram than in the off-pulse measurement. This is probably related to the fact that on the off-pulse experiment, there is a non-zero probability for the sample to return to the initial state due to thermal activation before the resistance is probed.

These experiments demonstrate that it should, in principle, be possible to (at the very least) determine the bias-dependence of the in-plane STT from the on-pulse phase diagram at room temperature, with samples allowing for a stable contact. Field-induced switching remains thermally activated and thus low-temperature measurements are required to determine the bias-dependence of the perpendicular STT.

#### 4.1.2.4 Low-temperature DC phase diagram

A DC phase diagram was measured at 4.2 K in a LakeShore Cryogenic Probe Station using a liquid-Helium-cooled superconducting magnet (in the laboratory of Dr. Artur Erbe). Both voltage sourcing and current measurement were carried out by a Keithley 2401 model. During the measurement, the temperature variations remained below 1 K.

Figure 4.18 displays several low-temperature R-H loops measured for different applied bias voltages, as well as the room temperature R-H loop recorded for the same sample, for comparison. The coercivity of the sample decreased from 13.5 mT at 4.2 K to 0.25 mT at room temperature, as consequence of thermal activation.

Figure 4.19 shows the DC phase diagram at 4.2 K, as determined from R-H loops measured at constant applied bias voltage. The obtained phase diagram disagrees with the theoretical model, but is similar to a DC phase diagram measured at 4.2 K by Oh et al. [10] (see figure 2.12, MTJ2) for an asymmetric MTJ with a 2.3 nm thick Co-rich free layer of  $\text{Co}_{49}\text{Fe}_{21}\text{B}_{30}$ . The authors interpret the results as stemming from the presence of an additional linear term in the perpendicular STT component, due to the asymmetric structure of the MTJ. However, introducing an additional linear term for the

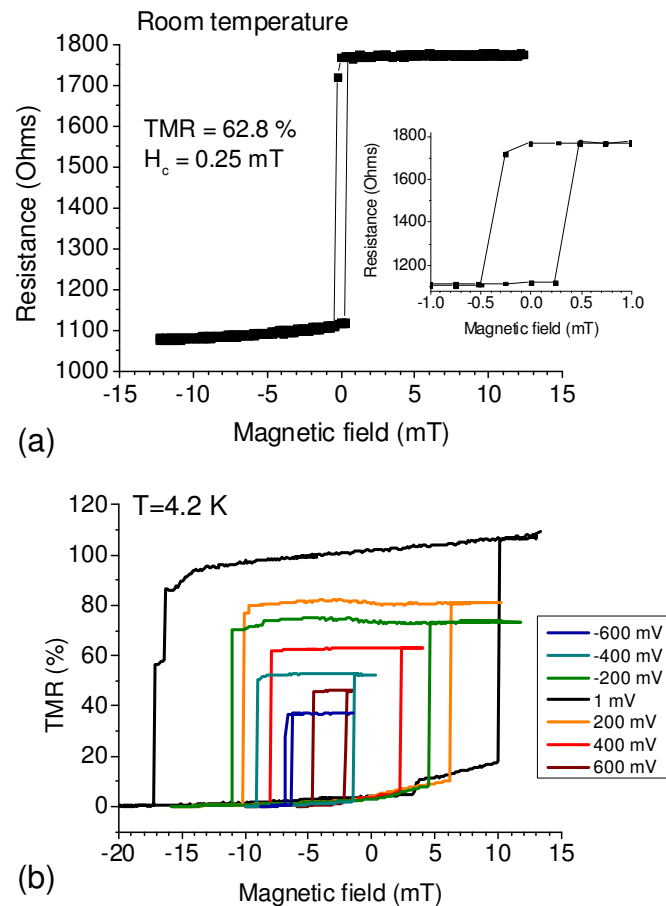


Figure 4.18: DC Magnetoresistance loops of sample 6 taken at (a) room temperature at constant current ( $1 \mu\text{A}$ ) and (b) 4.2 K at different constant voltages (not all shown) with a step size about 0.1 mT. From the measurements in (b), the phase diagram in figure 4.19 was extracted.

perpendicular STT in the analytical calculations does not change the general shape of the predicted phase diagram. Its main effect is to shift the minima of the two parabolas (line 3 and 6) away from  $V = 0$ . Possible explanations for the differences between theory and experiment include:

- The actual temperature of the sample during the measurement is unknown, as Joule heating may cause considerable temperature variation in the experiment, and thus induce an apparent decrease of coercivity with increasing bias. Note that the scans were performed starting from positive fields, and there is approximately a factor of 2 difference between the resistances of the two states, which implies a similar difference in the actual sample temperature for the two transitions on the MR loops. In addition, the resistance of the AP state strongly depends on



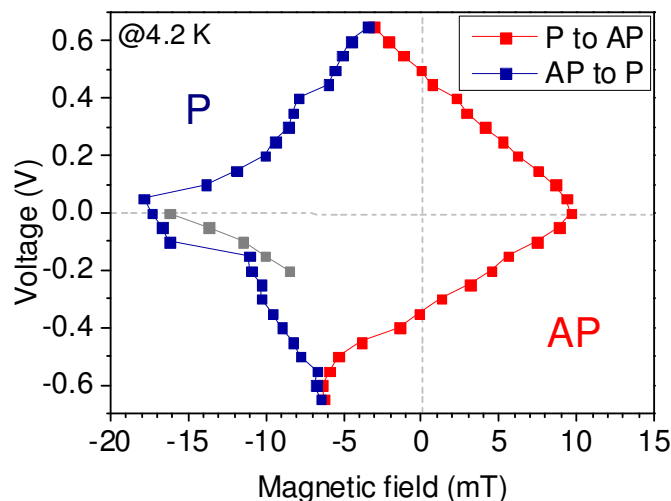


Figure 4.19: Low temperature (4.2 K) DC phase diagram of sample 6 obtained from magnetoresistance loops at different constant applied voltages. The right branch (red) represents switching from P to AP, whereas the left branch (blue) indicates switching from AP to P. The grey points indicate the start of the switching from AP to P for cases with steps in the MR loop.

the bias, which impacts the amount of Joule heating generated as well. Further experiments will be conducted using voltage pulses as opposed to DC bias in order to limit Joule heating.

- For the switching from the AP to the P state, several steps in the hysteresis curve were observed for small negative voltages (0 to -0.2 V), as indicated on the MR loop in figure 4.18. The position of these steps is also indicated in figure 4.19. The grey data points indicate the start of the switching from AP to P for the cases with steps in the MR loop, whereas the blue curve represents the end of the switching process towards the P state. The fact that the switching is not sharply defined for this switching branch might indicate an inhomogeneous magnetisation configuration (either the two-domain state or a vortex-like magnetisation distribution). Consequently, a comparison with a macrospin model is not appropriate. Further measurements on different samples are thus required.

## 4.2 Thermally excited ferromagnetic resonance

A second approach to determine the STT bias-dependence is the thermally excited ferromagnetic resonance, whereby the applied magnetic field and the in-plane STT favour the same state. Here we present the TE-FMR measurements on a different sample from

the same set (sample 4). In the following, we discuss data obtained at two different field values and for different voltage magnitudes. The analysis is done in four steps:

1. Individual spectra are smoothed and fitted with a Lorentz function to determine the linewidth and peak position.
2.  $M_s$  is estimated from the frequency dependence on the field.
3. The perpendicular STT parameter is determined from the peak position and its dependence on applied bias.
4. The damping factor and the in-plane STT parameter will be extracted from the linewidth as a function of the applied bias voltage.

### 4.2.1 Smoothing and fitting of raw data

The R-H and R-I loop of sample 4, which was used for the TE-FMR, can be seen in figure 4.20. The TMR was 80 % and the coercivity was low (0.53 mT). The shift of the

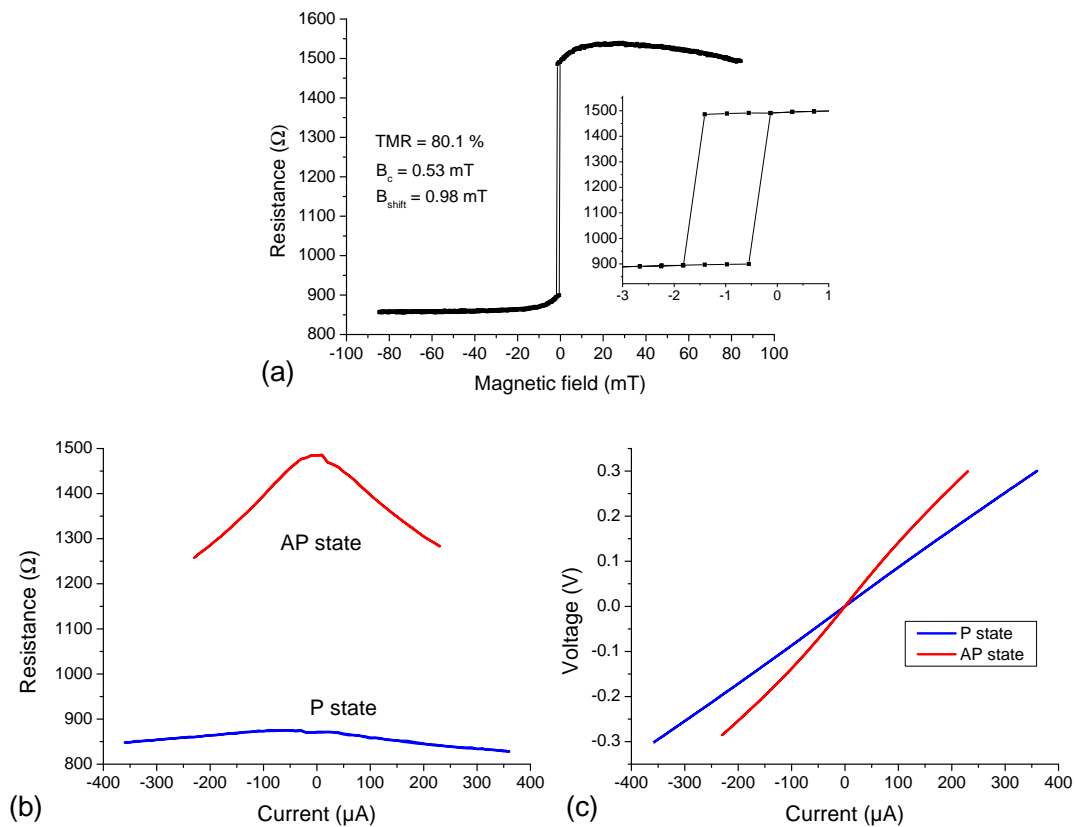


Figure 4.20: (a) Resistance versus magnetic field (R-H) and (b) resistance versus current (R-I) loops for sample 4 for the two magnetic fields at which the TE-FMR spectra were taken. (c) shows the data of (b) in voltage vs. current for the two states.

MR loop (corresponding to average antiferromagnetic coupling with  $B_{\text{shift}} = 0.98$  mT) is the result of competing effects between antiferromagnetic magnetostatic interaction between the free and the SAF layer, and coupling through barrier roughness (orange-peel coupling) favouring the parallel configuration. The magnetic fields for the TE-FMR measurements were set (almost) symmetrically around the center of the loop at  $-2.3$  mT (P) and  $+0.9$  mT (AP).

The TE-FMR spectra were taken at a constant current. The current was increased with a step of  $10$   $\mu\text{A}$  up to a maximum current  $350$   $\mu\text{A}$  for the P configuration and  $-220$   $\mu\text{A}$  for the AP state. Taking into account the resistance of the two states, the maximum applied bias voltage was  $0.3$  V in both cases. The applied current was converted to voltage using the IV curves shown in figure 4.20 (c).

The background spectrum taken at zero current was subtracted in order to obtain the change in the spectrum induced by the STT. The data were then smoothed using a Savitzky-Golay filter with a window of 20 points and polynomial order of 2. The effect of the smoothing can be seen in the example given in figure 4.21. The smoothing

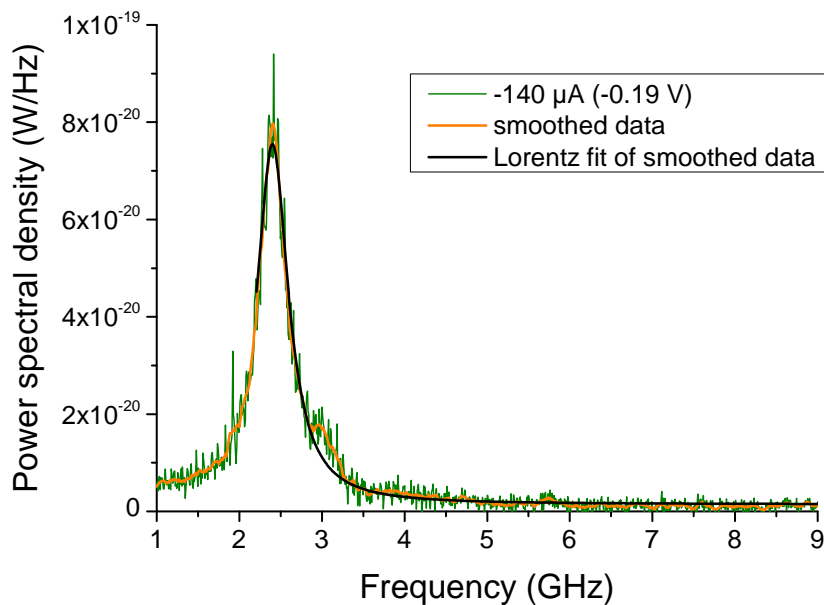


Figure 4.21: Example of smoothing and fitting the data in the TE-FMR measurement for the case of  $B_{\text{ext}} = 0.9$  mT and  $I = -140$   $\mu\text{A}$  for sample 4.

does not introduce additional distortions of the signal. Finally, the smoothed data is fitted with a Lorentz function. The data range for the fit was restricted to reduce the influence of the  $1/f$  noise at low frequencies. However, a comparison to a fit over the whole frequency range resulted in no significant change, emphasising the stability of

the fitting procedure. Since the smaller peak (around 3 GHz) is not distinguishable at lower voltages, only the largest peak was fitted and analysed.

#### 4.2.2 Determination of $M_s$

In order to extract the bias-dependence of the two STT terms from the TE-FMR data, the value of the saturation magnetisation needs to be estimated. The effective magnetisation was determined from the frequency shift with the applied magnetic field of the TE-FMR signals, based on a Kittel formula. Two series of TE-FMR spectra for fields up to  $\pm 120$  mT can be seen in figure 4.22. In the parallel state, the signal shifts to

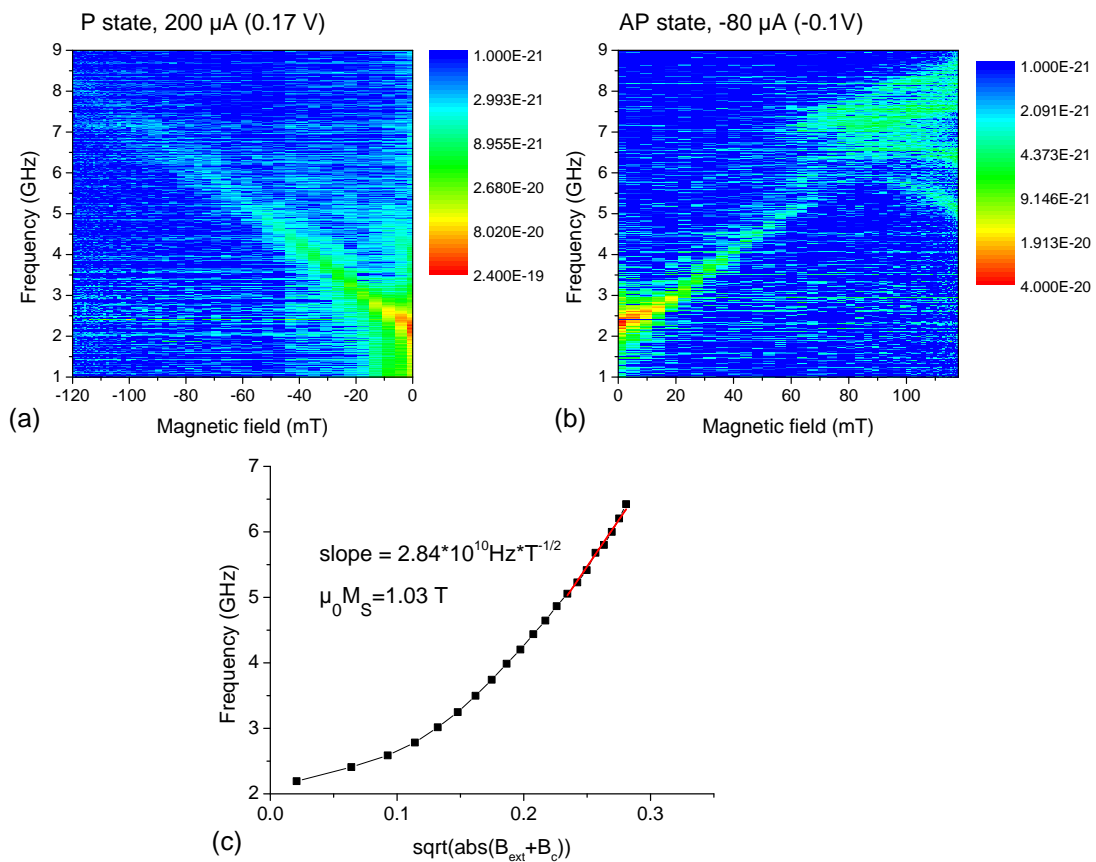


Figure 4.22: Overview over TE-FMR spectra for sample 4 for large field ranges and different applied currents: (a) 200  $\mu\text{A}$ , (b) -80  $\mu\text{A}$ , (c) Determination of  $M_s$  for the applied current of 200  $\mu\text{A}$ . Only the linear part of the graph was fitted (red line), the resulting  $M_s$  was determined from the slope of the curve in a high magnetic field range.

higher frequency with increasing negative field, as expected from the Kittel formula (figure 4.22 (a)). In the antiparallel configuration (figure 4.22 (b)), a similar trend is observed up to 60 mT. At larger fields, however, the main peak amplitude is decreasing

and four different peaks emerge. At least two of these peaks shift to lower frequencies with increasing fields and can thus be attributed to excitations of the synthetic antiferromagnet (SAF). The SAF can be excited in this configuration since both field and STT destabilise the antiparallel state of the reference layer [92].

To estimate the saturation magnetisation, we consider only the large field range where the in-plane anisotropy and the field-like torque become negligible with respect to the external field. The data in figure 4.22 (c) was extracted from the spectra measured in the P state (in figure 4.22 (a)).

Under the assumption of the saturation magnetisation being much larger than the applied field ( $\mu_0 M_s \gg B_{\text{ext}} + B_c$ ), the Kittel formula

$$f_r = \frac{\gamma}{2\pi} \sqrt{(B_{\text{ext}} + B_c)(B_{\text{ext}} + B_c + \mu_0 M_s)} \quad (4.27)$$

can be reduced to:

$$f_r = \frac{\gamma}{2\pi} \sqrt{B_{\text{ext}} + B_c} \sqrt{\mu_0 M_s}. \quad (4.28)$$

Fitting the data in the field range between -54...-78 mT using equation (4.28) yields  $\mu_0 M_s = 1.03$  T (see figure 4.22 (c)).

It should be noted that estimating  $M_{\text{eff}}$  from a lower field range resulted in a considerably lower value for the magnetisation, indicating that the low-field magnetisation configuration of the free layer is inhomogeneous.

The estimated value of  $\approx 1$  T is reasonable and in agreement with previous reports. Bilzer et al. have determined the effective magnetisation  $M_{\text{eff}}$  for thin (extended) CoFeB films of different compositions and film thicknesses from a fit of the FMR resonance frequencies at high magnetic fields [93].  $M_{\text{eff}}$  was found to decrease with increasing boron content and decreasing layer thickness [93]. The value for 5 nm thick  $\text{Co}_{72}\text{Fe}_{18}\text{B}_{10}$  was 1.54 T (as deposited) and 1.76 T for the annealed sample.

In ultra-thin layers, such as considered here (1 nm CoFeB and 0.5 nm Fe), the effective magnetisation will be further decreased as it is counterbalanced by a significant perpendicular anisotropy component in thin CoFeB/MgO/CoFeB MTJs due to interfacial effects, as demonstrated in first-principle calculations. This effect is attributed to hybridization of Fe and O orbitals, thus changing the orbital magnetic moment [94]. It has also been experimentally proven, that a 1.3 nm CoFeB free layer in an MgO-MTJ is magnetised fully out-of-plane [95].

### 4.2.3 Signal evolution with bias voltage

The evolution of the smoothed TE-FMR peaks with the current can be seen in figure 4.23 for the two field values considered. The signals are more than twice larger in the P than in the AP configuration and the P state exhibits larger  $1/f$ -noise. Both features indicate that, although the average effective field is the same in the two experiments, the local field distribution of the magnetic configuration of the free layer is less homogeneous in the P state.

In the case of both in-plane STT and field favouring the AP state (figure 4.23 (a)), two peaks are visible around 2.4 and 3.0 GHz. These two peaks can be attributed to end and center precession modes in the free layer [64, 70]. At the center of the sample, the ferromagnetic coupling through roughness dominates the AP coupling to the SAF. Thus, the resulting coupling field opposes the external magnetic field and consequently reduces the local effective field. This leads to a reduced precession frequency according to the Kittel formula. In the case of the ends of the ellipse, the effect of the magneto-static coupling is larger, which translates into an increase in the effective field leading to an increase in the precession frequency [64].

For external fields favouring the P configuration (figure 4.23 (b)), the peak at lower frequency is identified as the end mode, since the larger magnetostatic field (favouring the AP alignment) is now opposing the external field. The increase in the precession frequency for the second (center mode) peak is due to the ferromagnetic coupling adding to the external field and therefore increasing the local effective field at the center of the free layer.

As indicated by arrows, with increasing current the peak frequencies shift in opposite directions for the two alignments. This can be explained by the effect of the perpendicular STT. Since it favours the AP state independently from the current sign, its effect is to either increase the effective field for AP alignment (increase in precession frequency, blueshift) or to decrease the effective field for the P alignment (decrease in the precession frequency, redshift). It has been shown that a shift in frequency might also occur due to an increase in temperature [96]. However, this effect should be symmetric with current (redshift) and can therefore not explain the behaviour observed here.

For the experiments discussed here, the sign of the bias voltage was chosen so that the in-plane STT acts in the same direction as the damping. Since the linewidth is proportional to the effective damping, increasing the applied current leads to an increase

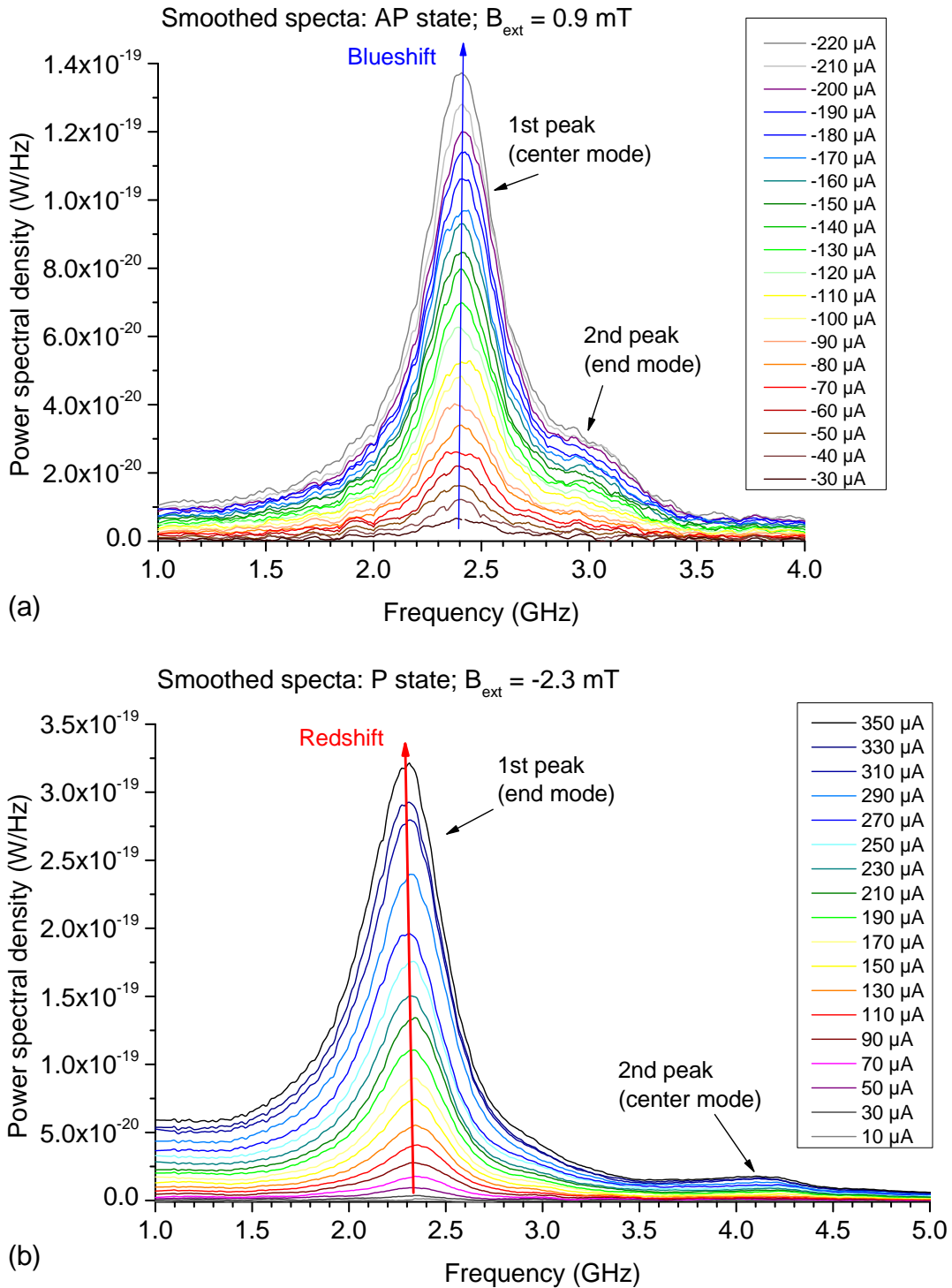


Figure 4.23: Smoothed spectra for sample 4 from the TE-FMR for (a) AP and (b) P state. The blue- and redshift of the peaks with current are indicated and can be attributed to the effect of the perpendicular STT. The different peaks refer to different precession modes. In (b), only every second measurement is shown for clarity.

in linewidth for both the P and AP state, as evidenced by figure 4.23.

#### 4.2.4 Analysis of peak position: perpendicular STT

The bias-dependence of the perpendicular STT is estimated from the change of the resonance frequency with the applied voltage. We assume, that the perpendicular STT introduces an additional bias-dependent effective field,  $B_{\perp}(V)$  in the Kittel formula, which is then written as:

$$f_r(V) = \frac{\gamma}{2\pi} \sqrt{(B_{\text{net}} + B_k + B_{\text{coupl}} + B_{\perp}(V)) (B_{\text{net}} + B_k + B_{\text{coupl}} + B_{\perp}(V) + \mu_0 M_s)}. \quad (4.29)$$

The bias-dependence for the perpendicular STT in the fit is assumed to have a second order polynomial dependence:  $B_{\perp}(V) = a_{\perp 0} + a_{\perp 1}V + a_{\perp 2}V^2$ . For the fitting of the data, the two bias-dependent parameters  $a_{\perp 1}$  and  $a_{\perp 2}$  were forced to be the same for the two branches of the data (P and AP configuration). The only difference allowed was a constant relative shift in the resonance frequency between the two branches to take into account the different effective fields, due to the difference in the effective coupling, which introduces a jump in the resonance frequency at zero voltage (figure 4.24).

The equation used for fitting was

$$f_r(V) = \frac{\gamma}{2\pi} \sqrt{\left(\beta + (a_{\perp 1}V + a_{\perp 2}V^2) \frac{V}{|V|}\right) \left(\beta + (a_{\perp 1}V + a_{\perp 2}V^2) \frac{V}{|V|} + \mu_0 M_s\right)}. \quad (4.30)$$

where the difference in the effective magnetic fields of the two modes ( $\delta$ ) is described by the two fitting parameters  $\epsilon$  and  $\delta$  ( $\beta = \epsilon + \frac{1}{2} \frac{V}{|V|} \delta$ ). These two parameters include the net external magnetic field,  $B_{\text{net}}$ , the anisotropy,  $B_k$ , the ferromagnetic (Néel) and dipolar coupling,  $B_{\text{coupl}}$  and the exchange coupling,  $a_{\perp 0}$ .

The fit of the data can be seen in figure 4.24. Please note that the data consist of the TE-FMR data set determined in the AP state (negative voltage) and the data set from the P state (positive voltage).

For the perpendicular STT, a quadratic voltage dependence with a small linear component was found. The determined STT parameters are shown in table 4.1. The values are given in different units for better comparison with the literature. The quadratic component favours the same state (AP) and is about one order of magnitude smaller than some of the literature values (e.g. Kubota et al.:  $1.73 \times 10^{-19}$  J/V<sup>2</sup> [5] and Deac et al.:  $2.09 \times 10^{-19}$  J/V<sup>2</sup> [64]), but it is in the same range as some other publications



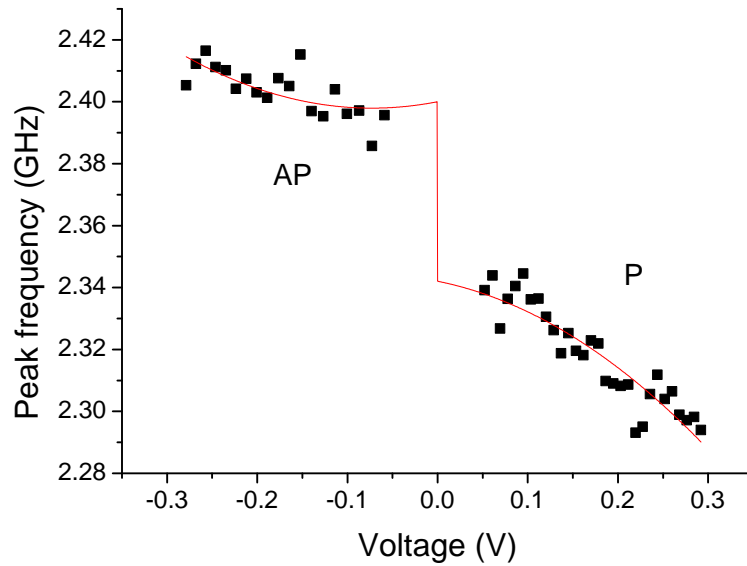


Figure 4.24: Analysis of peak frequency vs. applied bias voltage for sample 4 in the TE-FMR: Determination of perpendicular STT parameter from the effective field change due to the perpendicular STT at different bias voltages. Both data from P and AP configuration were fitted simultaneously using equation (4.30).

$a_{\perp 1}$ (linear)	-0.34 mT/V	$-5.19 \times 10^{-21}$ J/V	$-1.25 \times 10^9$ ( $\Omega\text{m}^2$ ) $^{-1}$
$a_{\perp 2}$ (quadratic)	-2.36 mT/V $^2$	$-3.56 \times 10^{-20}$ J/V $^2$	$-8.56 \times 10^9$ ( $\Omega\text{m}^2\text{V}$ ) $^{-1}$

Table 4.1: Perpendicular STT values determined from the voltage bias-dependent TE-FMR peak frequencies with linear and quadratic component in various units for comparison to literature. The signs imply that the linear component favours the AP (P) state for positive (negative) voltages, whereas the quadratic component always favours the AP state (in the sign convention used in this thesis, positive voltage favours the P state).

such as Sankey et al.:  $2.76 \times 10^{-20}$  J/V $^2$  [4] or Wang et al.:  $5.26 \times 10^{-20}$  J/V $^2$  [67]. It should be noted that the samples from the last two references, which are in good agreement with the value determined here, were also fabricated at IBM like the samples studied in this thesis.

## 4.2.5 Analysis of peak linewidth

### 4.2.5.1 Determination of in-plane STT parameter

The change of the linewidth by the applied voltage can be described as a sum of the intrinsic contribution due to the damping and the in-plane STT contribution as an effective field  $B_{||}(V)$  [69]:

$$\Delta f_r(V) = \frac{\gamma}{2\pi} \alpha (\mu_0 M_s + 2(B_{\text{net}} + B_k + B_{\text{coupl}})) + \frac{\gamma}{2\pi} 2B_{||}(V). \quad (4.31)$$

Similar to the analysis of the perpendicular STT, the linewidth dependence of both data sets (P and AP configuration) can be fitted using a second order polynomial dependence:  $B_{||}(V) = a_{||0} + a_{||1} V + a_{||2} V^2$ . For the fit, the two bias-dependent parameters  $a_{||1}$  and  $a_{||2}$  were forced to be the same for the two branches of the data. As previously, the only difference allowed was a constant relative shift in the linewidth between the two branches to take the different effective fields due to the difference in the effective coupling into account.

The equation used for fitting was

$$\Delta f_r(V) = \frac{\gamma}{2\pi} \left[ \alpha (\mu_0 M_s + \beta) + 2(a_{||1} V + a_{||2} V^2) \frac{V}{|V|} \right], \quad (4.32)$$

where the difference in the effective magnetic fields of the two modes ( $\delta$ ) is described by the two fitting parameters  $\epsilon$  and  $\delta$  ( $\beta = \epsilon + \frac{1}{2} \frac{V}{|V|} \delta$ ). These two parameters again include the net external magnetic field,  $B_{\text{net}}$ , the anisotropy,  $B_k$ , the ferromagnetic (Néel) and dipolar coupling,  $B_{\text{coupl}}$ , and  $a_{||0}$ .

The data and the fit of the linewidth versus voltage are shown in figure 4.25. From the fit, the voltage dependence looks linear, but there was also a small quadratic term. The quadratic term does not play a role for low voltages, but at higher voltages it should be taken into account (it has a magnitude of 16 % of the linear component at 0.3 V). The determined in-plane STT parameters are listed in table 4.2.

$a_{  1}$ (linear)	+3.63 mT/V	$+5.48 \times 10^{-20}$ J/V	$+1.32 \times 10^{10}$ ( $\Omega\text{m}^2$ ) <sup>-1</sup>
$a_{  2}$ (quadratic)	-1.94 mT/V <sup>2</sup>	$-2.92 \times 10^{-20}$ J/V <sup>2</sup>	$-7.04 \times 10^9$ ( $\Omega\text{m}^2\text{V}$ ) <sup>-1</sup>

Table 4.2: In-plane STT values determined from the bias voltage dependent TE-FMR linewidths. The signs imply that the linear component favours the P (AP) state for positive (negative) voltages, whereas the quadratic component always favours the AP state (in the sign convention used in this thesis, positive voltage favours the P state).

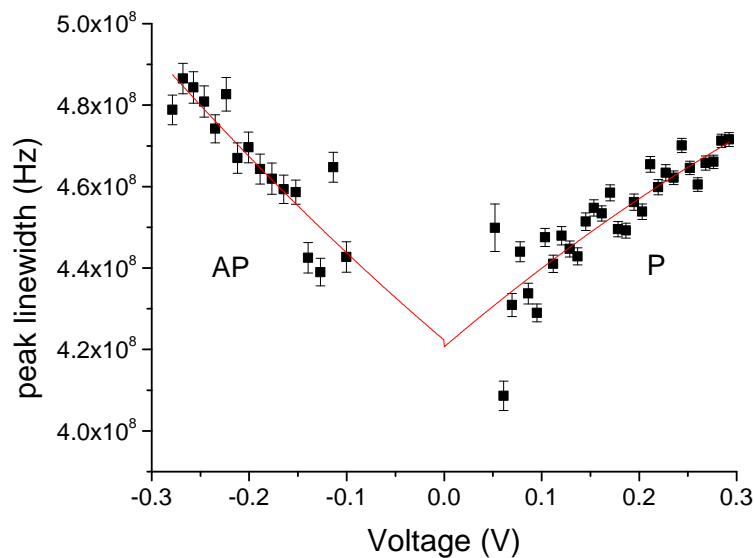


Figure 4.25: Analysis of peak linewidth vs. applied bias voltage for sample 4 in the TE-FMR: determination of the in-plane STT from the linewidth at different bias voltages. Both data from P and AP configuration were fitted simultaneously using equation (4.32). The damping factor  $\alpha$  was also determined from the fit.

Similar to the out-of-plane STT, the in-plane STT parameter is about one order of magnitude smaller than some of the literature values (e.g. Kubota et al.:  $4.55 \times 10^{-19}$  J/V [5]). But it is in the same range as some other publications such as Deac et al.:  $2.78 \times 10^{-20}$  J/V [64], Sankey et al.:  $4.27 \times 10^{-20}$  J/V [4] and Wang et al.:  $3.29 \times 10^{-20}$  J/V [67]. Again, the last two references, which have studied samples which were also fabricated at IBM, are in good agreement with the value determined here.

#### 4.2.5.2 Determination of damping factor $\alpha$

The intrinsic damping factor  $\alpha$  can be determined from the linewidth at zero bias voltage, where the in-plane STT does not contribute. From the fit shown in figure 4.25, the damping factor was determined as  $\alpha = 0.015$ . Fuchs et al. who have investigated an elliptical spin-valve (cross section of  $50 \times 110$  nm) with a 3.5 nm thick  $\text{Co}_{60}\text{Fe}_{20}\text{B}_{20}$  free layer by measuring spin-transfer torque-FMR found  $\alpha = 0.014$  [97].

It should be noted that the value depends strongly on the value of the saturation magnetisation used (an exemplary fit for  $M_s = 0.5$  T would yield  $\alpha = 0.025$  and for  $M_s = 1.5$  T:  $\alpha = 0.011$ ). In general, measurements performed at lower magnetic fields resulted in a larger damping factor. Like the reduced  $M_s$  value estimated from the low field data, the increase in the effective damping under these circumstances can also

be attributed to an inhomogeneous magnetisation configuration, which introduces an additional 'inhomogeneous line broadening'.

The influence of the thickness of the CoFeB films and the annealing was investigated by Bilzer et al. [93] by network-analyzer FMR on extended films. The damping factor of 5 nm thick  $\text{Co}_{72}\text{Fe}_{18}\text{B}_{10}$  increases from  $\alpha = 0.008$  (as deposited) to  $\alpha = 0.012$  after annealing at 280 °C due to the crystallisation. This effect is less pronounced for thinner materials.

Since the exact composition of the CoFeB in the samples investigated in this thesis is not known, it is interesting to know how changes in the composition effect the damping factor. Hayakawa et al. have investigated two different stacks with either Co-rich  $\text{Co}_{40}\text{Fe}_{40}\text{B}_{20}$  or Fe-rich  $\text{Co}_{20}\text{Fe}_{60}\text{B}_{20}$  synthetic ferrimagnetic layers. It was found that increasing the Fe content leads to a smaller damping factor, a higher TMR ratio and a lower effective magnetisation [98]. This is confirmed by Natarajarathinam et al. who have determined the damping factor by conventional FMR technique for extended films of either  $\text{Co}_{40}\text{Fe}_{40}\text{B}_{20}$  or  $\text{Co}_{31.5}\text{Fe}_{58.5}\text{B}_{10}$  [99]. The damping factor is found to increase for thinner films (in the range of 8 nm to 1 nm). Taking all these facts into account, the extracted damping factor is a reasonable value.

# 5

## Summary and outlook

---

During the course of this PhD, an experimental setup was built to perform DC and high frequency switching experiments. This makes it possible to perform field-driven and current-driven STT switching experiments of magnetic tunnel junctions. Pulsed switching experiments can also be carried out, allowing for the simultaneous detection of the DC resistance and the reflected voltage pulse using a real-time 20 GHz oscilloscope. Furthermore, high-frequency phenomena like steady state magnetisation precession (either driven by spin-transfer torques or excited thermally) can also be investigated in the frequency domain, using a spectrum analyser.

The samples investigated were state-of-the-art CoFeB/MgO-based in-plane magnetised MTJs fabricated by IBM Research (USA). The MTJs were patterned into nanopillars with an elliptical cross section, with a lateral size of the order of 100 nm. The devices had a typical RA product of  $8.5 \Omega\mu\text{m}^2$  and a tunnel magnetoresistance around 70 %.

The abrupt DC field- and STT-induced switching was consistent with coherent magnetisation reversal. The obtained critical current densities were in the range of  $2.3 \times 10^6 \text{ A/cm}^2$ , consistent with previous reports. For the case of current and field favouring opposite states, sudden jumps in the resistance between the P and AP state were observed for currents above the critical switching current. This behaviour, typically referred to as 'back-hopping' in the literature, was also observed in experiments where the switching was induced by the external field.

Back-hopping is highly undesirable when considering the potential application of MTJs as magnetic random access memory cells using STT-induced switching as write scheme. Since the critical voltages vary from element to element as consequence of size fluctuations, a certain overdrive voltage is applied to ensure switching of each device.

The occurrence of back-hopping will lead to an unreliable write operation. This effect is usually ascribed to thermally activated reversal.

In this thesis, the influence of the perpendicular STT on the switching was investigated theoretically for different sample geometries. Switching phase diagrams were derived by solving the extended Landau-Lifshitz-Gilbert equation. Additionally, measurements of experimental phase diagrams and TE-FMR were carried out on MgO-based in-plane MTJs, aiming at estimating the bias-dependence of the in-plane and field-like STT contributions. The analytical solutions were adapted to a real sample, based on the experimentally determined material parameters and STT bias-dependence.

### **Switching properties**

To derive an analytical switching phase diagram, the critical switching voltages and magnetic fields were determined by solving the Landau-Lifshitz-Gilbert equation including both the in-plane and perpendicular STT term. Specifically, the critical voltages and fields were defined as the values where a given state (parallel or antiparallel) becomes unstable. The analytical solutions were found to be in good agreement with phase diagrams calculated by numerically integrating the extended LLG equation, which also provided additional information with regards to the presence of precessional states or canted static configurations.

The LLG equation was first solved for the general case, assuming two generic anisotropy components for the free layer of the MTJ. The first component was defined as being oriented along the same direction as the applied field and the magnetic moment of the reference layer, which dictates the direction of the current polarisation. The second anisotropy component was assumed to be perpendicular to the first.

By appropriately defining the anisotropy components with respect to the plane of the layers, as well as their sign, the general solution was then reduced to three experimentally relevant configurations: perpendicularly magnetised MTJs with and without additional in-plane easy axis, as well as in-plane magnetised MTJs with an in-plane shape anisotropy.

For in-plane magnetised MTJs, compared to the metallic case, the critical lines defining the switching field as functions of the applied voltage (lines 3 and 6 in figure 4.6 (a)) exhibit an additional curvature, reflecting the assumption that the field-like torque has a quadratic dependence on the applied voltage and always favours the AP state. This will have consequences for experimental magnetoresistance curves at con-

stant voltage (horizontal scans in the phase diagram). A hysteresis loop at  $V = 0$  yields the anisotropy value of the magnetic free layer, as the horizontal cross section through  $V = 0$  crosses lines 3 and 6 at  $-\mu_0 H_{kz}$  and  $+\mu_0 H_{kz}$ . If the voltage is increased, both switching fields shift to the left for both voltage polarities, but the width of the loop remains twice the anisotropy. Indeed, as the field-like torque favours the AP state, it will assist the external field for switching to the AP state and oppose it for the AP to P reversal. Switching to the AP state will thus require less field to be applied, while the field necessary to induce the opposite transition will be increased in the presence of a finite bias voltage.

The curvature of the two critical lines in the presence of a quadratic field-like STT term can potentially lead to back-hopping, even at zero K. This would explain why back-hopping has not been observed in metallic nanopillars. Indeed, in metallic devices, the perpendicular STT is generally negligible, as evidenced by experimentally determined phase diagrams [89].

The second configuration analysed, fully perpendicular MTJs with no in-plane anisotropy, is the highest symmetry case. The phase diagram consists only of regions where at least one state (P or AP) is stable. No back-hopping is expected for this geometry, as has been experimentally confirmed by Nowak et al. [78]. When taking into account an additional in-plane anisotropy, the phase diagram becomes more complex, with additional regions where the number of allowed states is further reduced. Numerical calculations reveal that canted states are also allowed for this geometry.

The experimental part of the work presented here focused on estimating the STT bias-dependence. Measuring a DC phase diagram at room temperature was found not to be appropriate for a direct comparison with theory, as large thermal activation effects were observed. Therefore, switching was investigated through on- and off-pulse measurements.

While the impact of thermally activated reversal on the phase diagram is limited when using ns-long voltage pulses, in pulsed measurements, thermal activation still plays a major role for field-induced switching, as the duration over which the field is applied is of the order of ms. Consequently, the bias-dependence of the perpendicular STT-parameter determined by fitting the analytical formula describing the voltage dependence of the switching fields yielded  $0.5 \text{ mT/V}^2$ , which is one order of magnitude lower than previously reported in the literature.

A comparison of the off-pulse and on-pulse measurement revealed the effect of the thermal activation after the pulse. The most striking difference between the two

measurements was obtained in the high voltage region, where the voltage pulse clearly induced reversal (detected in the on-pulse measurement), but the probability to return to the initial state until the resistance was probed (after several 100 ms) was non-zero due to thermal activation (off-pulse measurement).

It should be noted that the on-pulse single shot measurement technique enables the user to investigate individual switching events in a very detailed way during the pulse. For switching voltages being not large enough to actually switch, switching attempts to an intermediate resistance value before returning back to the initial state have been detected.

A second approach for reducing thermal activation is to perform low temperature experiments. A DC phase diagram measurement was obtained at 4.2 K. The results are, however, still not suitable for direct comparison with a theoretical model, as consequence of Joule heating causing considerable temperature variation with increasing voltage. Moreover, the sample exhibited features consistent with an inhomogeneous magnetisation configuration of the free layer of the MTJ, which makes an interpretation based on a single domain model inappropriate.

### **TE-FMR - Extraction of parameters**

The second method to determine the STT bias dependence was to measure thermally excited ferromagnetic resonance at different applied bias. TE-FMR enables the determination of material parameters, such as the effective magnetisation and the damping factor, as well as the in-plane and perpendicular torques and their voltage dependence. This technique probes high frequency voltage oscillations due to thermal fluctuations (intrinsically present on the free layer at room temperature) of the magnetisation in an external magnetic field while a small DC bias current or voltage is applied to the sample ( $V < 0.3$  V).

The effective magnetisation was estimated to be  $\approx 1$  T from data obtained at high magnetic fields. This value is in good agreement with the literature, and accounts for the presence of a significant perpendicular anisotropy component in thin CoFeB/MgO-MTJs due to interfacial effects [94, 100].

The bias dependence of the in-plane STT and the perpendicular STT components was determined from the linewidth and peak position dependence on the applied voltage bias, respectively. It was found that the perpendicular STT has the same order of magnitude as the in-plane STT, reaching about 25 % of  $a_{\parallel}$  at the maximum bias of



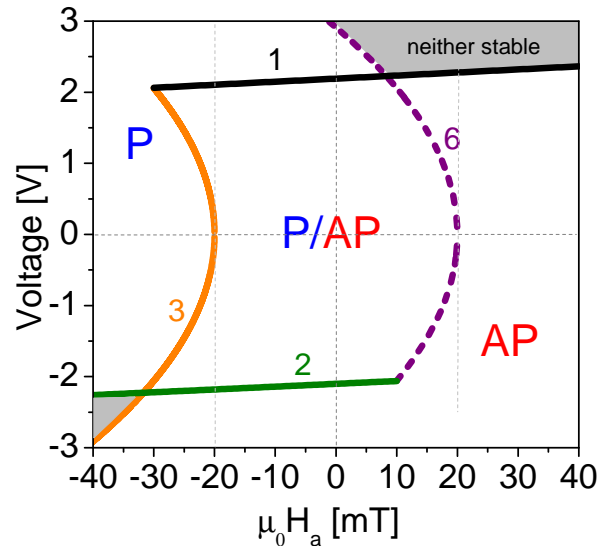


Figure 5.1: Analytical phase diagram with values determined from TE-FMR ( $\alpha = 0.015$ ,  $a_{\parallel 1} = 3.63$  mT/V and  $a_{\perp 2} = 2.36$  mT/V<sup>2</sup>). The anisotropy  $\mu_0 H_{kz}$  was assumed to be 20 mT and the demagnetising field  $\mu_0 H_{kx}$  was set to 1 T.

0.3 V. This is in agreement with the literature [64].

The in-plane STT component,  $a_{\parallel}$ , was found to be mostly linear with the applied voltage, although the fit also yielded a small additional quadratic component. The linear part was about  $5.48 \times 10^{-20}$  J/V. The perpendicular STT was found to consist of a quadratic and a linear term:  $a_{\perp} = a_{\perp 1} V + a_{\perp 2} V^2$  with  $a_{\perp 1} = 0.52 \times 10^{-20}$  J/V and  $a_{\perp 2} = 3.56 \times 10^{-20}$  J/V<sup>2</sup>. Both STT values are in good agreement with previous reports from groups which have investigated samples that were also fabricated by IBM [4, 67]. The small linear term in the perpendicular STT might be due to the asymmetry of the structure of the MTJ, as was both predicted [6] and experimentally observed [10, 70].

The damping was estimated from the linewidth at zero bias voltage:  $\alpha = 0.015$ . This is also in agreement with the literature [97]. In general, a low damping is desired in order to reduce the switching voltages and thus the power consumption for applications.

The phase diagram shown in figure 5.1 was constructed combining the experimentally determined values from the TE-FMR and the analytically derived formulae. The anisotropy and the demagnetising field had to be assumed since they are not known from the experiment for sample 4.

- The anisotropy  $\mu_0 H_{kz}$  was set to 20 mT, which is of the same order of magnitude as the anisotropy of sample 6 measured at 4.2 K in the DC phase diagram (13.5 mT). Increasing the coercivity shifts lines 3 and 6 to higher fields and lines 1 and 2 to higher voltages, according to the analytically determined formulae.

- The demagnetising field  $\mu_0 H_{kx}$  was set to 1 T (as determined experimentally). In general, an increase in the damping, an increase in the demagnetising field and a decrease in the in-plane STT parameter result in higher switching voltages (lines 1 and 2).
- An increased perpendicular STT parameter enhances the bending of the critical switching fields (lines 3 and 6).

### Outlook

The experiments demonstrate that it should, in principle, be possible to determine the bias-dependence of the in-plane STT from the on-pulse phase diagram at room temperature, with samples allowing for a stable contact. The analysis of the on-pulse measurement carried out at low temperature is expected to yield the bias-dependence of the perpendicular STT, for a sample with single-domain like behaviour. Additionally, measurements with different pulse lengths would provide further information on the impact of thermal activation on the phase diagrams.

Furthermore, the results should also be compared with the STT bias dependence as determined from spin-torque FMR measurements on similar devices. This comparison is so far missing in the literature.

Recently, a new set of samples has become available. These devices exhibit different in-plane and out-of-plane anisotropy components, thus providing a perfect test bench for the generalised model. These samples will be investigated in the following months.

# A

## Appendix

---

### **Additional information on experimental setup**

#### **Sample holder and contacting possibilities**

To contact patterned samples in two- or four-point-probe measurements, high frequency (HF) prober tips in a PM5 wafer prober connected via SMA cables are used. Three different small probe heads and one large probe head are also provided in order to either contact films (for determining the resistivity by four wire measurements, i.e. four-point-probe-method or the Van-der-Pauw technique) or to connect to large contact pads of specifically structured devices (resistance measurement).

Both the sample holder and the in-plane electromagnet can be fully turned in-plane without any restriction. The sample can be fixed to the sample holder by a vacuum pump; however, the fixation by glue is recommended since it was found to increase the contact stability.

A Keithley switch is used to connect both a Keithley current source and a Keithley nanovoltmeter to a LEMO connector going to the wafer prober and sample. The switch allows to wire the current and voltage connections in different outputs (to the sample or additionally to ground) without physically changing the wiring.

To provide an easy means for different combinations of SMA/standard LEMO connections for 4-wire or 2-wire measurements, the LEMO connector from the switch can be combined with different connector boxes:

1. A (larger) aluminium box was designed for 4-wire or 2-wire measurements using either an SMA output for the high frequency tips on the wafer prober PM5 or the probe heads with the LEMO connector output.

2. A (smaller) aluminium box with one SMA output was designed for a 2-wire measurement configuration using one high frequency tip of the wafer prober (reflection mode).

## Wiring and control of equipment

The electrical connections within the magnetoresistance setup are shown in figure A.1. The following instruments are connected via ethernet (IP address in brackets) to the PC

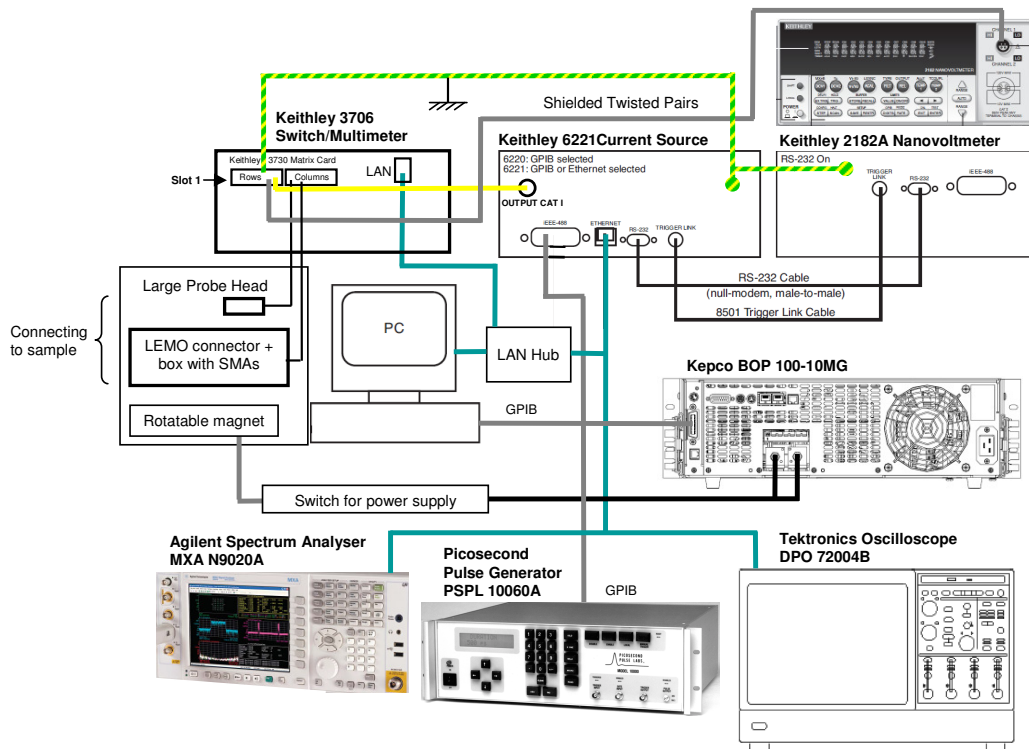


Figure A.1: Wiring of equipment in experimental setup.

(192.168.4.1): current source (192.168.4.2), switch (192.168.4.3), spectrum analyser (192.168.4.4) and oscilloscope (192.168.4.10). The Kepeco power supply for the magnet (GPIB address: 5), the current source (GPIB address: 2) and the pulse generator (GPIB address: 4) are connected via GPIB.

A combination of a Keithley current source and a nanovoltmeter allows a high sensitivity of the measurement at low voltages. The instruments are connected to each other via RS 232 by a serial cable and a trigger link cable. This has the advantage that both instruments can work together as a single unit and can operate in certain modes providing noise compensation. The 'delta mode' employs a moving average algorithm

of three consecutive readings with alternating positive/negative current source output level. This eliminates thermoelectric voltage, reduces the drift of the nanovoltmeter and thereby increases the signal-to-noise ratio. The 'pulse delta mode' is a specially designed mode for heat sensitive devices, whereby the pulsed test current can be increased without overheating the device. However, the nanovoltmeter can also be connected to the PC directly via GPIB (GPIB address: 3) which is faster and easier to program.

The Keithley Switch connects the nanovoltmeter and the current source to the probe head or to the LEMO connector leading to the connector box. Furthermore, it can also set all outputs to ground, which is needed during the contacting process in the case of highly sensitive samples such as the MTJ samples in this thesis (see figure A.2). Nanovoltmeter, current source, switch, the connector boxes and the waferprober are stargrounded. Note that the sample holder is not isolated.

The triax output connector of the current source can be configured in different ways. The configuration for the work in this thesis is that the inner shield is used as current return path (I-), while the outer shield is disconnected from the earth ground. This is done by connecting the triax inner shield to output low and disconnecting output low from earth ground. This setting was chosen because it reduced large electromagnetic interference-induced voltage peaks ( $>1.5$  V) induced in the cables to the connector box which were observed in the guarded configuration (inner shield to cable guard, outer shield and output low to ground).

The connections inside the switch are shown in more detail in A.3. Each cross point relay of the matrix card in the switch has two poles (low and high). Here, always the low pole was used. In general, all channels in the switch should be opened except for those specified for the measurement connecting the LEMO connector with the current source and the voltmeter.

Current source and nanovoltmeter are connected to the **rows** in the switch as indicated. The triax cable from the current source is connected to row 2L (inner shield), row 3L (output high, I+) and row 4L (outer shield). The nanovoltmeter is connected to rows 5L (V+) and 6L (V-). The outputs can be grounded by an extra row connection (Row 1L) in the case of contacting highly sensitive samples.

The cables to the large probe head and the LEMO connector to the connector boxes/sample are soldered to the **columns**. The columns connecting the LEMO connector are 12 (pin 12, I+), 13 (pin 29, I-), 14 (pin 14, V+) and 15 (pin 16, V-). The channel number is composed of the number of the slot of the matrix card (1 in this case), the row and the column. For connecting the current source and nanovoltmeter to the

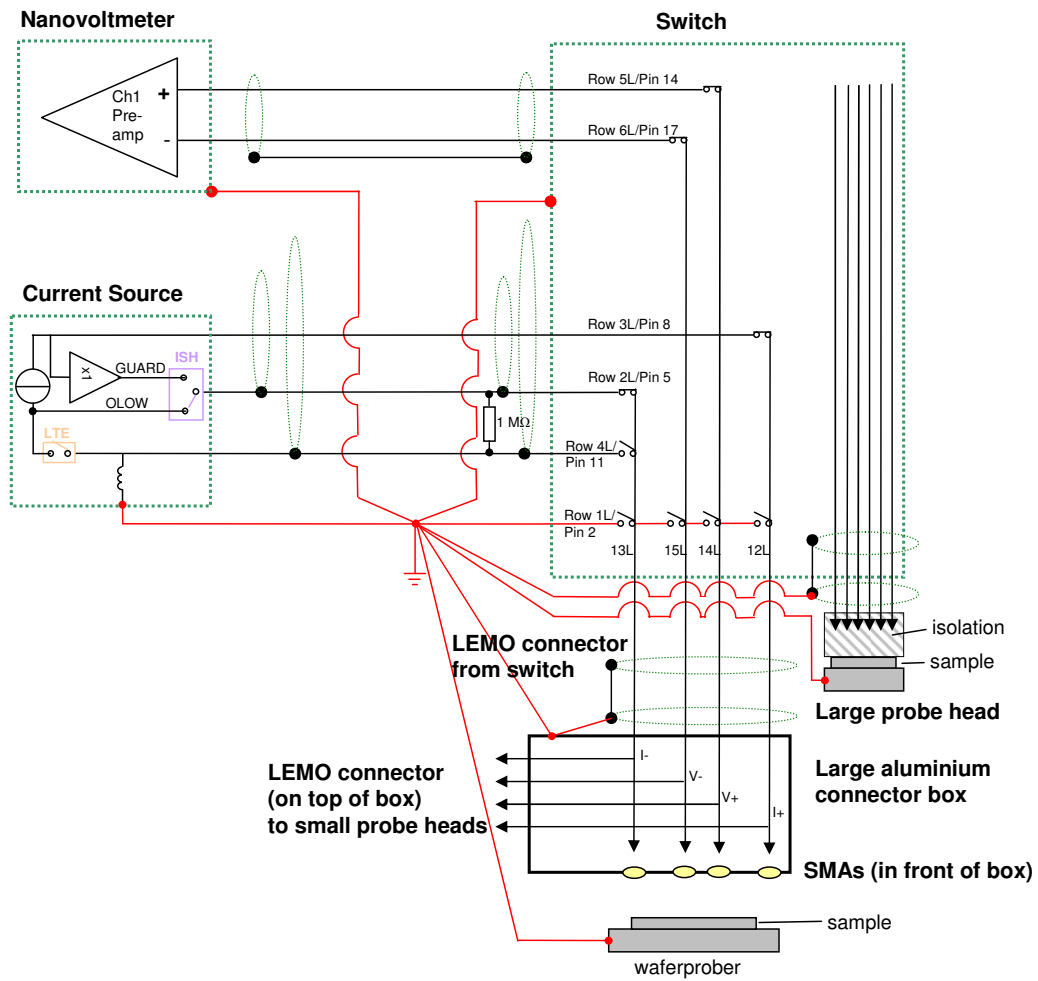


Figure A.2: Wiring of nanovoltmeter, current source and switch in the experimental setup. Current and nanovoltmeter are connected to the rows in the switch whereas the LEMO connector to the connector box and the sample is connected to the columns. An extra row connection (Row 1L) can ground the outputs in the case of contacting highly sensitive samples. The abbreviations used for the output of the current source are: 'OLOW'=output low, 'ISH'=inner shield, and 'LTE'=triax output low earth connection.

LEMO connector, the following four channels have to be closed: 1213 (I-), 1312 (I+), 1514 (V+), 1615 (V-). Everything is grounded/disconnected from ground if channels 1112, 1113, 1114 and 1115 are closed/opened. More details of the setup can be found in the documentation file.

D-sub connection information for 6x16 matrix card (model 3730)

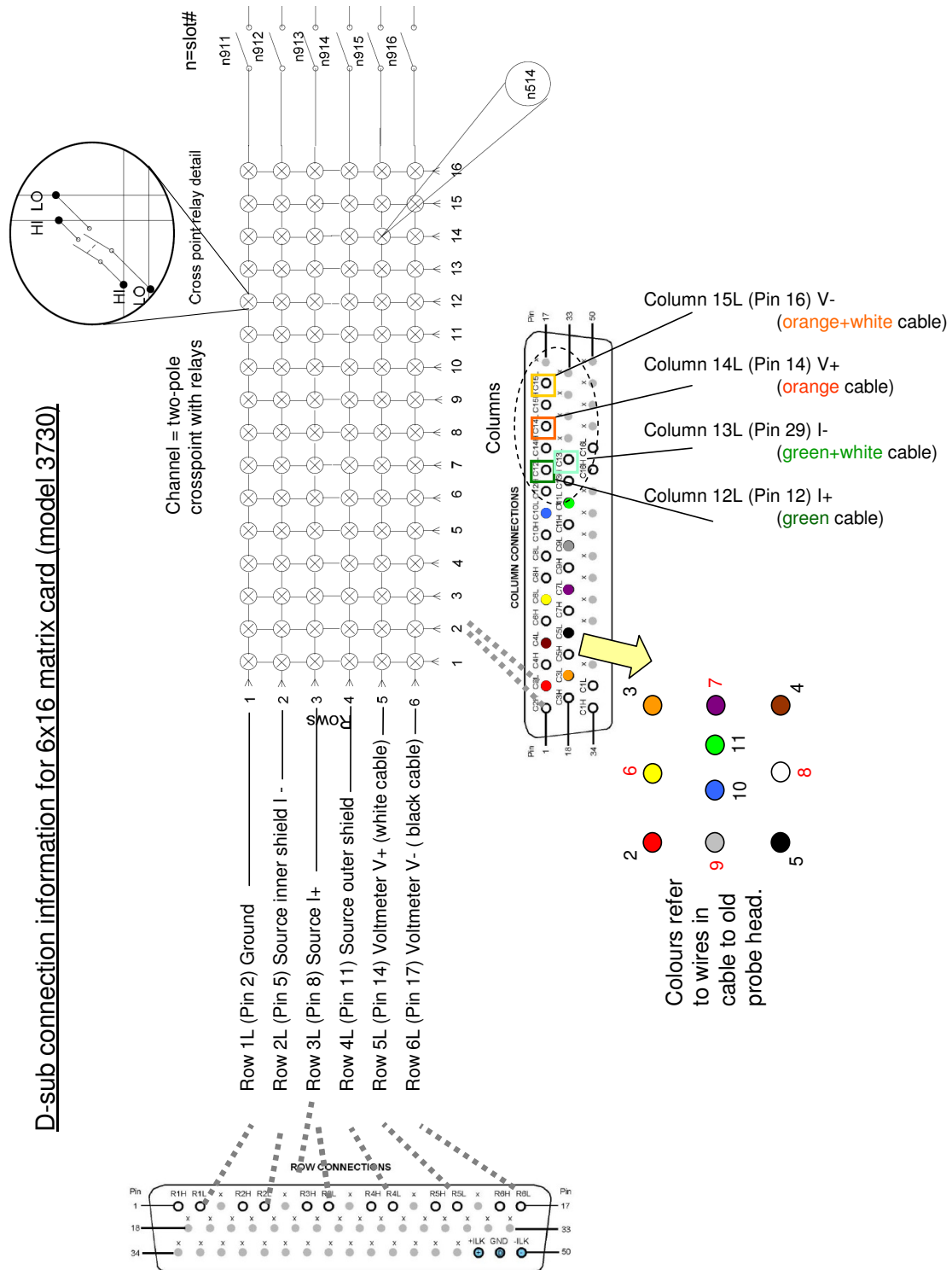


Figure A.3: Wiring of the D-sub connectors to the matrix card in the switch in the experimental setup. The current source, nanovoltmeter and ground are connected to the rows of the matrix card, whereas the connections to the sample (LEMO connector and large probe head) are connected to the columns. By closing individual channels of the switch, the outputs of the measurement devices can be connected in different ways without changing the physical connections.

## Selected specifications of the equipment

The main specifications of the DC equipment in the setup are summarised in table A.1, those of the high frequency equipment can be found in table A.2.

Name of device	Main specifications
Keithley 2182A Nanovoltmeter	Voltage range: 10 mV...100 V Resolution (10 mV range): 1 nV with internal R > 10 G $\Omega$ Resolution (100 V range): 10 $\mu$ V with internal R > 10 M $\Omega$
Keithley 6221 DC/AC current source	Output: 0.1 pA...100 mA Typical noise: 200 pA peak-peak/40 pA rms (2 $\mu$ A range) Voltage compliance: 0.1 V...100 V Programmable to generate arbitrary waveform currents, shortest unit: 1 ms In combination with 2182A Nanovoltmeter: can perform delta mode and pulse delta mode
Keithley 2401 source meter	Voltage source output: max. $\pm$ 20 V (min. 5 $\mu$ V steps) Voltage meas. resolution: 1 $\mu$ V (200 mV range) Current source output: max. $\pm$ 1 A (min. 50 pA steps) Current meas. resolution: 10 pA (1 $\mu$ A range) Programmable to generate standard and custom sweeps
Keithley 3730 multimeter	Voltage range: 100 mV...300 V Current range: 10 $\mu$ A...3 A
Switch module with 3730 matrix card	96 two-pole crosspoints with relays Switching time: 4 ms
Kepeco Power Supply BOP 100-10 MG	DC range: 100 V, 10 A Programming resolution: voltage: 14 bits/0.03 %; current: 14 bits/0.1 % Readback resolution: voltage: 16 bits/0.05 %; current: 16 bits / 0.1 %
Water cooled electromagnet	Maximum field at 50 mm distance of pole shoes: 0.12 T Maximum field at minimal separation of pole shoes (15 mm): 0.3 T

Table A.1: Selected specifications of DC equipment of setup.



Name of device	Main specifications
Picosecond pulse generator PSPL 10060A	Rise time: 55 ps Fall time: 115 ps Maximum amplitude: 10 V Range of duration: 100 ps...10 ns (in 2.5 ps steps) Repetition period: 10 $\mu$ s...1 s
Tektronics Oscilloscope DPO72004B	Rise time: 18 ps Number of digitized bits: 8 Sensitivity range: 10 mV/div to 1 V/div in 1-2-5 sequence Maximum bandwidth: 20 GHz Noise in 10 mV range: 0.87 mV (at 20 GHz); 0.49 mV (at 10 GHz) Real time sample rate: 50 GS/s Time base range: 10 ps/div...1000 s/div
Agilent Spectrum analyser MXA N9020A	Frequency range: 20 Hz...26.5 GHz Internal preamplifier: +20 dB gain between 100 kHz to 26.5 GHz; noise figure (at 5 GHz): 9 dB Resolution bandwidth: 1 Hz...8 MHz Range: 707 pV...7.07 V Average noise level (at 5 GHz): -153 dBm (preamp off); -166 dBm (preamp on)
Picosecond Power Splitter 5336	Bandwidth: DC to 20 GHz Delay: 180 ps Insertion loss, AC: 6.0 dB $\pm$ 0.5 dB Input impedance: 50 $\Omega$ $\pm$ 0.3 $\Omega$ max.
Mini-Circuits Bias-Tee ZX85-12G+	Frequency range: 0.2...12 GHz DC resistance from DC to RF+DC port: 1.8 $\Omega$ Insertion loss: 0.6 dB Max. DC voltage and current: 25 V; 400 mA
True Blue high frequency cables	Max. operating frequency: 26.5 GHz Attenuation (at 5 GHz): 0.59 dB/m Propagation delay: 4.56 ns/m

Table A.2: Selected specifications of the high frequency equipment of the setup.



# List of Figures

---

2.1	Schematic of the spin-dependent density of states in a ferromagnet. . . .	7
2.2	Phenomenological picture for the two-current model of the CPP GMR effect. . . . .	8
2.3	Density of states depending on the energy for the Jullière model of the TMR effect. . . . .	9
2.4	Tunneling density of states at normal incidence to the interface ( $\vec{k}_{\parallel} = 0$ ) for Fe(100)/MgO/Fe(100), taken from [24]. . . . .	12
2.5	Physical picture of spin-transfer torque in a ferromagnet/spacer/ferromagnet structure. . . . .	14
2.6	Schematic of the torques in the LLGS equation. . . . .	19
2.7	Schematic of the MRAM cell design for field-switched and STT-MRAM.	22
2.8	Switching current $I_c$ depending on the pulse width, taken from [38]. . .	24
2.9	Resistance versus voltage loop for a perpendicular MTJ, taken from [39].	25
2.10	Simulated phase diagram by Berkov et al. [61] for a metallic spin-valve at 0 K in the macrospin approximation. . . . .	31
2.11	Experimental phase diagram measured at room temperature by Kiselev et al. [28]. . . . .	32
2.12	Switching phase diagrams of asymmetric MgO-based MTJs at room temperature and 4.2 K, taken from [10]. . . . .	33
2.13	Phase diagrams of a metallic nanopillar with perpendicular magnetisation, taken from [62]. . . . .	34
2.14	Example of an R-V curve of an MTJ exhibiting back-hopping. . . . .	41
3.1	Historical evolution of the MTJ stack. . . . .	44
3.2	TEM image of an electron beam-grown 2.5 nm thick MgO barrier, taken from [82]. . . . .	46
3.3	Overview over equipment used for the three different types of measurements presented in this work. . . . .	48
3.4	Experimental magnetotransport setup. . . . .	48
3.5	Contacting of IBM-sample with 150 $\mu\text{m}$ GSG HF tip and sample electrode dimensions. . . . .	50

3.6	Pictures of the IBM samples. . . . .	50
3.7	Typical minor magnetoresistance loop of sample 3 taken at a constant current of 10 $\mu$ A. . . . .	53
3.8	Current-induced switching with a DC current and different applied magnetic fields in the easy axis direction for sample 1. . . . .	54
3.9	Schematic of the experimental setup for the phase diagram measurement in reflection mode. . . . .	56
3.10	Schematic of measurement sequence for obtaining the phase diagram. . . . .	57
3.11	Full reflection of pulse as detected by the oscilloscope at a pulse amplitude of 1.8 V. . . . .	58
3.12	Reflected signals from sample 3 in on-pulse measurement. . . . .	61
3.13	Schematic of the experimental setup for the thermally excited ferromagnetic resonance (TE-FMR). . . . .	62
4.1	Schematic of the MTJ and field definitions for the general case of an MTJ with two orthogonal anisotropy components. . . . .	67
4.2	Analytical phase diagram for the general case of an MTJ with two orthogonal anisotropy components. . . . .	71
4.3	Numerically simulated phase diagram for the general case. . . . .	72
4.4	Analytically calculated switching phase diagram for fully perpendicular MTJ. . . . .	75
4.5	Numerically simulated phase diagram for fully perpendicular MTJ. . . . .	75
4.6	Analytical phase diagram for an in-plane magnetic tunnel junction. . . . .	77
4.7	Numerically simulated phase diagram for an in-plane MTJ. . . . .	78
4.8	Numerically simulated phase diagram for an in-plane MTJ without perpendicular STT. . . . .	79
4.9	Schematic of one possible origin for the back-hopping phenomenon in in-plane magnetised MTJs. . . . .	80
4.10	DC phase diagram for sample 5. . . . .	82
4.11	Experimental pulsed phase diagrams of sample 2 in off-pulse measurement with different pulse lengths. . . . .	84
4.12	Schematic of the artefact in the off-pulse measurements for in-plane magnetised samples. . . . .	85
4.13	Experimental pulsed phase diagrams of sample 3 in off-pulse measurement (1 ns pulse length). . . . .	87
4.14	Determination of $a'_{\perp}$ from the off-pulse phase diagram. . . . .	88
4.15	Examples for the automated analysis of the on-pulse measurement of sample 3. . . . .	90
4.16	On-pulse phase diagram for sample 3 starting from P saturation. . . . .	91
4.17	On-pulse phase diagram for sample 3 starting from AP saturation. . . . .	92

4.18	DC Magnetoresistance loops of sample 6 taken at (a) room temperature at constant current (1 $\mu$ A) and (b) 4.2 K at different constant voltages. . . . .	94
4.19	Low temperature (4.2 K) DC phase diagram of sample 6. . . . .	95
4.20	Resistance versus magnetic field (R-H) and resistance versus current (R-I) loops for sample 4 (for TE-FMR). . . . .	96
4.21	Example of smoothing and fitting the data in the TE-FMR measurement for sample 4. . . . .	97
4.22	Overview over TE-FMR spectra for sample 4 for large field ranges and different applied currents and determination of $M_s$ . . . . .	98
4.23	Smoothed spectra for sample 4 from the TE-FMR for AP and P state. . . . .	101
4.24	Analysis of peak frequency vs. applied bias voltage for sample 4 in the TE-FMR. . . . .	103
4.25	Analysis of peak linewidth vs. applied bias voltage for sample 4 in the TE-FMR: determination of the in-plane STT from the linewidth at different bias voltages. . . . .	105
5.1	Analytical phase diagram with values determined from TE-FMR. . . . .	111
A.1	Wiring of equipment in experimental setup. . . . .	114
A.2	Wiring of nanovoltmeter, current source and switch in the experimental setup. . . . .	116
A.3	Wiring of the D-sub connectors to the matrix card in the switch in the experimental setup. . . . .	117



# List of Tables

---

2.1	Overview of literature values for the in-plane STT in different units. . .	39
2.2	Overview of literature values for the perpendicular STT. . . . .	40
3.1	Stack composition of IBM-MTJ. . . . .	46
3.2	Properties of samples used in this thesis. . . . .	47
3.3	Selected specifications of DC equipment of setup relevant for the measurements in this work. . . . .	51
3.4	Selected specifications of the high frequency equipment of the setup. . .	52
3.5	Comparison of maximum theoretical and actual signal height (in V) for some selected voltage pulse amplitudes for the P and AP configuration in the on-pulse phase diagram measurement. . . . .	59
4.1	Perpendicular STT values determined from the voltage bias-dependent TE-FMR peak frequencies. . . . .	103
4.2	In-plane STT values determined from the bias voltage dependent TE-FMR linewidths. . . . .	104
A.1	Selected specifications of DC equipment of setup. . . . .	118
A.2	Selected specifications of the high frequency equipment of the setup. . .	119





# Bibliography

---

- [1] J. C. Slonczewski, "Current-driven excitation of magnetic multilayers," *Journal of Magnetism and Magnetic Materials*, vol. 159, p. L1, June 1996.
- [2] L. Berger, "Emission of spin waves by a magnetic multilayer traversed by a current," *Physical Review B*, vol. 54, p. 9353, Oct. 1996.
- [3] *Everspin introduces the 64Mb DDR3 ST-MRAM*, <http://www.everspin.com>, November 2012.
- [4] J. C. Sankey, Y.-T. Cui, J. Z. Sun, J. C. Slonczewski, R. A. Buhrman, and D. C. Ralph, "Measurement of the spin-transfer-torque vector in magnetic tunnel junctions," *Nature Physics*, vol. 4, p. 67, Jan. 2008.
- [5] H. Kubota, A. Fukushima, K. Yakushiji, T. Nagahama, S. Yuasa, K. Ando, H. Maehara, Y. Nagamine, K. Tsunekawa, D. D. Djayaprawira, N. Watanabe, and Y. Suzuki, "Quantitative measurement of voltage dependence of spin-transfer torque in MgO-based magnetic tunnel junctions," *Nature Physics*, vol. 4, p. 37, Jan. 2008.
- [6] J. Xiao, G. E. W. Bauer, and A. Brataas, "Spin-transfer torque in magnetic tunnel junctions: Scattering theory," *Physical Review B*, vol. 77, p. 224419, June 2008.
- [7] J. C. Slonczewski and J. Z. Sun, "Theory of voltage-driven current and torque in magnetic tunnel junctions," *Journal of Magnetism and Magnetic Materials*, vol. 310, p. 169, Mar. 2007.
- [8] J. Z. Sun, M. C. Gaidis, G. Hu, E. J. O'Sullivan, S. L. Brown, J. J. Nowak, P. L. Trouilloud, and D. C. Worledge, "High-bias backhopping in nanosecond time-domain spin-torque switches of MgO-based magnetic tunnel junctions," *Journal of Applied Physics*, vol. 105, p. 07D109, Apr. 2009.
- [9] T. Min, J. Z. Sun, R. Beach, D. Tang, and P. Wang, "Back-hopping after spin torque transfer induced magnetization switching in magnetic tunneling junction cells," *Journal of Applied Physics*, vol. 105, p. 07D126, Apr. 2009.

- [10] S.-C. Oh, S.-Y. Park, A. Manchon, M. Chshiev, J.-H. Han, H.-W. Lee, J.-E. Lee, K.-T. Nam, Y. Jo, Y.-C. Kong, B. Dieny, and K.-J. Lee, "Bias-voltage dependence of perpendicular spin-transfer torque in asymmetric MgO-based magnetic tunnel junctions," *Nature Physics*, vol. 5, p. 898, Dec. 2009.
- [11] S.-Y. Park, J.-H. Han, S.-C. Oh, J.-E. Lee, K.-T. Nam, H.-W. Lee, Y. Jo, and K.-J. Lee, "Switching phase diagrams of current-induced magnetization switching in asymmetric MgO-based magnetic tunnel junctions," *Journal of Physics D: Applied Physics*, vol. 44, no. 6, p. 064008, 2011.
- [12] C. M. Schneider, D. R. Bürgler, S. Blügel, R. Waser, and M. Morgenstern, *40th IFF Springschool 2009. Spintronics - From GMR to Quantum Information*. Forschungszentrum Jülich GmbH, 2009.
- [13] P. M. Levy and S. Zhang, "Our current understanding of giant magnetoresistance in transition-metal multilayers," *Journal of Magnetism and Magnetic Materials*, vol. 151, p. 315, Dec. 1995.
- [14] N. F. Mott, "The resistance and thermoelectric properties of the transition metals," *Proceedings of the Royal Society of London. Series A, Mathematical and Physical Sciences*, vol. 156, p. 368, Aug. 1936.
- [15] P. R. Gross, *Lecture Notes on "Spintronics"*. Technische Universität München, 2005.
- [16] M. Julliere, "Tunneling between ferromagnetic films," *Physics Letters A*, vol. 54A, p. 225, Sept. 1975.
- [17] T. Yaoi, S. Ishio, and T. Miyazaki, "Dependence of magnetoresistance on temperature and applied voltage in a 82Ni-Fe/Al-Al<sub>2</sub>O<sub>3</sub>/Co tunneling junction," *Journal of Magnetism and Magnetic Materials*, vol. 126, p. 430, Sept. 1993.
- [18] J. S. Moodera, L. R. Kinder, T. M. Wong, and R. Meservey, "Large magnetoresistance at room temperature in ferromagnetic thin film tunnel junctions," *Physical Review Letters*, vol. 74, p. 3273, Apr. 1995.
- [19] S. Yuasa, T. Nagahama, A. Fukushima, Y. Suzuki, and K. Ando, "Giant room-temperature magnetoresistance in single-crystal Fe/MgO/Fe magnetic tunnel junctions," *Nature Materials*, vol. 3, p. 868, Dec. 2004.
- [20] S. S. P. Parkin, C. Kaiser, A. Panchula, P. M. Rice, B. Hughes, M. Samant, and S.-H. Yang, "Giant tunnelling magnetoresistance at room temperature with MgO (100) tunnel barriers," *Nature Materials*, vol. 3, p. 862, Dec. 2004.

- [21] S. Ikeda, J. Hayakawa, Y. Ashizawa, Y. M. Lee, K. Miura, H. Hasegawa, M. Tsunoda, F. Matsukura, and H. Ohno, "Tunnel magnetoresistance of 604 % at 300 K by suppression of Ta diffusion in CoFeB/MgO/CoFeB pseudo-spin-valves annealed at high temperature," *Applied Physics Letters*, vol. 93, p. 082508, Aug. 2008.
- [22] W. H. Butler, X.-G. Zhang, T. C. Schulthess, and J. M. MacLaren, "Spin-dependent tunneling conductance of Fe/MgO/Fe sandwiches," *Physical Review B*, vol. 63, p. 054416, Jan. 2001.
- [23] J. Mathon and A. Umerski, "Theory of tunneling magnetoresistance of an epitaxial Fe/MgO/Fe(001) junction," *Physical Review B*, vol. 63, p. 220403, May 2001.
- [24] X.-G. Zhang and W. H. Butler, "Band structure, evanescent states, and transport in spin tunnel junctions," *Journal of Physics: Condensed Matter*, vol. 15, no. 41, p. R1603, 2003.
- [25] D. C. Ralph and M. D. Stiles, "Spin transfer torques," *Journal of Magnetism and Magnetic Materials*, vol. 320, p. 1190, Apr. 2008.
- [26] E. B. Myers, D. C. Ralph, J. A. Katine, R. N. Louie, and R. A. Buhrman, "Current-induced switching of domains in magnetic multilayer devices," *Science*, vol. 285, p. 867, Aug. 1999.
- [27] J. A. Katine, F. J. Albert, R. A. Buhrman, E. B. Myers, and D. C. Ralph, "Current-driven magnetization reversal and spin-wave excitations in Co/Cu/Co pillars," *Physical Review Letters*, vol. 84, p. 3149, Apr. 2000.
- [28] S. I. Kiselev, J. C. Sankey, I. N. Krivorotov, N. C. Emley, R. J. Schoelkopf, R. A. Buhrman, and D. C. Ralph, "Microwave oscillations of a nanomagnet driven by a spin-polarized current," *Nature*, vol. 425, p. 380, Sept. 2003.
- [29] M. D. Stiles and A. Zangwill, "Anatomy of spin-transfer torque," *Physical Review B*, vol. 66, p. 014407, June 2002.
- [30] J. C. Slonczewski, "Currents and torques in metallic magnetic multilayers," *Journal of Magnetism and Magnetic Materials*, vol. 247, p. 324, June 2002.
- [31] K. Xia, P. J. Kelly, G. E. W. Bauer, A. Brataas, and I. Turek, "Spin torques in ferromagnetic/normal-metal structures," *Physical Review B*, vol. 65, p. 220401, May 2002.
- [32] I. Theodonis, N. Kioussis, A. Kalitsov, M. Chshiev, and W. H. Butler, "Anomalous bias dependence of spin torque in magnetic tunnel junctions," *Physical Review Letters*, vol. 97, p. 237205, Dec. 2006.

- [33] T. Gilbert, "A phenomenological theory of damping in ferromagnetic materials," *IEEE Transactions on Magnetics*, vol. 40, p. 3443, Nov. 2004.
- [34] C. Chappert, A. Fert, and F. N. Van Dau, "The emergence of spin electronics in data storage," *Nature Materials*, vol. 6, p. 813, Nov. 2007.
- [35] S. Mao, Y. Chen, F. Liu, X. Chen, B. Xu, P. Lu, M. Patwari, H. Xi, C. Chang, B. Miller, D. Menard, B. Pant, J. Loven, K. Duxstad, S. Li, Z. Zhang, A. Johnston, R. Lamberton, M. Gubbins, T. McLaughlin, J. Gadbois, J. Ding, B. Cross, S. Xue, and P. Ryan, "Commercial TMR heads for hard disk drives: characterization and extendibility at 300 Gbit/in<sup>2</sup>," *IEEE Transactions on Magnetics*, vol. 42, p. 97, Feb. 2006.
- [36] J. Slaughter, "Materials for magnetoresistive random access memory," *Annual Review of Materials Research*, vol. 39, p. 277, Aug. 2009.
- [37] S. Mangin, D. Ravelosona, J. A. Katine, M. J. Carey, B. D. Terris, and E. E. Fullerton, "Current-induced magnetization reversal in nanopillars with perpendicular anisotropy," *Nature Materials*, vol. 5, p. 210, Mar. 2006.
- [38] T. Aoki, Y. Ando, D. Watanabe, M. Oogane, and T. Miyazaki, "Spin transfer switching in the nanosecond regime for CoFeB/MgO/CoFeB ferromagnetic tunnel junctions," *Journal of Applied Physics*, vol. 103, p. 103911, May 2008.
- [39] J. C. Leutenantsmeyer, M. Walter, V. Zbarsky, M. Münzenberg, R. Gareev, K. Rott, A. Thomas, G. Reiss, P. Peretzki, H. Schuhmann, M. Seibt, M. Czerner, and C. Heiliger, "Parameter space for thermal spin-transfer torque," *Spin*, vol. 03, p. 1350002, Mar. 2013.
- [40] J. Sun and D. Ralph, "Magnetoresistance and spin-transfer torque in magnetic tunnel junctions," *Journal of Magnetism and Magnetic Materials*, vol. 320, p. 1227, Apr. 2008.
- [41] M. Sharma, S. X. Wang, and J. H. Nickel, "Inversion of spin polarization and tunneling magnetoresistance in spin-dependent tunneling junctions," *Physical Review Letters*, vol. 82, p. 616, Jan. 1999.
- [42] Y. Higo, K. Yamane, K. Ohba, H. Narisawa, K. Bessho, M. Hosomi, and H. Kano, "Thermal activation effect on spin transfer switching in magnetic tunnel junctions," *Applied Physics Letters*, vol. 87, p. 082502, Aug. 2005.
- [43] M. Yoshikawa, T. Ueda, H. Aikawa, N. Shimomura, E. Kitagawa, M. Nakayama, T. Kai, K. Nishiyama, T. Nagase, T. Kishi, S. Ikegawa, and H. Yoda, "Estimation of spin transfer torque effect and thermal activation effect on magnetization reversal in CoFeB/MgO/CoFeB magnetoresistive tunneling junctions," *Journal of Applied Physics*, vol. 101, p. 09A511, May 2007.

- [44] R. H. Koch, J. A. Katine, and J. Z. Sun, "Time-resolved reversal of spin-transfer switching in a nanomagnet," *Physical Review Letters*, vol. 92, p. 088302, Feb. 2004.
- [45] I. N. Krivorotov, N. C. Emley, A. G. F. Garcia, J. C. Sankey, S. I. Kiselev, D. C. Ralph, and R. A. Buhrman, "Temperature dependence of spin-transfer-induced switching of nanomagnets," *Physical Review Letters*, vol. 93, p. 166603, Oct. 2004.
- [46] M. P. Sharrock, "Time dependence of switching fields in magnetic recording media (invited)," *Journal of Applied Physics*, vol. 76, p. 6413, Nov. 1994.
- [47] R. Skomski, "Role of thermodynamic fluctuations in magnetic recording (invited)," *Journal of Applied Physics*, vol. 101, p. 09B104, May 2007.
- [48] Z. Li and S. Zhang, "Thermally assisted magnetization reversal in the presence of a spin-transfer torque," *Physical Review B*, vol. 69, p. 134416, Apr. 2004.
- [49] Z. Li, S. Zhang, Z. Diao, Y. Ding, X. Tang, D. M. Apalkov, Z. Yang, K. Kawabata, and Y. Huai, "Perpendicular spin torques in magnetic tunnel junctions," *Physical Review Letters*, vol. 100, p. 246602, June 2008.
- [50] J. Z. Sun, "Spin-current interaction with a monodomain magnetic body: A model study," *Physical Review B*, vol. 62, p. 570, July 2000.
- [51] T. Devolder, P. Crozat, J.-V. Kim, C. Chappert, K. Ito, J. A. Katine, and M. J. Carey, "Magnetization switching by spin torque using subnanosecond current pulses assisted by hard axis magnetic fields," *Applied Physics Letters*, vol. 88, p. 152502, Apr. 2006.
- [52] T. Aoki, Y. Ando, M. Oogane, and H. Naganuma, "Reproducible trajectory on subnanosecond spin-torque magnetization switching under a zero-bias field for MgO-based ferromagnetic tunnel junctions," *Applied Physics Letters*, vol. 96, p. 142502, Apr. 2010.
- [53] M. Morota, A. Fukushima, H. Kubota, K. Yakushiji, S. Yuasa, and K. Ando, "Dependence of switching current distribution on current pulse width of current-induced magnetization switching in MgO-based magnetic tunnel junction," *Journal of Applied Physics*, vol. 103, p. 07A707, Feb. 2008.
- [54] I. N. Krivorotov, N. C. Emley, J. C. Sankey, S. I. Kiselev, D. C. Ralph, and R. A. Buhrman, "Time-domain measurements of nanomagnet dynamics driven by spin-transfer torques," *Science*, vol. 307, p. 228, Jan. 2005.

- [55] H. Tomita, K. Konishi, T. Nozaki, H. Kubota, A. Fukushima, K. Yakushiji, S. Yuasa, Y. Nakatani, T. Shinjo, M. Shiraishi, and Y. Suzuki, "Single-shot measurements of spin-transfer switching in CoFeB/MgO/CoFeB magnetic tunnel junctions," *Applied Physics Express*, vol. 1, p. 061303, June 2008.
- [56] T. Devolder, J. Hayakawa, K. Ito, H. Takahashi, S. Ikeda, P. Crozat, N. Zerounian, J. V. Kim, C. Chappert, and H. Ohno, "Single-shot time-resolved measurements of nanosecond-scale spin-transfer induced switching: Stochastic versus deterministic aspects," *Physical Review Letters*, vol. 100, p. 057206, Feb. 2008.
- [57] T. Aoki, Y. Ando, M. Oogane, and H. Naganuma, "Dynamic magnetic intermediate state during nanosecond spin transfer switching for MgO-based magnetic tunnel junctions," *Applied Physics Express*, vol. 3, no. 5, p. 053002, 2010.
- [58] Y.-T. Cui, G. Finocchio, C. Wang, J. A. Katine, R. A. Buhrman, and D. C. Ralph, "Single-shot time-domain studies of spin-torque-driven switching in magnetic tunnel junctions," *Physical Review Letters*, vol. 104, p. 097201, Mar. 2010.
- [59] K.-J. Lee, A. Deac, O. Redon, J.-P. Nozieres, and B. Dieny, "Excitations of incoherent spin-waves due to spin-transfer torque," *Nature Materials*, vol. 3, p. 877, Dec. 2004.
- [60] S. Serrano-Guisan, K. Rott, G. Reiss, J. Langer, B. Ocker, and H. W. Schumacher, "Biased quasiballistic spin torque magnetization reversal," *Physical Review Letters*, vol. 101, p. 087201, Aug. 2008.
- [61] D. V. Berkov and J. Miltat, "Spin-torque driven magnetization dynamics: Micromagnetic modeling," *Journal of Magnetism and Magnetic Materials*, vol. 320, p. 1238, Dec. 2008.
- [62] S. Le Gall, J. Cucchiara, M. Gottwald, C. Berthelot, C.-H. Lambert, Y. Henry, D. Bedau, D. B. Gopman, H. Liu, A. D. Kent, J. Z. Sun, W. Lin, D. Ravelosona, J. A. Katine, E. E. Fullerton, and S. Mangin, "State diagram of nanopillar spin valves with perpendicular magnetic anisotropy," *Physical Review B*, vol. 86, p. 014419, July 2012.
- [63] S. Kaka, M. R. Pufall, W. H. Rippard, T. J. Silva, S. E. Russek, and J. A. Katine, "Mutual phase-locking of microwave spin torque nano-oscillators," *Nature*, vol. 437, p. 389, Sept. 2005.
- [64] A. M. Deac, A. Fukushima, H. Kubota, H. Maehara, Y. Suzuki, S. Yuasa, Y. Nagamine, K. Tsunekawa, D. D. Djayaprawira, and N. Watanabe, "Bias-driven high-power microwave emission from MgO-based tunnel magnetoresistance devices," *Nature Physics*, vol. 4, p. 803, Oct. 2008.

- [65] J. C. Sankey, P. M. Braganca, A. G. F. Garcia, I. N. Krivorotov, R. A. Buhrman, and D. C. Ralph, "Spin-transfer-driven ferromagnetic resonance of individual nanomagnets," *Physical Review Letters*, vol. 96, p. 227601, June 2006.
- [66] A. A. Tulapurkar, Y. Suzuki, A. Fukushima, H. Kubota, H. Maehara, K. Tsunekawa, D. D. Djayaprawira, N. Watanabe, and S. Yuasa, "Spin-torque diode effect in magnetic tunnel junctions," *Nature*, vol. 438, p. 339, Nov. 2005.
- [67] C. Wang, Y.-T. Cui, J. Z. Sun, J. A. Katine, R. A. Buhrman, and D. C. Ralph, "Bias and angular dependence of spin-transfer torque in magnetic tunnel junctions," *Physical Review B*, vol. 79, p. 224416, June 2009.
- [68] W. Skowronski, M. Czapkiewicz, M. Frankowski, J. Wrona, T. Stobiecki, G. Reiss, K. Chalapat, G. S. Paraoanu, and S. van Dijken, "Influence of MgO tunnel barrier thickness on spin-transfer ferromagnetic resonance and torque in magnetic tunnel junctions," *Physical Review B*, vol. 87, p. 094419, Mar. 2013.
- [69] S. Petit, C. Baraduc, C. Thirion, U. Ebels, Y. Liu, M. Li, P. Wang, and B. Dieny, "Spin-torque influence on the high-frequency magnetization fluctuations in magnetic tunnel junctions," *Physical Review Letters*, vol. 98, p. 077203, Feb. 2007.
- [70] S. Petit, N. de Mestier, C. Baraduc, C. Thirion, Y. Liu, M. Li, P. Wang, and B. Dieny, "Influence of spin-transfer torque on thermally activated ferromagnetic resonance excitations in magnetic tunnel junctions," *Physical Review B*, vol. 78, p. 184420, Nov. 2008.
- [71] M. H. Jung, S. Park, C.-Y. You, and S. Yuasa, "Bias dependences of in-plane and out-of-plane spin-transfer torques in symmetric MgO-based magnetic tunnel junctions," *Physical Review B*, vol. 81, p. 134419, Apr. 2010.
- [72] O. G. Heinonen, S. W. Stokes, and J. Y. Yi, "Perpendicular spin torque in magnetic tunnel junctions," *Physical Review Letters*, vol. 105, p. 066602, Aug. 2010.
- [73] C. Wang, Y.-T. Cui, J. A. Katine, R. A. Buhrman, and D. C. Ralph, "Time-resolved measurement of spin-transfer-driven ferromagnetic resonance and spin torque in magnetic tunnel junctions," *Nature Physics*, vol. 7, p. 496, June 2011.
- [74] L. Xue, C. Wang, Y. T. Cui, J. A. Katine, R. A. Buhrman, and D. C. Ralph, "Network analyzer measurements of spin transfer torques in magnetic tunnel junctions," *Applied Physics Letters*, vol. 101, p. 022417, July 2012.
- [75] C. Heiliger and M. D. Stiles, "Ab initio studies of the spin-transfer torque in magnetic tunnel junctions," *Physical Review Letters*, vol. 100, p. 186805, May 2008.

- [76] T. Min, Q. Chen, R. Beach, G. Jan, C. Horng, W. Kula, T. Torng, R. Tong, T. Zhong, D. Tang, P. Wang, M. Chen, J. Z. Sun, J. K. Debrosse, D. C. Worledge, T. M. Maffitt, and W. J. Gallagher, "A study of write margin of spin torque transfer magnetic random access memory technology," *IEEE Transactions on Magnetics*, vol. 46, p. 2322, June 2010.
- [77] S.-Y. Park, Y. Jo, and K.-J. Lee, "Measurement of perpendicular spin torque at high bias via the pulsed switching phase diagram," *Physical Review B*, vol. 84, p. 214417, Dec. 2011.
- [78] J. J. Nowak, R. P. Robertazzi, J. Z. Sun, G. Hu, D. W. Abraham, P. L. Trouiloud, S. Brown, M. C. Gaidis, E. J. O'Sullivan, W. J. Gallagher, and D. C. Worledge, "Demonstration of ultralow bit error rates for spin-torque magnetic random-access memory with perpendicular magnetic anisotropy," *IEEE Magnetics Letters*, vol. 2, p. 3000204, June 2011.
- [79] Z. Wang, Y. Zhou, J. Zhang, and Y. Huai, "Bit error rate investigation of spin-transfer-switched magnetic tunnel junctions," *Applied Physics Letters*, vol. 101, p. 142406, Oct. 2012.
- [80] G. H. Yu and X. Peng, "Inter-diffusion study in MgO tunneling magneto-resistive (TMR) system by XPS," *Applied Surface Science*, vol. 256, p. 6592, Sept. 2010.
- [81] S. Yuasa, Y. Suzuki, T. Katayama, and K. Ando, "Characterization of growth and crystallization processes in CoFeB/MgO/CoFeB magnetic tunnel junction structure by reflective high-energy electron diffraction," *Applied Physics Letters*, vol. 87, p. 242503, Dec. 2005.
- [82] H. Kurt, K. Oguz, T. Niizeki, and J. M. D. Coey, "Giant tunneling magnetoresistance with electron beam evaporated MgO barrier and CoFeB electrodes," *Journal of Applied Physics*, vol. 107, p. 083920, Apr. 2010.
- [83] H. Kurt, K. Rode, K. Oguz, M. Boese, C. C. Faulkner, and J. M. D. Coey, "Boron diffusion in magnetic tunnel junctions with MgO (001) barriers and CoFeB electrodes," *Applied Physics Letters*, vol. 96, p. 262501, June 2010.
- [84] J. J. Cha, J. C. Read, W. F. Egelhoff, P. Y. Huang, H. W. Tseng, Y. Li, R. A. Buhrman, and D. A. Muller, "Atomic-scale spectroscopic imaging of CoFeB/Mg-B-O/CoFeB magnetic tunnel junctions," *Applied Physics Letters*, vol. 95, p. 032506, July 2009.
- [85] J. R. Andrews, *Low-pass risetime filters for time domain applications*. Picosecond Application Note AN-7a, Picosecond Pulse Labs, Mar. 1999.



- [86] J. R. Andrews, *Time domain reflectometry (TDR) and time domain transmission (TDT) measurement fundamentals*. Picosecond Application Note AN-15, Picosecond Pulse Labs, Nov. 2004.
- [87] C. Kittel, *Einführung in die Festkörperphysik*. Oldenbourg Wissenschaftsverlag GmbH, 2006.
- [88] J. Grollier, V. Cros, H. Jaffres, A. Hamzic, J. M. George, G. Faini, J. Ben Youssef, H. Le Gall, and A. Fert, “Field dependence of magnetization reversal by spin transfer,” *Physical Review B*, vol. 67, p. 174402, May 2003.
- [89] M. A. Zimmler, B. Özyilmaz, W. Chen, A. D. Kent, J. Z. Sun, M. J. Rooks, and R. H. Koch, “Current-induced effective magnetic fields in Co/Cu/Co nanopillars,” *Physical Review B*, vol. 70, p. 184438, Nov. 2004.
- [90] J. Coey, *Magnetism and Magnetic Materials*. Cambridge University Press, 2010.
- [91] D. C. Worledge, G. Hu, D. W. Abraham, J. Z. Sun, P. L. Trouilloud, J. Nowak, S. Brown, M. C. Gaidis, E. J. O’Sullivan, and R. P. Robertazzi, “Spin torque switching of perpendicular Ta/CoFeB/MgO-based magnetic tunnel junctions,” *Applied Physics Letters*, vol. 98, p. 022501, Jan. 2011.
- [92] D. Gusakova, D. Houssameddine, U. Ebels, B. Dieny, L. Buda-Prejbeanu, M. C. Cyrille, and B. Delaët, “Spin-polarized current-induced excitations in a coupled magnetic layer system,” *Physical Review B*, vol. 79, p. 104406, Mar. 2009.
- [93] C. Bilzer, T. Devolder, J.-V. Kim, G. Counil, C. Chappert, S. Cardoso, and P. P. Freitas, “Study of the dynamic magnetic properties of soft CoFeB films,” *Journal of Applied Physics*, vol. 100, p. 053903, Sept. 2006.
- [94] H. X. Yang, M. Chshiev, B. Dieny, J. H. Lee, A. Manchon, and K. H. Shin, “First-principles investigation of the very large perpendicular magnetic anisotropy at Fe/MgO and Co/MgO interfaces,” *Physical Review B*, vol. 84, p. 054401, Aug. 2011.
- [95] S. Ikeda, K. Miura, H. Yamamoto, K. Mizunuma, H. D. Gan, M. Endo, S. Kanai, J. Hayakawa, F. Matsukura, and H. Ohno, “A perpendicular-anisotropy CoFeB-MgO magnetic tunnel junction,” *Nature Materials*, vol. 9, p. 721, July 2010.
- [96] N. Stutzke, S. L. Burkett, and S. E. Russek, “Temperature and field dependence of high-frequency magnetic noise in spin valve devices,” *Applied Physics Letters*, vol. 82, p. 91, Jan. 2003.
- [97] G. D. Fuchs, J. C. Sankey, V. S. Pribiag, L. Qian, P. M. Braganca, A. G. F. Garcia, E. M. Ryan, Z.-P. Li, O. Ozatay, D. C. Ralph, and R. A. Buhrman, “Spin-torque

- ferromagnetic resonance measurements of damping in nanomagnets,” *Applied Physics Letters*, vol. 91, p. 062507, Aug. 2007.
- [98] J. Hayakawa, S. Ikeda, K. Miura, M. Yamanouchi, Y. M. Lee, R. Sasaki, M. Ichimura, K. Ito, T. Kawahara, R. Takemura, T. Meguro, F. Matsukura, H. Takahashi, H. Matsuoka, and H. Ohno, “Current-induced magnetization switching in MgO barrier magnetic tunnel junctions with CoFeB-based synthetic ferrimagnetic free layers,” *IEEE Transactions on Magnetics*, vol. 44, p. 1962, July 2008.
- [99] A. Natarajarathinam, Z. Tadisina, T. Mewes, S. Watts, E. Chen, and S. Gupta, “Influence of capping layers on CoFeB anisotropy and damping,” *Journal of Applied Physics*, vol. 112, p. 053909, Sept. 2012.
- [100] Y. Guan, J. Z. Sun, X. Jiang, R. Moriya, L. Gao, and S. S. P. Parkin, “Thermal-magnetic noise measurement of spin-torque effects on ferromagnetic resonance in MgO-based magnetic tunnel junctions,” *Applied Physics Letters*, vol. 95, p. 082506, Aug. 2009.